Department of Chemistry, University of Jyväskylä

THEORETICAL STUDIES ON SPECTROSCOPY AND ATOMIC DYNAMICS IN RARE GAS SOLIDS

TONI KILJUNEN

Academic Dissertation
for the Degree of
Doctor of Philosophy

Jyväskylä, Finland 2001

Research Report No. 84

OPPONENT

Academy Prof. Risto M. Nieminen
Laboratory of Physics, Helsinki University of Technology

SUPERVISOR

Prof. Henrik Kunttu
Department of Chemistry, University of Jyväskylä

REVIEWERS

Prof. Alexander V. Nemukhin
Laboratory of Chemical Cybernetics, Department of Chemistry,
Moscow State University

Dr. Dage Sundholm
Laboratory for Instruction in Swedish, Department of Chemistry,
University of Helsinki

DEPARTMENT OF CHEMISTRY, UNIVERSITY OF JYVÄSKYLÄ
RESEARCH REPORT No. 84

THEORETICAL STUDIES ON SPECTROSCOPY AND ATOMIC DYNAMICS IN RARE GAS SOLIDS

BY

TONI KILJUNEN

Academic Dissertation
for the degree of
Doctor of Philosophy

To be presented, by permission of the Faculty of Mathematics and Science
of the University of Jyväskylä, for public examination
in Auditorium KEM 4, on June 15th, 2001, at 12 noon

University of Jyväskylä
Jyväskylä, Finland
ISBN 951-39-0963-8
ISSN 0357-346X

URN:ISBN:978-951-39-9871-4
ISBN 978-951-39-9871-4 (PDF)
ISSN 0357-346X

Jyväskylän yliopisto, 2023

Preface

The study reviewed in this thesis has been carried out between the autumn 1998 and the winter 2001 at the Chemistry Department of the University of Jyväskylä.

I wish to express my warmest appreciation for the inspiring spirit I have experienced during the years in the research group. Without the excellent leadership of my supervisor Prof. Henrik Kunttu, the constant multitasking and guidance of the primus motor Dr. Jussi Eloranta, and the active bustle of the foremost collaborators Mr. Jussi "the oracle" Ahokas and Mr. Kari Vaskonen in the laboratory, the work could not have been accomplished. Owing to these great individuals, the time spent working in the Kunttu Group has felt like a leisure.

Thanks are also due to the fellow physico-chemists and personnel at the Department, much for the same reasons, for creating the pleasant atmosphere and especially for the refreshing moments at the coffeeroom. My gratitude is substantial to my roommates at work: Jani and Viivi for putting up with me, and particularly Pekka for taking the mantle of Unix Wizard on his shoulders.

I am grateful to the colleagues at the Helsinki matrix group, Prof. Markku Räsänen, Dr. Mika Pettersson and Dr. Leonid Khriachtchev, for their interest and participation in my work.

Professor Emeritus Matti Nurmia is thanked for revising the language of this thesis.

The financial support from the Ministry of Education and the Graduate School of Computational Chemistry and Molecular Spectroscopy (LASKEMO), as well as the computing resources of the Center for Scientific Computing, are gratefully acknowledged.

Finally, I want to thank my family and friends for making the time during the course of this work a constant bliss.

Jyväskylä, April 2001
Toni Kiljunen

Abstract

Challenges of chemical dynamics have been encountered in the present study consisting of five publications, where a theoretical approach has been chosen to clarify the observations gathered by magnetic and optical spectroscopies in solid rare gases. Detailed understanding of the events at a microscopic level is necessitated for control over the basic processes occurring in the solids. The knowledge of atom trapping sites and dynamics gained here is of both practical and academic importance in this research field of chemical physics.

In this thesis a combined quantum chemical - classical mechanics approach is adopted. First, accurate *ab initio* electronic structure methods are used for the atom pairs present in the system in order to parametrize the interaction energies and spectroscopic quantities. Second, the pairwise information is used in molecular dynamics simulations, which yields the time-averaged effects of the surrounding medium on the dopant atom.

The electron paramagnetic resonance spectra of H, Li, Na, and B atoms in rare gas solids are simulated by a novel combination of computational tools, and the results agree well with the experiments. Definite assignments for trapping in various lattice geometries with distinct symmetries and volumes have been achieved, and the developed methodology seems promising for future use in studies of more complex cases. Atomic dynamics plays a crucial role in the optical studies, and the present simulations have been successful in associating the experimental observations and the temperature dependent atomic motion to specific trapping configurations of matrix isolated B and S atoms. In particular, both thermal and photoinduced recombinant emissions of S_2 have been interpreted with the aid of simulations, and the B atom optical transitions perturbed in the solids have been assigned on the basis of the knowledge of computed potential energy curves, simulated energetics, and combinatory magnetic effects.

Original publications

This thesis is a review based on the following original research papers.

I **_Ab initio_ and molecular-dynamics studies on rare gas hydrides: Potential-energy curves, isotropic hyperfine properties, and matrix cage trapping of atomic hydrogen**
Toni Kiljunen, Jussi Eloranta, and Henrik Kunttu,
J. Chem. Phys. **110**, 11814–11822 (1999).
https://doi.org/10.1063/1.479173

II **Theoretical analysis of alkali metal trapping sites in rare gas matrices**
Jussi Ahokas, Toni Kiljunen, Jussi Eloranta, and Henrik Kunttu,
J. Chem. Phys. **112**, 2420–2426 (2000).
https://doi.org/10.1063/1.480825

III **Electronic structure and short-range recombination dynamics of S_2 in solid argon**
Toni Kiljunen, Jussi Eloranta, Henrik Kunttu, Leonid Khriachtchev, Mika Pettersson, and Markku Räsänen,
J. Chem. Phys. **112**, 7475–7483 (2000).
https://doi.org/10.1063/1.481345

IV **Magnetic properties of atomic boron in rare gas matrices: An electron paramagnetic resonance study with _ab initio_ and diatomics-in-molecules molecular dynamics analysis**
Toni Kiljunen, Jussi Ahokas, Jussi Eloranta, and Henrik Kunttu,
J. Chem. Phys. **114**, 7144–7156 (2001).
https://doi.org/10.1063/1.1360796

V **Optical properties of atomic boron in rare gas matrices: An ultraviolet absorption/laser induced fluorescence study with _ab initio_ and diatomics-in-molecules molecular dynamics analysis**
Toni Kiljunen, Jussi Ahokas, Jussi Eloranta, and Henrik Kunttu,
J. Chem. Phys. **114**, 7157–7165 (2001).
https://doi.org/10.1063/1.1360797

The author of the present thesis has performed all the *ab initio* work in paper I and written the paper. The author has conducted and guided the computational work in II and written the paper. The author was the main writer of paper III, where he has calculated the quantum chemical part, participated in writing the necessary computer codes and run all the final simulations. The author has done the computational work in papers IV and V, coded a portion of the simulation programs, and written the papers. The experimental results presented in papers IV and V were provided by Mr. Jussi Ahokas and Dr. Jussi Eloranta.

Abbreviations

HF-SCF	Hartree-Fock self-consistent field, molecular orbital method.
MCSCF	Multiconfiguration SCF, generalization.
CASSCF	Complete active space SCF, special MCSCF case.
CISD	Single and double excited configuration interaction.
MRCI+Q	Multireference configuration interaction + Davidson correction for quadruple excitations.
CCSD(T)	Single and double excitation Coupled Cluster extended with perturbative estimation of connected triple excitations.
QCISD	Quadratic CISD, size-extensive amendment of the CI model.
MBPT	Many-body perturbation theory.
MP	Møller-Plesset PT.
RS	Rayleigh-Schrödinger PT.
FC	Fermi contact, isotropic hyperfine interaction.
SD	Spin dipolar, anisotropic hyperfine interaction.
MD	Molecular Dynamics, deterministic simulation method.
PES	Potential energy surface(s).
DIM	Diatomics-in-Molecules, method for PES construction.

Contents

Chapter 1

Introduction

Chemical dynamics in condensed matter forms a branch of chemistry and physics that deals with a wide range of processes from simple atomic diffusion to the broad field of chemical reaction dynamics. Because of the many-body nature of these interactions an understanding of the events at a molecular level is the challenge in this frontier of science. A convergence of quantitative modelling and interpretation of various processes is attained by a synergy of experimental and theoretical tools. A prediction of accelerated progress [1] for the field in the future is supported by the two most incisive methods: ultrafast laser spectroscopy and large-scale simulations with computers. The wealth of photophysics and spectroscopy has been exploited as basic research, carried out for the pursued definite characterization of the chemical dynamics, to reveal the details hidden in the electronic structure of a particular system under study. Experimental methods at one's disposal range from optical absorption or emission based techniques to more seldom used electron paramagnetic resonance (EPR) spectroscopy. Moreover, and most important in the view of the present study, microscopic description of the observed spectroscopy and dynamics can be pursued at first-principles level by advanced theoretical methods nowadays feasible due to the increased computer power and the development of new efficient algorithms.

Rare gases (Rg) condensate in cryogenic conditions and form more or less ordered structures, namely, glassy crystalline or light scattering powderous solids that are generally termed as matrices. The inertness of the matrix atoms to chemical reactivity is reflected in their other common name, the noble gases.

As such, they provide a versatile medium for the study of fundamentals in elementary physico-chemical processes. In particular, doping these matrices with atomic or small molecular impurities constitutes an experimental technique called matrix isolation [2], which allows a detailed exploration of a variety of issues of key importance for our understanding of the microscopic behaviour of the chemical events of interest. For example, recombination of chemical intermediates, energy transfer and charge transfer reactions, atom transfer and tunnelling are prototypical processes amenable to such scrutiny.

The control over many-body events in chemical dynamics, such as reactions and diffusion, is more easily attained in these structurally well-defined atomic cryocrystal hosts than for example in liquids. As a practical example, the possibility of chemical energy storage in cryogenic solids by trapping reactive atoms, radicals or chemical intermediates, and controlling their subsequent recombination by thermal annealing, is opened by the increased knowledge of the mentioned properties. The advanced propellant systems named "high energy density materials" serve as a representable example of applications long carried out in the field of matrix isolation [2] which still are under active debate and development [3–5]. The work in this area is aimed at increased propellant densities and specific impulses of astronautical fuels such as impurity doped solid H_2.

The information gathered from experiments in solids is subject to perpetual averaging processes of dynamic and sructural origin. Therefore, as the spectroscopic methods become blunted in this respect, the need for theoretical aid in interpretation becomes evident. On the other hand, cryocrystals provide an ideal testing ground for the accuracy of theoretical treatments. The fundamental problems in condensed matter physics, such as lattice dynamics, isotropic and anisotropic interactions, impurity effects, phase transitions, etc., are all issues related to cryocrystals themselves [6,7], whereas matrix isolation science is more directed at molecular phenomena and solvent effects in these solids [1]. Either way around, the theoretical approaches encounter challenging obstacles due to the immense number of interacting species and degrees of freedom that need to be considered. This is the reason why purely quantum mechanical approaches, that is, solving the time-dependent Schrödinger equation by some affordable way, are rarely used in large-scale simulations and, instead, various approximations of semi-classical nature are usually employed. A thorough discussion of the experimental and theoretical aspects of the chemical physics in rare gas solids has been presented in a recent review article [1].

Finally, it should be mentioned that the role of rare gases as inert solvents has recently been changed by the fact that these stable atoms also form compounds and show enhanced reactivity [8–10]. This interesting novel chemistry is not limited to low temperature matrices alone. The first gas phase observation of the molecule HXeI belonging to the set of molecules synthetized by the Helsinki matrix group was reported recently [11]. The progress in this direction opens a new avenue in matrix isolation: studying rare gas containing molecules, in addition to the old function of matrices as merely passive stabilizing media.

The aim and the motivation of the present study as a whole has been twofold. First, to provide a theoretical interpretation of the measured atomic and molecular data gathered by optical and magnetic spectroscopy. Second, and more general, to test the applicability of certain methodological approximations in theoretical work, in terms of both efficiency and reliability, considering interactions and observables in large periodic systems in the condensed phase.

The main emphasis in this work is on the magnetic interactions since EPR seems conceptually ideally suited for exploring the nature of trapping of matrix isolated atoms. The power of the EPR technique is in elucidating details of the electronic structure of the open shell species in question. This originates from the fact that EPR transitions depend on the electronic ground state only and are very sensitive to small changes in the environment of the paramagnetic impurity.

Initially, the need for theoretical investigation arose from the EPR measurements in Rg matrices (Ne, Ar, Kr, Xe) that were recently carried out in our laboratory [12–14], and by several authors [15–18] before us. The effect of the lattice geometry on the spin density and, therefore, on the magnetic properties of an impurity atom trapped in sites of various character, was the problem to be solved, or at least, qualitatively explained. The study expanded from the isotropic case, both in electrostatic and magnetic hyperfine interactions, to cover also anisotropicity characteristics of ^2P atoms in terms of potential energy matrices and tensoral magnetic properties. A step beside the main line of this study was taken to a molecular case where recombination of photolytically produced separated S atoms was studied. This investigation was connected to the experimental observations by the Helsinki matrix group [19] and pertained to the results of short-range separation of the fragments of photolyzed NO obtained in our laboratory [20].

The five articles which form the body of this thesis may be partitioned into isotropic, in-between, and anisotropic cases, where the first group is made up of papers I and II that consider the dynamics of the isotropic ^2S state atoms H, Li, and Na using a scalar interaction method. The in-between case is the study of S+S recombination dynamics, in paper III, that is anisotropic in nature but was handled isotropically with a single potential energy surface (PES). Finally, the last group consists of papers IV and V where the dynamics and properties of ^2P state B atom in a lattice environment were rigorously described.

The most distinct separation in treatment, common to all the above mentioned three cases, is obviously the division of the system into quantum mechanical and classical portions. That is, all the as-accurate-as-possible quantum chemical parameters were calculated for atom pairs, and then used as inputs in subsequent classical dynamics part, which extends the treatment to the full scale of the lattice.

During the present series of studies more insight into atomic trapping and diffusion has been gained by theoretical investigation. The adopted methodology has helped to finally interpret experimental spectra, both magnetic and optical, with significant certainty. A profound understanding of the matrix effects on spectral observables and the way they are reflected in the perturbed spin densities and electronic states has been achieved. The developed procedure for including the hyperfine properties in a simulation and accounting for the motional averaging in the solid host lattice is applied probably for the first time here. The results are promising, and the methodology seems applicable for future use in extended and more complex studies.

The outline of the thesis is the following: The theoretical background is established in Chapter 2 by first discussing briefly the concepts of the applied quantum chemical methods for computing the potential energy curves. Then, the origin of the magnetic parameters and their connection to spin Hamiltonian formalism and experiment is presented. The classical molecular dynamics (MD) simulations that utilize the *ab initio* data as input is described in Chap. 3. The main results are given in Chap. 4, where more detailed case-specific portrayal is offered. The concluding remarks appear in Chap. 5.

Chapter 2

Quantum chemical methods

One of the main challenges in condensed matter physics, and also in theoretical chemistry, is the need to find good, workable approximations to the many-body problem that contains the essence of the physics involved in the particular problem, and to obtain as accurate solutions as possible. *Ab initio* methods are the most unbiased tools in theoretical chemistry, and truly independent of the experiment they seek to model. Without any additional extensions to the postulates of basic quantum and relativistic mechanics, these methods can closely approximate and explain the majority of static features of molecular physics and chemistry.

The approach in the present study for deriving the final computational results relies on accurate pair-information that can be obtained by various techniques. Because only diatomic calculations need to be performed, the most advanced quantum chemical methods available are computationally feasible. In particular, the Coupled Cluster and Multireference Configuration Interaction (MRCI) methods, although very different in nature, are both regarded [21–24] as highly accurate techniques yielding results close to the full CI (FCI) limit.

The magnetic interactions considered in this thesis are related to the resonance effecs which form the basis of the EPR spectroscopy. They arise from the coupling of the electron spin magnetic moment to an external magnetic field and to the nuclear spins in the system. The origin of these effects can be unraveled by relativistic[1] treatment of quantum mechanics and they are manifested as

---

[1] Although, as discussed on p. 15, relativity is not necessarily required.

the fine and hyperfine structures, respectively. The actual numerical treatment, however, may be carried out in the nonrelativistic regime using ordinary one-component wavefunctions and operators in a perturbative manner.

2.1 Computing the energy

The theoretical foundation for most molecular energy evaluations in quantum chemistry is the nonrelativistic time-independent Schrödinger equation that is formulated within the Born-Oppenheimer approximation of fixed nuclei [25]. The antisymmetry requirement of the fermion statistics (the Pauli exclusion principle) is fulfilled by the determinantal form of the many-electron wavefunction (Slater determinant), or by using occupation number representation of the second quantization [24,26,27]. The resulting matrix eigenvalue equations of the Hartree-Fock molecular orbital (MO) approximation constitute the zero-order solution to the electronic problem [27]. It is not intended to dwell upon the details of these basic issues here, but merely to discuss some important matters that influence the accuracy of the results.

The Hartree-Fock self-consistent field (HF-SCF) method is a mean field assumption that does not account for electron correlation. The interest in quantum chemistry is mainly in energy differences, e.g. in binding energies that are only a fraction of the total energy of a system; hence it becomes essential to include these higher-order effects into the model when accurate results are needed. This translates into filling the energy gap $E_{\text{exact}} - E_{\text{HF}}$ by post-HF electron correlation methods designed for this purpose.

Most of the applied methods can be characterized as being either variational or perturbational. The advantage of the former is the guaranteed existence of bounds for the energy. The CI (and HF) methods provide an upper bound to the exact energy of the system, whereas many-body perturbation theories (MBPT) usually have an oscillatory convergence or they may even diverge [24, 28]. Coupled Cluster methods are also nonvariational (in the usual formulation) but they behave more smoothly [23]. More crucial than the variational nature of the method is, however, the concept of scaling.

A method that gives linear scaling for energy of N noninteracting systems is correct, and the proper scaling of the energy with the number of all correlated particles is thus termed size-extensivity [29]. This is a property that truncated

CI methods generally lack, while the above mentioned other methods satisfy it. A somewhat more pragmatic criterion is the property called size-consistency [30], which requires that the energy of two infinitely separated systems is the sum of the individual system energies. This corresponds to correct dissociation of a molecule to atomic fragments which, again, is a serious problem with CI methods.

Another aspect in the treatment of electron correlation is the division into dynamic and static effects. The former is attained by generating excited electron configurations out of the reference function and including them into the wavefunction with proper weight. The single configuration description for reference becomes inadequate when static correlations predominate. Instead, a simultaneous optimization of both self-consistent orbitals and coefficients of several configurations (multiconfiguration method [31]) that are important for a qualitative description of the reference function, can be used.

The choice of approach for a particular case is also dependent on the electronic state one needs to calculate. The perturbative methods described above are of ground state nature and can give only the lowest state of a particular spin and symmetry. Basically, the same argument applies for the Coupled Cluster methods, although a means to describe excited states within the scheme is provided by the equation-of-motion Coupled Cluster (EOM-CC) method [32]. This is not discussed further or used in the present work. With the (MR)CI methods, however, the excited states are straightforwardly given as eigenvalues of the variational diagonalization problem in the spanned configuration space.

The essence of MO theory is in the construction of N-particle and one-particle spaces. The discretization of the one-particle space to a finite set of basis functions is a fundamental approximation and defines the limit of accuracy that can be computationally gained. In most cases the N-particle space expanded as a set of linear combinations of basis functions must also be truncated. This produces the methodological hierarchy that converges toward the full CI limit.

In the present study of matrix isolated atoms and molecules special attention must be focussed on the basis sets due to the weak interactions and large interatomic distances involved. The basis sets must contain adequately diffuse functions to account for the fluctuations of the electron clouds in van der Waals (vdW) region. The incompleteness of the basis, however, artificially increases the binding strengths, which in these complexes may even be of comparable magnitude to the actual interaction, and needs therefore to be taken care of.

This basis set superposition error (BSSE) [33] is most conveniently corrected by the counterpoise procedure (CP) [34].

Magnetic properties, as can be seen from their operator form in Section 2.2, depend heavily on the wavefunction at or near the nuclei. This puts an additional demand on the Gaussian-type basis functions as they must fulfill the cusp condition at the nucleus. When absolute values are aimed at, the usual solution is to augment the basis set with tight functions and possibly uncontract the inner region of the standard set. In a more specialized approach one utilizes Hiller-Sucher-Feinberg operators instead of the delta function [35, 36] for the evaluation of the spin density. However, when relative values are sought, as in the present study, it is essential to add diffuse functions to account for the effect of matrix perturbations mediated via the outer part of the wavefunction on spin density.

2.1.1 Coupled Cluster and Configuration Interaction

The above methodological difference that affects the size-extensivity is inherent in the procedure that generates the particle-hole excitations within the N-electron space in CI and Coupled Cluster schemes. Namely, the linear parametrization of the CI wavefunction [27],

$$|\Psi_{\mathrm{CI}}\rangle = \big(1+\hat{C}\big)|\Phi_0\rangle\,, \tag{2.1}$$

as compared to the exponential ansatz of the Coupled Cluster theory [37],

$$|\Psi_{\mathrm{CC}}\rangle = e^{\hat{T}}|\Phi_0\rangle\,, \tag{2.2}$$

is deficient since it does not yield correct quantum mechanical description for many-body interactions if $\hat{C}$ is truncated in the usual way:

$$\begin{aligned}\hat{C} &= \hat{C}_1 + \hat{C}_2 + \cdots \\ &= \sum_{ia} c_i^a a_a^\dagger a_i + \frac{1}{4}\sum_{ijab} c_{ij}^{ab} a_a^\dagger a_b^\dagger a_j a_i + \cdots\end{aligned} \tag{2.3}$$

This form produces the singles and doubles CI (CISD) wavefunction where correspondingly excited determinants having holes in the occupied space (i,j) and electrons promoted to the virtual space (a,b) are included with expansion coefficients c_i^a, c_{ij}^{ab}. The creation and annihilation operators of the second quantization $a_a^\dagger, a_i$ act on the Fermi vacuum (HF-reference function) ket vector $|\Phi_0\rangle$ producing the excited configurations. In this formulation, the CI method then comprises the variational optimization of these coefficients subject to the intermediate normalization constraint $\langle \Phi_0 | \Psi_{\mathrm{CI}} \rangle = 1$, i.e., the minimization of the expectation value of the energy. The technical solution to this eigenvalue problem consists of diagonalization of the Hamiltonian matrix in the configuration basis, or it may be accomplished by special iterative techniques [24].

The Coupled Cluster operator $e^{\hat{T}}$, on the other hand, expands with a similar truncation as above to give

$$\begin{aligned} |\Psi_{\mathrm{CC}}\rangle = \big(1 &+ \hat{T}_1 + \hat{T}_2 + \hat{T}_3 + \ldots \\ &+ \frac{1}{2!}\hat{T}_1^2 + \hat{T}_2\hat{T}_1 + \frac{1}{3!}\hat{T}_1^3 \\ &+ \frac{1}{4!}\hat{T}_1^4 + \frac{1}{2!}\hat{T}_2\hat{T}_1^2 + \hat{T}_3\hat{T}_1 + \frac{1}{2!}\hat{T}_2^2 + \ldots\big)|\Phi_0\rangle \end{aligned} \tag{2.4}$$

which includes ***disconnected*** wavefunction components as operator products, where the total cluster operators are [38]:

$$\hat{T}_1 \equiv \sum_i \hat{t}_i = \sum_{ia} t_i^a a_a^\dagger a_i \tag{2.5}$$

$$\hat{T}_2 \equiv \frac{1}{2}\sum_{ij} \hat{t}_{ij} = \frac{1}{4}\sum_{ijab} t_{ij}^{ab} a_a^\dagger a_b^\dagger a_j a_i \tag{2.6}$$

and generally

$$\hat{T}_n = \left(\frac{1}{n!}\right)^2 \sum_{ij\ldots ab\ldots} t_{ij\ldots}^{ab\ldots} a_a^\dagger a_b^\dagger \ldots a_j a_i \,. \tag{2.7}$$

The truncation at a specific excitation level gives the hierarchy of the Coupled Cluster techniques, e.g., CCSD, CCSDT, etc. Due to the disconnected terms the Coupled Cluster state contains contributions from all the excitation levels in the FCI wavefunction even when truncated, as can be seen in the following comparison for $\hat{C} = e^{\hat{T}} - 1$:

$$\begin{aligned} \hat{C}_1 &= \hat{T}_1 \\ \hat{C}_2 &= \hat{T}_2 + \frac{1}{2}\hat{T}_1^2 \\ \hat{C}_3 &= \hat{T}_3 + \hat{T}_2\hat{T}_1 + \frac{1}{6}\hat{T}_1^3 \\ \hat{C}_4 &= \hat{T}_4 + \hat{T}_3\hat{T}_1 + \frac{1}{2}\hat{T}_2\hat{T}_1^2 + \frac{1}{2}\hat{T}_2^2 + \frac{1}{24}\hat{T}_1^4 \,, \\ &\vdots \end{aligned}$$

and is therefore always size-extensive, whereas CI methods become fatally flawed for large systems. Furthermore, the deficiency of the CI methods can be related to the lack of multiplicative separability of the wavefunction for noninteracting subsystems (e.g. largely separated A and B) $|\Psi\rangle \nrightarrow |\Psi_{\mathrm{A}}\rangle|\Psi_{\mathrm{B}}\rangle$ and, therefore, to the lack of additively separable energy $E \nrightarrow E_{\mathrm{A}} + E_{\mathrm{B}}$.

A convenient and preferred way to obtain the Coupled Cluster energy and amplitude equations is to proceed with similarity-transformed Hamiltonian $\bar{H} \equiv e^{-\hat{T}}\hat{H}e^{\hat{T}}$ formed by left-multiplying the Schrödinger equation, and then by projecting with respect to the reference and excited determinants. This gives

$$\langle\Phi_0|e^{-\hat{T}}\hat{H}e^{\hat{T}}|\Phi_0\rangle = E \tag{2.8a}$$

$$\langle\Phi_{ij\dots}^{ab\dots}|e^{-\hat{T}}\hat{H}e^{\hat{T}}|\Phi_0\rangle = 0\,, \tag{2.8b}$$

where the energy expression (2.8a) is decoupled from the nonlinear amplitude equations (2.8b), meaning that the cluster amplitudes $t_{ij\dots}^{ab\dots}$ can be obtained independently of the energy. This formulation is necessitated for extending the Coupled Cluster theory beyond the calculation of energies. The Hausdorff expansion for evaluating $\bar{H}$ does not give an infinite series, but the five term expansion

$$\begin{aligned} e^{-\hat{T}}\hat{H}e^{\hat{T}} =& \hat{H} + \left[\hat{H},\hat{T}\right] + \frac{1}{2}\left[\left[\hat{H},\hat{T}\right],\hat{T}\right] + \frac{1}{3!}\left[\left[\left[\hat{H},\hat{T}\right],\hat{T}\right],\hat{T}\right] \\ &+ \frac{1}{4!}\left[\left[\left[\left[\hat{H},\hat{T}\right],\hat{T}\right],\hat{T}\right],\hat{T}\right]\,, \end{aligned} \tag{2.9}$$

that truncates naturally due to the (anti-)commutation properties of the cluster operator $\hat{T}$ and the electronic Hamiltonian, which in second-quantized form is written as [27]

$$\hat{H} = \sum_{pq} h_{pq} a_p^\dagger a_q + \frac{1}{4}\sum_{pqrs}\langle pq||rs\rangle a_p^\dagger a_q^\dagger a_s a_r\,. \tag{2.10}$$

This involves matrix elements for the one-electron component in the Hamiltonian, $h_{pq} \equiv \langle p|\hat{h}|q\rangle$, and $\langle pq||rs\rangle \equiv \langle pq|rs\rangle - \langle pq|sr\rangle$ is the antisymmetrized two-electron part including all the electron-electron interaction integrals. The general spin-orbital indices in (2.10) refer to both occupied and virtual subspaces. Derivation of the analytical expressions for the amplitudes and the energy then comprises the evaluation of the commutators of creation/annihilation operator products. The tedious commutator algebra can be significantly reduced by Wick's theorem and normal ordering, and even further by diagrammatic techniques [38]. Without entering into the details, it is inherent in these techniques that termwise size-extensivity is ensured, which allows all kinds of truncations to be made for the cluster expansion.

The close connection to many-body perturbation theory with Møller-Plesset (MP) partitioning allows one to evaluate the MPn energies along with the Coupled Cluster calculation [39, 40]. As the CCSDT method is computationally far too expensive at present, it is no surprise that perturbative estimates for inclusion of connected triples contributions have been developed. The method called CCSD(T) is presently the most accurate one, being at the same time a computationally feasible, single reference method [41]. It includes terms that can be related by perturbational analysis up to fifth order excitations and works even in cases with substantial static correlation effects [23, 38].

When excited states having lower energy roots in the same symmetry are considered, or static correlation effects require several configurations for the reference, a balanced description is attained by a multiconfiguration self-consistent field (MCSCF) based method. The MCSCF wavefunction

$$|\Psi_{\mathrm{MC}}\rangle = \sum_{I}^{M} c_I |\Phi_I\rangle \tag{2.11}$$

is a truncated linear CI expansion that contains the essential number of M configurations to give qualitatively correct description of the electronic structure and, for example, all possible dissociation pathways. The difference with the CI methods is that the orbitals are also relaxed in addition to the expansion coefficients c_I, that is, the variational energy minimization [24]

$$E = \min_{\kappa, \mathbf{C}} \frac{\langle \kappa, \mathbf{C} | \hat{H} | \kappa, \mathbf{C} \rangle}{\langle \kappa, \mathbf{C} | \kappa, \mathbf{C} \rangle} \tag{2.12}$$

contains the parametrization

$$|\kappa, \mathbf{C}\rangle = \exp(-\hat{\kappa}) \sum_{I}^{M} c_I |\Phi_I\rangle \, , \tag{2.13}$$

where the orbital rotation operator $\exp(-\hat{\kappa})$ carries out unitary transformations among the spin-orbitals. The selection of included configurations $|\Phi_I\rangle$ is automatized in complete active space SCF (CASSCF) method, that generates a full CI expansion in a chosen set of molecular orbitals. Usually this is taken to be the valence space.

To recover as much of the correlation energy as possible, as in a single reference case, it is essential to go beyond multiconfiguration SCF scheme and to solve the dynamical correlation problem. The MRCI approach approximates the wavefunction as an expansion in all singly and doubly excited configurations (external) with respect to a set of chosen reference configurations (internal). This can be written as [42–44]

$$|\Psi_{\mathrm{MRCI}}\rangle = \sum_{I} c_I|\Phi_I\rangle + \sum_{ta,I} c^a_{t,I}|\Phi^a_{t,I}\rangle + \sum_{tuab,I} c^{ab}_{tu,I}|\Phi^{ab}_{tu,I}\rangle\,, \tag{2.14}$$

where the indices (t, u) refer to the internal valence orbitals occupied in the MC- or CAS-reference function. A more efficient formulation which avoids the rapid increase of the basis size with number M is the so-called internally contracted MRCI [44–46]. Instead of selecting excitations from each reference configuration, it constructs configurations by applying excitation operators to the reference wavefunction as a single entity. Therefore, the number of configurations becomes independent of M and depends only on the number of internal and external orbitals. This reduces the size of the CI expansion by one or two orders of magnitude.

Two methods have been used to approximatively attain size-extensivity in the present study when the Coupled Cluster has not been applicable. With MRCI calculations, a multireference analogue of the simple Davidson rescaling correction [47, 48] has been routinely applied for approximating the disconnected quadruple excitations. This has the effect of removing the contributions from unlinked diagrams that enter the CI matrix elements and are absent in CC equations by construction. Another treatment is adopted in quadratic configuration interaction (QCI) methods. The QCISD, for example, is derived by adding a few of the terms in the $e^{\hat{T}}$ power series expansion to the CISD in order for it to approach size-extensivity in a rigorous manner [49].

2.1.2 Basis sets

The description of one-particle spaces in the present set of studies is based on the so-called correlation-consistent basis sets of Dunning and co-workers [50]. These basis sets have become one of the standard functions due to their extensive benchmark testing [51]. The acronym x-aug-cc-pVXZ reads x times diffusively augmented correlation-consistent polarized valence X-tuple zeta basis set, where the cardinal number X takes values D, T, Q, 5,... for doubly, triply, quadruply, quintuply, etc., split sets. When it is important to account explicitly for the core correlation in a property evaluation, the basis sets named cc-pCVXZ are utilized for their additional flexibility.

As the number of basis functions (M) and, therefore, integrals to be calculated and stored, increases rapidly when extensive basis sets are used, it is plausible to describe the core region effectively by a single function or potential. This is called effective core potential (ECP) or pseudopotential (PP) method, and is usually applied to heavy atoms. In addition to the reduced computational effort that scales at least as M^4, incorporation of scalar relativistic and spin-orbit effects important for heavy atoms can be carried out efficiently. In the present work the chosen potentials for Rg atoms are the relativistic ECP's of the Stuttgart group [52]. These potentials represent the Rg^{8+} core, containing the spin-orbit parametrization, whereas the valence part is described by contracted $[4s\,4p\,3d\,1f]$ set of Gaussians that was further augmented by a $\{spdf\}$ set of optimized diffuse functions in paper I. Nicklass *et al.* [52] give the following form for the pseudopotential part

$$V_{\mathrm{PP}}(\boldsymbol{r}_i) = -\frac{Q}{r_i} + \sum_{l=0}^{l_{max}} \left[\sum_k B_{lk}\, e^{-\beta_{lk} r_i^2} \right] P_l \, , \tag{2.15}$$

where the core charge $Q = 8$ for Rg atom, P_l denotes a projection operator on spinor spherical harmonics centered at Rg atom

$$P_l = \sum_{m=-l}^{l} |Y_{lm}\rangle\langle Y_{lm}| \, , \tag{2.16}$$

and the pseudopotential parameters B_{lk} and β_{lk} are adjusted to represent the scalar-relativistic all-electron energies. The spin-orbit operator has the form [52]

$$V_{\mathrm{SO}}(i) = \sum_{l=1}^{l'_{max}} \frac{2\,\Delta V_{\mathrm{SO},l}(r_i)}{2l+1} P_l\, \boldsymbol{l}_i \cdot \boldsymbol{S}_i\, P_l \tag{2.17}$$

with $\boldsymbol{l}_i$ and $\boldsymbol{S}_i$ denoting the orbital angular momentum and spin operator of the ith valence electron. The difference $\Delta V_{\mathrm{SO},l}$ of the radial parts of the two-component relativistic pseudopotentials $V_{\mathrm{PP},l,l+1/2}$ and $V_{\mathrm{PP},l,l-1/2}$ is written in terms of Gaussian functions as

$$\Delta V_{\mathrm{SO},l}(r_i) = \sum_k \Delta B_{lk}\, e^{-\beta_{lk} r_i^2} \, . \tag{2.18}$$

The exponential parameters are the same as above in (2.15), hence only the linear parameters ΔB_{lk} are least-squares optimized to reproduce spin-orbit splittings of the reference data.

2.2 Computing the magnetic properties

Paramagnetic resonance studies carried out in the microwave frequency range (10^9–10^{11} Hz) belong to the domain of EPR spectroscopy. It involves magnetic dipoles of electrons that originate from permanent magnetic moments due to the electron spin and orbital motion. The two paramagnetic resonance effects of concern for the present study are the electronic Zeeman and hyperfine interactions. The former is basically a coupling between the electron magnetic moment and the external magnetic field, mediated by the g-factor, or more generally, by a second-rank (3×3) g-tensor, where the orbital contributions introduce the environmental anisotropy into the description. The phenomenological expression for the Zeeman energies leading to the resonance condition can be written as

$$h\nu = -\boldsymbol{\mu} \cdot \boldsymbol{B} = \mu_B \boldsymbol{S} \cdot \mathbf{g} \cdot \boldsymbol{B} \,, \tag{2.19}$$

where μ_B is the Bohr magneton, and the g-tensor having elements g^{ab} in terms of Cartesian axes $a, b \in \{x, y, z\}$ parametrizes the orientational dependence of the resonance. Quite similarily, the hyperfine interaction between the electron and nuclear spins is mediated by the traceless A-tensor,

$$h\nu \propto \boldsymbol{S} \cdot \mathbf{A} \cdot \boldsymbol{I} \,, \tag{2.20}$$

which contains the isotropic Fermi contact (FC) and the anisotropic spin dipolar (SD) contributions. The relevant Hamiltonian terms for describing the tensors[1] **g** and **A** are needed to give an explicit connection between experimentally derived parameters and molecular structure. To clarify these matters, the energy levels showing Zeeman and isotropic hyperfine splittings are drawn in Fig. 2.1 for $S = 1/2$, $I = 1/2$ case according to the Breit-Rabi solution, in which the magnetic Hamiltonian is diagonalized in the basis of spin states $|m_s\, m_I\rangle$ [18].

These properties are spin-dependent and arise naturally from the relativistic theory which is roughly sketched in the following. The traditional approach for arriving at the practical expressions that parametrize the interactions is to start from the four-component Dirac equation, to apply the minimal substitutions (Lorentz gauge) for the field-dependent operators, and to reduce the equations to a two-component form (Pauli limit) by decoupling the electronic and positronic components. Generalization to the many-particle case is carried out by the Breit formalism, which after a similar reduction to nonrelativistic form leads to the so-called Breit-Pauli (BP) equation that at least to a good approximation explains all the interactions between matter (molecules) and electromagnetic field [53, 54]. However, radiative corrections of quantum electrodynamics are needed to bring the free electron g-value from the predicted number of 2 to the correct g_e of 2.0023193.

---

[1] Actually interaction matrices, in general. The term *tensor* is valid here, nevertheless.

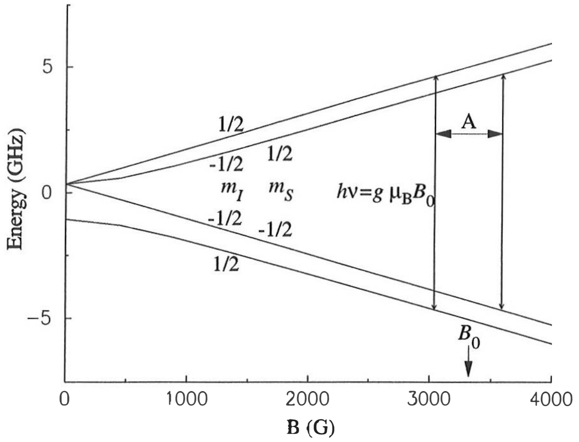

Figure 2.1: The Breit-Rabi levels for $|m_s\, m_I\rangle$ states of an electron interacting with a nucleus with spin $\frac{1}{2}$ as in H atom. The allowed magnetic dipole transition is split due to the hyperfine coupling.

It should be noted that a revised point of view to the origin of the spin and the magnetic moment of the electron is provided by the Lévy-Leblond equation, which results as a nonrelativistic limit of the Dirac equation by a change of the metric in the four-component spinor space [55, 56]. It was shown by Lévy-Leblond [57] that the electron spin is perfectly consistent with a Galilei-invariant (i.e. nonrelativistic) field theory, and that the corresponding equation arises also from group theory of spin-half particles which describes the spin correctly and also accounts for its gyromagnetic ratio $g = 2$. Therefore, it is not necessary to consider the electron spin as a genuine relativistic effect.

Taking into account all the Breit-Pauli terms linear in $\boldsymbol{B}$ or $\boldsymbol{S}$, as Eq. (2.19) suggests, one ends up with a Hamiltonian that has seven terms contributing to the g-tensor,

$$\begin{aligned} H_g = H_{\mathrm{SZ}} + H_{\mathrm{RMC-SZ}} + H_{\mathrm{GC-SZ}}(1e) + H_{\mathrm{GC-SZ}}(2e) \\ + H_{\mathrm{SO}}(1e) + H_{\mathrm{SO}}(2e) + H_{\mathrm{OZ}}\,. \end{aligned} \tag{2.21}$$

These terms are identified as spin-Zeeman operator, relativistic mass correction to the spin-Zeeman, one- and two-electron spin-Zeeman gauge corrections, one- and two-electron spin-orbit terms, and orbital-Zeeman operator, respectively [54]. The spin-Zeeman operator, $g_e \mu_B \boldsymbol{S} \cdot \boldsymbol{B}$, is the dominant part of the interaction, whereas the rest produce the deviation from the free electron value g_e. Thus, the g-tensor may be expressed in the form $g^{ab} = g_e \delta^{ab} + \Delta g^{ab}$, where

Δg^{ab} are the components of the g-shift [58]. The hyperfine components are already present in the BP equation, given that electron magnetic moment vector $-g_e\mu_B\boldsymbol{S}$ is replaced by a nuclear one, $\boldsymbol{\mu}_K = g_K\mu_N\boldsymbol{I}_K$, where μ_N is the nuclear magneton, $\boldsymbol{I}$ is the total nuclear angular momentum, i.e., nuclear spin, and g_K is the g-factor specific to the nucleus K.

Since the magnetic effects are generally very small compared to other energetics in the low external fields of an EPR measurement, the perturbation theory is conceptually well suited for quantifying the effects of the corresponding operators. In this approach, the electronic problem is first solved to give a reasonable (nonrelativistic) field-free description of the system as discussed in Section 2.1, and then the magnetic operators are used in the Rayleigh-Schrödinger perturbation theory (RSPT) to produce the induced small changes in the energy. The perturbed Hamiltonian is conveniently expressed in a form $H = H_0+\lambda V = H_0+\lambda\mathbf{P}_1+\lambda^2\mathbf{P}_2$. The first- and second-order energy corrections in terms of complete set of eigenfunctions $\{\Psi_j^{(0)}\}$ are thus [26, 27]

$$E_i^{(1)} = \langle\Psi_i^{(0)}|\mathbf{P}_1|\Psi_i^{(0)}\rangle \tag{2.22}$$

$$E_i^{(2)} = \langle\Psi_i^{(0)}|\mathbf{P}_2|\Psi_i^{(0)}\rangle + \sum_{j\neq i}\frac{\langle\Psi_i^{(0)}|\mathbf{P}_1|\Psi_j^{(0)}\rangle\langle\Psi_j^{(0)}|\mathbf{P}_1|\Psi_i^{(0)}\rangle}{E_i^{(0)} - E_j^{(0)}}, \tag{2.23}$$

where (Ψ_j, E_j) are the field-independent solutions. All the operators affecting the tensors $\mathbf{g}$ and $\mathbf{A}$ in the linear approximation are of $\mathbf{P}_1$-type, since the perturbation in the former is only the external magnetic field and in the latter the nuclear field. In addition, the terms that appear quadratic in the second-order contribution are dropped. The reasoning for using the RSPT also applies for derivative techniques where the field-effects are handled as responses of the system to the perturbation. While the above expressions are perfectly valid for exact wavefunctions, the response approach holds strictly for approximate wavefunctions also [26],

$$\left.\frac{\partial E_i}{\partial\lambda}\right|_{\lambda=0} = \langle\Psi_i^{(0)}|\mathbf{P}_1|\Psi_i^{(0)}\rangle + 2\left\langle\frac{\partial\Psi_i^{(0)}}{\partial\lambda}\middle|H_0\middle|\Psi_i^{(0)}\right\rangle \tag{2.24}$$

and is used with the aid of a Lagrangian function for calculation of the hyperfine properties in the present set of studies.

The hyperfine FC and SD properties are calculated along with the energy evaluation from normalized spin densities by standard methods [58,59]. The evaluation of the g-tensor is, however, more laborious for it requires a detailed knowledge of the electronic structure of both ground and excited states. However, the problem can be avoided using the response equations of the propagator methods since the excited states are then handled only implicitly, and no truncation in the sum-over-states expansion shown in Eq. (2.23) is needed [60,61].

Two commercial program packages were used for computing the wavefunction and several properties, as cited in the original articles, throughout this study. All the MRCI and related computations were carried out with the MOLPRO set of codes [62], as well as the RHF-based (spin-restricted open shell) Coupled Cluster energy calculations. The hyperfine calculations were performed with the GAUSSIAN package [63], with various levels of theory, however, all based on an UHF-reference (unrestricted) description. It is noted that the open shell UHF determinant is not a pure spin state and it suffers from the spin contamination, i.e. the expectation value of $\boldsymbol{S}^2$ becomes higher than the correct 0.75 for a doublet, which may affect the computation of magnetic properties. However, a quantitative investigation on the extent of this effect in open shell Coupled Cluster wavefunctions has shown that modestly spin contaminated reference states are not a valid concern [64]. A popular method of removing unwanted higher multiplicity states is to project them out with a suitable projection operator.

2.2.1 Fine structure

The term *fine structure* in the context of the electronic Zeeman effect can be rationalized in two ways. First, it is a splitting of energy levels as the Kramer's degeneracy is lifted in the presence of magnetic field. Secondly, a large contribution to the g-shift originates from spin-orbit interaction that is generally termed as a fine structure correction to the nonrelativistic energy.

The operators in Eq. (2.21) for molecular g-tensor evaluation have been only recently included in the *ab initio* level calculations [65]. In the present study it was sufficient just to concentrate on the dominating second-order contribution. The three correction terms in Eq. (2.21) all appear as first-order, since their contribution to the second-order leads to quadratic dependence on $\boldsymbol{S}$ or $\boldsymbol{B}$ or both. Therefore, only the spin-orbit and orbital-Zeeman operators are effective, and the bilinear perturbation formula is [54,58]

$$E_{\mathrm{Zeeman}} = 2\sum_{n\neq 0} \frac{\langle\Psi_0|H_{\mathrm{SO}}|\Psi_n\rangle\langle\Psi_n|H_{\mathrm{OZ}}|\Psi_0\rangle}{E_0 - E_n}\,, \tag{2.25}$$

where the matrix elements between ground $|\Psi_0\rangle$ and excited $|\Psi_n\rangle$ states are calculated with the MRCI wavefunctions.

The spin-orbit operator is written in terms of the fine structure constant $\alpha = e^2/(\hbar c) = 1/137.036$ (in Gaussian units) as

$$\begin{aligned} H_{\mathrm{SO}}(1e) &= \frac{g_e \mu_B \alpha \hbar}{2mc} \sum_{i=1}^{N} \sum_{K=1}^{N_K} \frac{Z_K}{r_{iK}^3} \boldsymbol{S}_i \cdot \boldsymbol{l}_{iK} \\ H_{\mathrm{SO}}(2e) &= -\frac{g_e \mu_B \alpha \hbar}{2me} \sum_{i=1}^{N} \sum_{j=1}^{N} \frac{1}{r_{ij}^3} (\boldsymbol{S}_i + 2\boldsymbol{S}_j) \cdot \boldsymbol{l}_{ij} \, , \end{aligned} \tag{2.26}$$

and the orbital-Zeeman term is given by

$$H_{\mathrm{OZ}} = -\frac{\alpha \hbar}{2me} \sum_{i=1}^{N} \boldsymbol{B} \cdot \boldsymbol{l}_{iC} \, , \tag{2.27}$$

where the indices i, j and K refer to summation over electrons and nuclear centres, respectively. The orbital-Zeeman term is gauge-dependent, since the angular momentum operator $\boldsymbol{l}_{iC} = (\boldsymbol{r}_i - \boldsymbol{C}) \times \boldsymbol{p}_i$ is defined in terms of some arbitrarily chosen computational origin $\boldsymbol{C}$. The computed matrix elements can be directly related to the g-shift components Δg^{ab} provided they are considered in a spin-field dimension reduced form [65].

The calculations described above are utilized in the paper IV.

2.2.2 Hyperfine structure

The hyperfine interaction splits the Zeeman energy levels further; thus additional resonances occur in the spectrum at different field strengths. The fine structure contributions arise in a Coulombic field of pure point charges, whereas the nuclear magnetic moments generated from the internal nucleon structure give birth to additional effects orders of magnitude smaller than those of the fine structure. Hence the term *hyperfine*.

The Breit-Pauli equation gives the following Hamiltonian for the hyperfine interactions that are of present interest:

$$\begin{aligned} H_{hf} = -g_e \mu_B \mu_N \sum_{i=1}^{N} \sum_{K} g_K \Bigg(& \frac{\boldsymbol{S}_i \cdot \boldsymbol{I}_K}{r_{iK}^3} - 3 \frac{(\boldsymbol{S}_i \cdot \boldsymbol{r}_{iK})(\boldsymbol{I}_K \cdot \boldsymbol{r}_{iK})}{r_{iK}^5} \\ & - \frac{8\pi}{3} \delta(\boldsymbol{r}_{iK}) \boldsymbol{S}_i \cdot \boldsymbol{I}_K \Bigg) \, , \end{aligned} \tag{2.28}$$

including a sum of two first-order contributions corresponding to the dipolar and Fermi contact terms. There are also correction terms that enter into the A-tensor description, but those are generally considered negligible [54].

The interface between experimental and theoretical work in EPR is based on the so-called spin Hamiltonian (sH) formalism. This model allows the measured data to be analyzed in terms of a small number of parameters, which can be interpreted by the theoretical approach as well. The idea is to write an effective Hamiltonian that comprises only spin operators, the external magnetic field, and measurable parameters, and to produce the same energy levels, when solved in a basis of pure spin states $\{\,|m_s m_I\rangle\,\}$, that Eq. (2.28) gives with calculated wavefunctions.

The spin Hamiltonian can be written for the present case (S = 1/2) as

$$H_s = \mu_B \boldsymbol{S} \cdot \mathbf{g} \cdot \boldsymbol{B} - \mu_N \sum_K g_K \boldsymbol{B} \cdot \boldsymbol{I}_K + \boldsymbol{S} \cdot \sum_K \mathbf{A}_K \cdot \boldsymbol{I}_K \,, \tag{2.29}$$

which upon diagonalization produces the magnetic field values for transition. On the other hand, this operator is subject to the first-order relation [58]

$$\langle m_s' m_I' | H_s^{(1)} | m_s m_I \rangle = \langle \Psi_0' | \mathbf{P}_1 | \Psi_0 \rangle \,, \tag{2.30}$$

where the sH matrix elements must be in correspondence with the theoretical ones. This equivalence can indeed be satisfied [54]. So, for the Fermi contact part in the perturbation expression, one gets (in spherical tensor form)

$$\begin{aligned} \langle \Psi_0' | H_{\mathrm{FC}} | \Psi_0 \rangle &= \frac{8\pi}{3} g_e \mu_B \mu_N \sum_K g_K D_S(\boldsymbol{r}_K) \\ &\times \sum_m (-1)^m \langle m_s' | S_m | m_s \rangle \langle m_I' | I_{-m}^K | m_I \rangle \\ &= \langle m_s' m_I' | H_{s,\mathrm{FC}}^{(1)} | m_s m_I \rangle \,, \end{aligned} \tag{2.31}$$

where

$$H_{s,\mathrm{FC}}^{(1)} = \sum_K h A_K^{\mathrm{iso}} \boldsymbol{S} \cdot \boldsymbol{I}_K \,, \tag{2.32}$$

and the isotropic coupling constant is (in Hz)

$$A_K^{\mathrm{iso}} = \frac{8\pi}{3} g_e \mu_B g_K \mu_N h^{-1} D_S(\boldsymbol{r}_K) \tag{2.33}$$

i.e., proportional to the normalized spin density $D_S(\boldsymbol{r}_K)$ evaluated at the nucleus. The dipolar interaction, written in tensor product form as

$$H_{\mathrm{SD}} = 3 g_e \mu_B \mu_N \sum_K g_K \sum_{i,m} (-1)^m r_{iK}^{-5} [\boldsymbol{r}_{iK} \times \boldsymbol{r}_{iK}]_{-m}^{(2)} [\boldsymbol{S}_i \times \boldsymbol{I}_K]_m^{(2)} \,, \tag{2.34}$$

can be treated in a similar manner and gives in a Cartesian representation the spin operator

$$H^{(1)}_{s,\mathrm{SD}} = \sum_{K,ab} hA^{\mathrm{dip}}_{K,ab} S_a I^K_b \,, \qquad (a,b = x,y,z) \tag{2.35}$$

where the anisotropic coupling constant is

$$A^{\mathrm{dip}}_{K,ab} = \frac{3g_e \mu_B g_K \mu_N}{h} \int \frac{(r_{1K})_a (r_{1K})_b - \frac{1}{3}\delta_{ab} r^2_{1K}}{r^5_{1K}} D_S(\boldsymbol{r}_1) d\boldsymbol{r}_1 \,. \tag{2.36}$$

The spherical tensors in the above expressions reflect merely the Wigner-Eckart theorem utilized in the derivation of these relations [59]. The one-particle reduced spin density function $D_S(\boldsymbol{r})$ yields the excess density of up-spin over down-spin electrons, given in terms of basis functions and expansion coefficients that define the spin density matrix, i.e., discretized representation of the S_z operator used, by $\sum_{\mu\nu} (\mathbf{D}_S)_{\mu\nu} \phi_\mu(\boldsymbol{r}) \phi^*_\nu(\boldsymbol{r})$.

Spin density is the key variable in these *ab initio* calculations. It is affected by spin polarization and electron correlation effects, and reflects the environmental structure in the vicinity of the paramagnetic species. It is also noted that the FC term is a s-wave contribution, whereas the SD term necessitates non-zero orbital angular momentum.

These matters were discussed in papers I, II, and IV.

Chapter 3

Molecular dynamics simulations

In the previous Sections only static, time-independent properties have been considered. In due course, dynamics is brought into debate, and the related methods are discussed. While the magnetic properties under investication are still the static ones, i.e. no spin-relaxation phenomena or other dynamical aspects of magnetic resonance are examined, the dependence of these parameters on atomic motion and configurations in finite (low) temperatures is explored by molecular dynamics (MD) simulations.

Very generally, molecular dynamics methods are devised to yield time averages of the physical quantities, approximately representing the experimentally observable values in a macroscopic time scale. Fortunately, the limited simulation time interval (picosecond scale) is usually sufficient, provided that the system samples the phase space to a reasonable extent. Thus, the physically correct thermodynamic description can be produced. The simulation of an infinite lattice corresponding to a macroscopic size scale is achieved by means of periodic boundary conditions. Therefore, the size of the system can be limited to the order of 10^2–10^3 explicitly defined atoms in a simulation.

In this Chapter the features of classical dynamics are pointed out at a general level and the assumption of pairwise additivity is discussed as it results from the use of quantum mechanical input data calculated for diatomic systems (previous Chapter). The symmetry of the electron density, i.e. the effect of an orbital angular momentum of the impurity atom, is stressed as it affects the adopted means of representation. In other words, the directional nature of chemical bonding and noncovalent interactions is considered in some detail.

In order to understand many chemical and physical processes it is essential to know the potential energy surfaces (PES). The set of PES is usually solved within the BO approximation and they depict the interatomic forces at various molecular electronic states. The symmetries of the states and the topologies of the surfaces define the static and dynamic behaviour of the system and its spectroscopic properties.

The fact that the whole potential energy surface must be known in dynamical studies is a computational bottleneck since the nuclear motion is usually handled relatively effortlessly by classical equations of the Newtonian dynamics. Progress in this area has been made by schemes [66, 67] based on density functional theory. These are, however, essentially ground state methods and, unfortunately, inadequately suited for studies on weak van der Waals interactions [68], mainly because of the lack of terms predicting the correct inverse power of R distance dependency. Although many processes are well represented with a single adiabatic surface, phenomena such as charge and electronic energy transfer reactions and nonadiabatic or spin-forbidden transitions necessitate detailed knowledge of the nonadiabatic interactions between states, and need to be computed with accuracy and efficiency.

Keeping these aspects in mind, the advantage of the presently applied methodology becomes evident. With accurate diatomic information it is possible to economically construct the PES for the whole system, in principle up to the exact BO-energy. This lies in the heart of the diatomics-in-molecules (DIM) theory [69, 70], initially used for constructing the potential energy matrices, and later utilized in MD simulations [71]. Moreover, although they are based on diatomic pair interactions, the DIM surfaces do not involve a simple assumption of pairwise additivity because of a peculiar mixture of various electronic states that is taken into account by rotational, spin coupling, and state mixing matrices [72, 73]. This is particularly profitable when studying chemical dynamics dictated by multi-body interactions. An example of this is the condensed phase molecular photodissociation, determined by recombination or cage exit of the fragments, and dependent on orbital reorientation dynamics [74].

The shortcoming of the classical treatment of the nuclear dynamics is, obviously, the neglect of quantum effects. In particular, zero point energy that may have a significant contribution to the amplitudes of the motion, is absent. Secondly, the continuous energy spectrum of nuclear motion and indefinable tunnelling are the inevitable, although not very severe, consequences of a classical study.

3.1 Isotropic case

Evaluation of forces is the most fundamental stage in the analysis of the deterministic equations of motion. Very generally, it can be assumed that the forces can be derived from a scalar potential which is a function of nuclear coordinates only. A simple and most frequently used additional condition is the pair-additivity. This is connected with the assumption of a single BO-surface, which does not hold when e.g. chemical bonds are formed or broken. The use of a single PES also implies angular isotropy of the electron density which is not always valid in the case of open shell atoms.

Moreover, the scalar potential neglects vectorial effects such as induction forces. The deviation from pair-additivity of Rg atoms, for example, arises from dispersion forces due to fluctuating electron distributions, and needs to be correlated vectorially, e.g. by the Axilrod-Teller three-body potential [75, 76]. The non-additivity may also arise from ionic pair contributions which necessitates the inclusion of the corresponding excited states in the DIM model [72].

In spite of the above, the pair-additive treatment is utilized here, and almost always by others too, with $l = 0$ atoms. This results in a method where the numerical integration of the equations of motion,

$$\begin{aligned} \mathbf{v}_i(t) &= \mathbf{v}_i(t-\delta t) + \delta t \left[\mathbf{F}^i_{AA}(t-\delta t) + \mathbf{F}^i_{AA}(t)\right]/2M_i \\ \mathbf{R}_i(t+\delta t) &= \mathbf{R}_i(t) + \mathbf{v}_i(t)\delta t + \delta t^2 \mathbf{F}^i_{AA}(t)/2M_i\,, \end{aligned} \tag{3.1}$$

as in the "velocity Verlet" algorithm (3.1) above, are solved with forces $\mathbf{F}_{AA} = -\nabla_{\mathbf{R}} E_A$. Here, the potential energy is described by a single function of nuclear coordinates

$$E(\{\boldsymbol{R}^n\}) = \sum_{i<j}^{n} V_{\mathrm{Rg}_i-\mathrm{Rg}_j} + \sum^{n} V_{\mathrm{X}-\mathrm{Rg}_i}\,, \tag{3.2}$$

that is, the state indices A always referring to a single PES only. Although this is strictly valid with closed shell atoms X such as hydrogen or alkali metal in Rg lattices (papers I, II), the triplet sulfur (paper III) becomes a more putative case if rigorous dependence on the electronic degrees of freedom were sought.

The application of the matters addressed above is realized in articles I–III. The actual simulation uses a sophisticated predictor-corrector integrator together with other standard algorithms of molecular dynamics [77] implemented in the MOLDY software [78], that was modified to account for the various aspects of present interest.

3.2 Anisotropic case

With open shell atoms ($l > 0$) the anisotropy of electron density and the multiplicity of electronic states due to the orbital degeneracy, and first of all, the breaking of this symmetry as a result of static or dynamic environmental effects, must be accounted for.

Quite generally, the anisotropic potentials can be described by the electrostatic expansion [79]

$$V_{{}^{M}P-{}^{1}S}(r, R_1, R_2, \ldots, R_N) = \sum_{k=1}^{N} \sum_{L=0}^{\infty} V_L(r, R_k) P_L(\boldsymbol{r} \cdot \boldsymbol{R}_k)\,, \tag{3.3}$$

where r is the electronic coordinate of an open shell atom X, R_k are the coordinates of the closed shell Rg atom, and P_L is a Legendre polynomial that can be expanded in spherical harmonics. The potential is evaluated as an expectation value over r in the basis of electronic wavefunctions of atom X.

The simplest case is $l = 1$, corresponding to a halogen atom (hole in p orbital) or a Group 13 atom (B, Al, etc.), which can be described on a one-particle basis $|m_l\rangle = Y_{1m}$ ($m = 1, 0, -1$) producing (if spin is neglected) a (3×3) matrix. The matrix elements are

$$V_{mm'} = \sum_{k} \sum_{L=0,2} \frac{4\pi}{2L+1} \langle Y_{1m}| \sum_{M=-L}^{L} Y_{LM} |Y_{1m'}\rangle\, V_L(R_k) Y^*_{LM}(\vartheta_k, \varphi_k)\,, \tag{3.4}$$

where the radial functions V_0 and V_2 represent the isotropic and anisotropic parts of X-Rg interaction, and can be written in terms of diatomic states as [79]

$$V_0 = \frac{1}{3}(V_\Sigma + 2V_\Pi) \tag{3.5a}$$

$$V_2 = \frac{5}{3}(V_\Sigma - V_\Pi)\,. \tag{3.5b}$$

The matrix elements can be evaluated with the Gaunt formula derived from the

Clebsch-Gordan series [80]

$$\int d\Omega \, Y^*_{lm}(\Omega) Y_{LM}(\Omega) Y_{l'm'}(\Omega) = (-1)^m \frac{\hat{l}\hat{L}\hat{l}'}{4\pi} \begin{pmatrix} l & L & l' \\ -m & M & m' \end{pmatrix} \begin{pmatrix} l & L & l' \\ 0 & 0 & 0 \end{pmatrix},$$

where $\hat{l} = \sqrt{2l+1}$ and the bracketed arrays are the $3j$-symbols for vector coupling. The adiabatic surfaces (3) are obtained by diagonalization of the potential energy matrix.

The above described first-order perturbation type approach is actually equivalent to the minimal basis DIM description. This limited basis is valid in the present studies, because the explored structures mainly correspond to near-equilibrium atomic configurations. Therefore, mixing of excited states into the three-state minimal basis manifold is negligible and the probability for surface-hopping transitions is extremely low. Generally, the DIM method is capable of handling a wide range of problems, so that the requirements of including excited states with ionic contributions, and/or treatment of separation into atomic fragments, cause no difficulty other than the increased complexity in implementation. This reflects the fact that DIM is essentially a valence bond theory.

While the DIM model is reviewed in detail elsewhere [70, 81], a brief outline is given here. For a system of N atoms the n-electron Hamiltonian H can be partitioned into a sum of atomic and diatomic fragment Hamiltonians,

$$H = \sum_{K}^{N} \sum_{L>K}^{N} H^{\mathrm{KL}} - (N-2) \sum_{K}^{N} H^{\mathrm{K}}, \tag{3.6}$$

where H^{K} and H^{KL} are the Hamiltonians for the atom K and the diatomic molecule KL, respectively. The total wavefunction Ψ_l can be expanded in terms of a complete set of polyatomic basis functions Φ_m,

$$\Psi_l = \sum_m \Gamma_{lm} \Phi_m . \tag{3.7}$$

The expansion coefficients Γ_{lm} and energies E_l are then the eigenvectors and eigenvalues of the matrix equation

$$\mathbf{H\Gamma} = \mathbf{S\Gamma E}, \tag{3.8}$$

where elements of the Hamiltonian matrix $\mathbf{H}$ are defined by

$$\begin{aligned} H_{mm'} &= \langle \Phi_m | H | \Phi_{m'} \rangle \\ H^{\mathrm{K}}_{mm'} &= \langle \Phi_m | \mathcal{A} H^{\mathrm{K}} | \phi_{m'} \rangle \\ H^{\mathrm{KL}}_{mm'} &= \langle \Phi_m | \mathcal{A} H^{\mathrm{KL}} | \phi_{m'} \rangle , \end{aligned} \tag{3.9}$$

since the polyatomic basis functions are constructed as the antisymmetrized product of the atomic wavefunctions $\phi_{m\nu}$:

$$\Phi_m = \mathcal{A} \prod_{\nu=1}^{N} \phi_{m\nu}(n_{\nu-1}+1, \ldots, n_\nu) \,. \tag{3.10}$$

Here, $\mathcal{A}$ is the n-electron antisymmetrizer and n_ν is the number of electrons of the first ν atoms. With linearly independent basis functions Φ_m the overlap matrix $\mathbf{S}$ will have a nonsingular inverse $\mathbf{S}^{-1}$, and the matrix equation can be written as

$$\mathbf{\Delta\Gamma} = \mathbf{\Gamma E} \,, \tag{3.11}$$

with definitions

$$\begin{aligned} \mathbf{\Delta} &= \mathbf{S}^{-1}\mathbf{H} \\ \mathbf{\Delta}^{\mathrm{K}} &= \mathbf{S}^{-1}\mathbf{H}^{\mathrm{K}} \\ \mathbf{\Delta}^{\mathrm{KL}} &= \mathbf{S}^{-1}\mathbf{H}^{\mathrm{KL}} \end{aligned} \tag{3.12}$$

so that $\mathbf{\Delta}$ is given exactly by

$$\mathbf{\Delta} = \sum_{K}^{N} \sum_{K>L}^{N} \mathbf{\Delta}^{\mathrm{KL}} - (N-2) \sum^{N} \mathbf{\Delta}^{\mathrm{K}} \,, \tag{3.13}$$

and the evaluation of an overlap matrix is thus avoided.

The basic approximation of DIM lies in selection of the atomic levels that give birth to the diatomic states, i.e. the finite number of polyatomic basis functions that are used to construct the whole system as a kind of a resonance structure. The Hamiltonian matrix $\mathbf{\Delta}$ is constructed in a fixed laboratory frame of reference with the aid of spin coupling $\mathbf{T}$, state mixing $\mathbf{B}$, and rotation matrices $\mathbf{R}$, so as to make the transformations from atomic and diatomic functions (defined in a coordinate frame suitable for the diatomic fragment), i.e. potential energy curves that are known from *ab initio* calculations or experiment. For example, the fragment Hamiltonian matrix is expressed as [70]

$$\mathbf{\Delta}^{\mathrm{KL}} = \mathbf{R}_{\mathrm{L}}^{\dagger}\mathbf{R}_{\mathrm{K}}^{\dagger}\mathbf{T}_{\mathrm{KL}}^{\dagger}\mathbf{B}_{\mathrm{KL}}^{-1}\mathbf{V}_{\mathrm{KL}}\mathbf{B}_{\mathrm{KL}}\mathbf{T}_{\mathrm{KL}}\mathbf{R}_{\mathrm{K}}\mathbf{R}_{\mathrm{L}} \,, \tag{3.14}$$

where the diagonal matrix $\mathbf{V}_{\mathrm{KL}}$ contains the known electronic states for the KL molecule. It is noted that the non-Hermitian formulation described above, i.e. Eq. (3.11), was not the one actually used in practice; the latter relied on the perturbational approach in the spirit of Ref. [71].

MD based on the DIM procedure utilizes the usual equations of motion (3.1), so that the force is evaluated from [82]

$$\frac{\partial \mathbf{E}}{\partial \mathbf{R}} \approx \mathbf{\Gamma}^{\dagger} \frac{\partial \mathbf{\Delta}}{\partial \mathbf{R}} \mathbf{\Gamma}\,, \tag{3.15}$$

where the Hamiltonian matrix elements are differentiated analytically. The dynamics can be run on various adiabatic states controlled by forces $\mathbf{F}_{AA}$, $\mathbf{F}_{BB}$, etc., or under a transition force, $\mathbf{F}_{AB}$, if nonadiabatic surface hopping is simulated.

The above procedure is adopted in papers IV and V in the simple perturbation type form, and the application to the present case of boron atom in Rg matrices is described in Section 4.3.

Chapter 4

Main results

4.1 Hydrogen and alkali metal atom trapping sites

The experimental background concerning the magnetic properties of spherically symmetric ^2S atoms H, Li, and Na is established in articles [12–18]. The theoretical description in papers I and II was aimed at providing a definite assignment of the spectral lines to specific trapping sites in rare gas matrices.

Common to all cases, the EPR transitions appear shifted from their free atom gas phase values, either positively or negatively. This is a result of perturbation of the spin density by the matrix, and can be explained as follows: In tight trapping sites the orbital overlap contracts the impurity atom's electron cloud resulting in increased A_{iso} values, whereas loose sites have the opposite effect of diminishing the A_{iso} due to dispersion interactions that enlarge the clouds. In other words, the situation can be viewed in terms of Pauli repulsion and vdW attraction, respectively.

The Fermi contact contribution corresponds to the probability of the unpaired electron being found at the nucleus, which in the case of alkali atoms Li($1s^2 2s^1$) and Na([Ne]$3s^1$) contains an indirect contribution of the inner-shell spin polarization. The computational consequences are, first of all, the need to use an UHF reference for polarization, and second, the all-electron correlation with no frozen orbitals imposed.

Calculation of the distance dependent $A_{\text{iso}}(R)$ curves, and especially modelling of the negative shift, required analytic spin density matrices which were available at most CCD or MP4(SDQ) correlated levels of theory. The results obtained are presented in Fig. 4.1, where the above mentioned two opposite effects are seen to prevail in different interaction regions. In addition to these, an abrupt turnover occurs at shorter internuclear distances leading rapidly to very large negative shift values, which is an indication of extensive shielding of the unpaired electron from the nuclei. More precisely, the situation can be described by a contribution of a molecular Rydberg state, which gains occupancy by the unpaired electron as the interatomic separation decreases.

The behaviour of the A_{iso} shift (ΔA_{iso}) can be seen to closely resemble the shape of relative interaction energies of the pair of atoms. This follows from the fact that the change of the unpaired electron density at the nucleus is directly proportional to the vdW interaction energy [16]. As observed from the Fig. 4.2, the minima of the ΔA_{iso} curves are located at slightly larger distances than the corresponding potential energy curve minima, but otherwise the interactions follow a similar trend.

The calculated Rg-X energies and experimental Rg-Rg energies were fitted to a single analytic potential energy function and used in the MD simulation. The MD code was modified to collect the ensemble averages for the hyperfine values, A_{iso} and its standard deviation, by including the computed curves that were pairwise summed either in fitted or linearly interpolated form.

The MD trajectories, carried out in a microcanonical (NVE) ensemble for 20–40 ps after a short thermalization period, yielded the hyperfine shift values ΔA_{iso} that were compared to the experiment. The results suggest that H atoms do trap only in substitutional sites in face centered cubic (fcc) Ne lattices, whereas in heavier rare gases both octahedral interstitial and substitutional trapping structures are thermally stable. The corresponding ΔA_{iso} values are in good agreement with the experimentally derived parameters, except for Xe where only a single trapping site has been observed. According to the simulations this can be assigned to a nearly undistorted substitutional site. The Xe matrix is rather peculiar, since detection of hydrogen atoms being photogenerated from precursor molecules has been very difficult by EPR [13], although the number density of trapped atoms is expected to be high. Moreover, the spectral analysis is complicated due to strong superhyperfine coupling caused by magnetic isotopes ^{129}Xe and ^{131}Xe. A possible explanation for the "magnetic transparency" of the H atoms trapped in tight octahedral positions may be connected to the turnover seen in the A_{iso} curves (Fig. 4.1). As a result of this acute distance

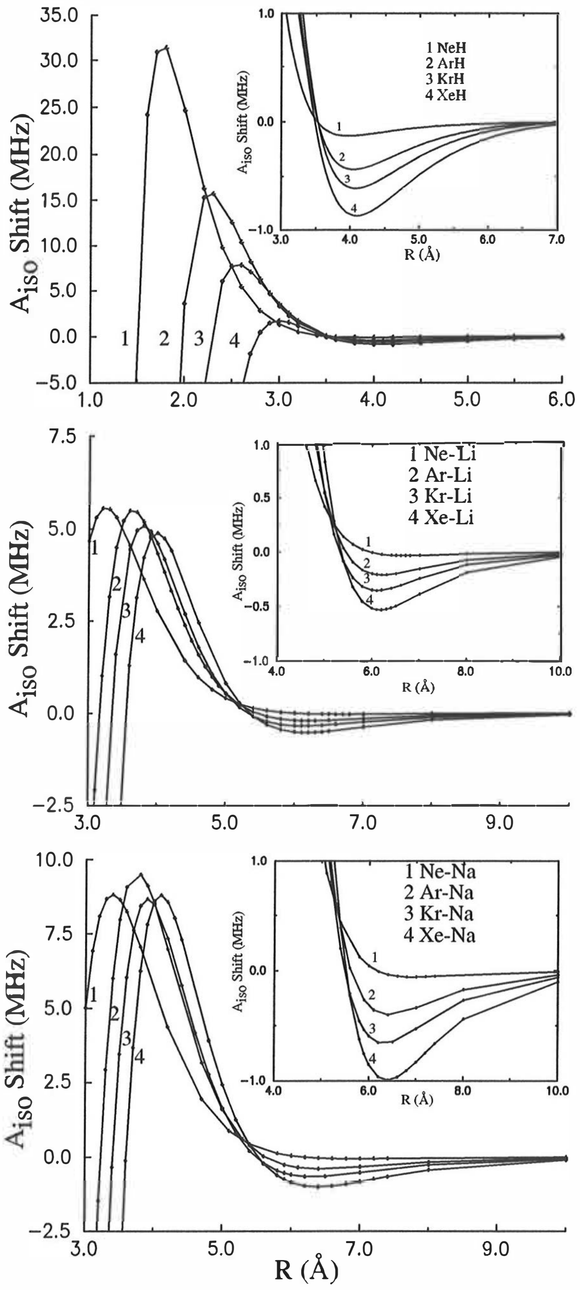

Figure 4.1: The distance dependence of the A_{iso} shifts of the impurity atom for diatomic pairs as obtained from MP4SDQ (Rg-H) and CCD (Rg-Li,Na) spin densities. The scaling to zero asymptote was obtained by the counterpoise procedure.

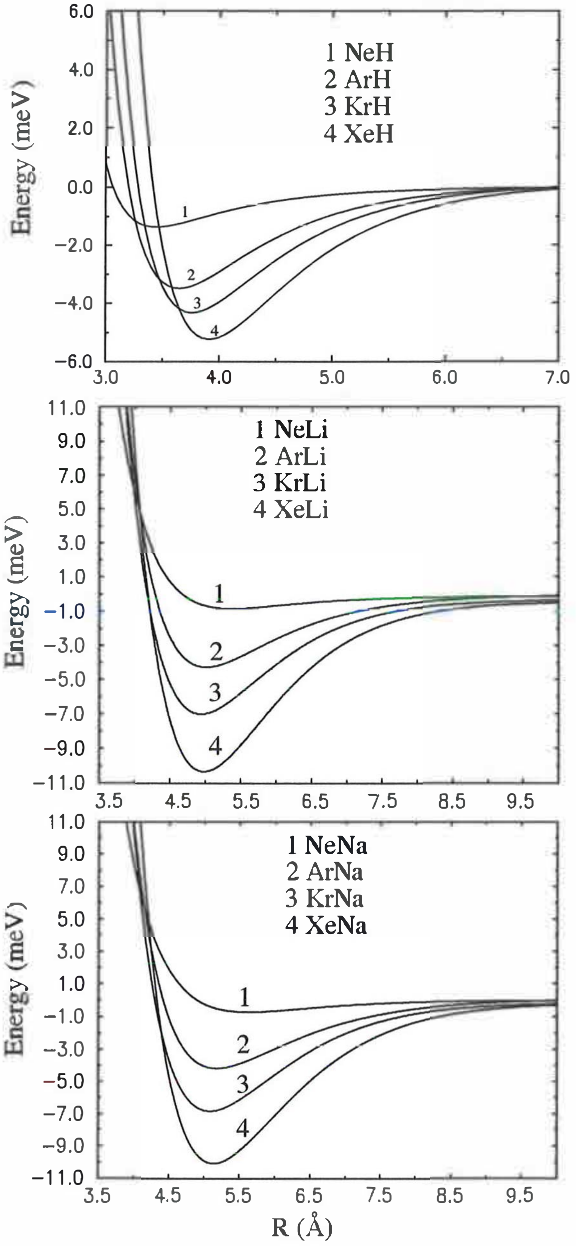

Figure 4.2: The CCSD(T) potential energy curves for Rg-(H,Li,Na) pairs, CP-corrected for BSSE.

dependence, the transitions might broaden severely, even beyond recognition. The above discussion is, however, only meaningful provided that the calculated ΔA_{iso} curves are qualitatively correct, i.e. that the pair-additivity assumption still holds.

The larger atomic radii of the alkali atoms cause a more dramatic relaxation of the surroundings than is found in H/Rg lattices, and it necessitates extended trapping sites for stabilization. Experimentally, it has been found that matrix preparation affects the trapping structures. In particular, thermal atom sources such as the Knudsen oven for alkali atoms mainly lead to multiple substitutional trapping as concluded on the basis of the negative ΔA_{iso} values, whereas atoms generated by laser ablation do trap in single substitutional sites. On the grounds of the simulations it is stated that more than six neighbouring vacancies are needed to reproduce the observed negative or small positive shifts. The large positive shifts, on the other hand, are unambiguously due to trapping in tight single substitutional sites. The octahedral site is not stable for trapping in Ne and Ar, but is stabilized in Kr and Xe. With the above cited preparation methods this is not, however, a probable trapping site. The numeric figures are more accurately reproduced for Li/Rg than Na/Rg, where the simulated values do not quite reproduce the large shifts. This discrepancy is most likely due to the limited accuracy of the calculated ΔA_{iso} curves.

Although the present method may be criticized for its neglect of the zero point motion, quantum corrections to the classical picture will not invalidate the conclusions obtained. The effect of the zero point motion can be compensated by increasing the temperature above the experimental level, as the enhanced motion accounts for the zero point amplitude. It can be seen in paper I that the temperature-enhanced motion (5–40 K) yields minor modifications to the numeric values but leaves the interpretation intact.

In addition to the above observations, further experiments have been conducted for H doped mixed Ne/H_2 matrices [83], showing novel trapping structures with negative hyperfine shifts. Preliminary simulations were performed with nearest-neighbour matrix atoms replaced by vacancies or spherical parahydrogen ($p\text{H}_2$) molecules [84]. The results are given in Table I. It is clearly seen that the negative shift is reproduced in a multiple substitutional trapping site, having at least four initially placed vacancies at nearest-neighbour positions. The lattice rearranges itself if further vacancies are issued, causing a fading of the effect. The original hypothesis of the experimentalists, that by adding more H_2 the negative shift would become more pronounced, is not supported by these simple simulations. This is also quite evident according to the calculated pair data (H_2-H vs Ne-H).

Table I: The modelling of the negative A_{iso} shift for H atom in Ne/H_2 matrices as obtained from 40 ps MD simulations[a] where different number of lattice vacancies and subsequent substitutions with $p$$H_2$ molecules were issued.

Vacancies		H_2 molecules	
#Vac	A Shift (MHz)	#Vac filled	A Shift (MHz)
00	5.98		
01	4.89	01	4.71
02	3.14	02	4.08
03	3.00	03	3.55
04	−1.61	04	3.38
05	−1.49	05	3.43
06	−1.46	06	3.68
07	−1.38	07	4.21
08	−1.28	08	4.94
09	−1.33	09	5.04
10	−1.04	10	4.96
11	−0.90	11	5.44
12	−0.87	12	5.91
Experimental[b]	−1.42 +5.70		

[a] The simulations with vacancies were performed with the MOLDY program and the H_2 case with a code written in the present study. Literature potential parameters [85–88] and QCISD/aug-pVQZ calculated A_{iso} curves were used.

[b] The temperatures were 1.5 K at deposition and 4.2 K at recording, and the matrix ratio H_2/Ne $\cong 10^{-4}$–10^{-5} [83].

4.2 Diatomic sulfur short-range trapping

The experimental background that stimulated the present investigation of recombination dynamics of S_2 in solid argon consists of two observations [19]. The photogenerated sulfur atoms show thermally activated luminescence at 10–15 K due to the $B''\ {}^3\Pi_u \rightarrow X\ {}^3\Sigma_g^-$ transition of the S_2 molecule. Second, while photoexcited at 456 nm, the S atoms were observed to undergo efficient recombination already at 7.5 K. The calculations in paper III were aimed at providing a rigorous microscopic description of both thermal and photoinduced recombination processes. In order to accomplish this task, accurate full-range potential energy curves for S_2 and ArS were calculated to define the force field to be used in the MD simulations. Transition moments and emission spectra were computed for the observable optical bands, and dynamics simulations were performed to account for the two distinct recombination mechanisms.

The calculated electronic states are presented in Fig. 4.3. The transition dipole moments for the states indicated were used for generating theoretical spectra. This was accomplished by first numerically solving the nuclear Schrödinger equation in these potentials and then evaluating the Franck-Condon integrals between the $v' = 0$ vibronic level and the ground state vibronic manifold. The Fermi Golden Rule formula [80] gives the transition probability as

$$W_{fi} = \frac{32}{3}\pi^3 c\,\alpha(5.29 \times 10^{-11})^2 \times 10^6\,\tilde{\nu}^3\,|\mathbf{R}|^2\,s^{-1}\,, \tag{4.1}$$

where the constants have their standard meanings, $\tilde{\nu}$ is the transition energy in cm^{-1}, and $|\mathbf{R}|$ is the vibronically averaged transition moment. The radiative lifetimes are obtained as

$$\tau = \left(\sum W_{fi}\right)^{-1}\,, \tag{4.2}$$

giving the values of 0.032 μs for the $B \to X$ and 6.25 μs for the $B'' \to X$. These numbers compare well with the experimental values discussed in paper III. The conclusion is that the states are calculated with sufficient accuracy to warrant their subsequent use in the MD simulations.

The thermally induced recombination was studied first by placing the two S atoms as nearest neighbours in the lattice. This led to immediate recombination even at 1 K simulation temperature. On the contrary, the configuration where the atoms were separated by a distance corresponding to one lattice constant was thermally stable, and no recombination was observed during the simulation. The simulation was, however, able to reproduce the thermal onset of the observed S+S glow curve when the reaction barrier was lowered by introducing vacancies in the four atom plane perpendicular to the reaction coordinate. By considering the different time scales of the experiment and simulation, it was concluded that a trapping configuration with one to three properly placed vacancies results in recombination upon annealing. Although the simulations were based on the ground state surfaces derived from the ArS($^3\Pi$) and S$_2$($^3\Sigma_g^-$) potentials, the radiative recombination is expected to proceed with similar dynamics via the B'' state, since all the states correlating to the ground state atoms behave congruously at large interatomic distances. The simulations with one excited S(^1D) atom showed less effective thermal recombination since the more strongly bound 1 $^1\Sigma^+$ state yielded stronger trapping according to radial distribution

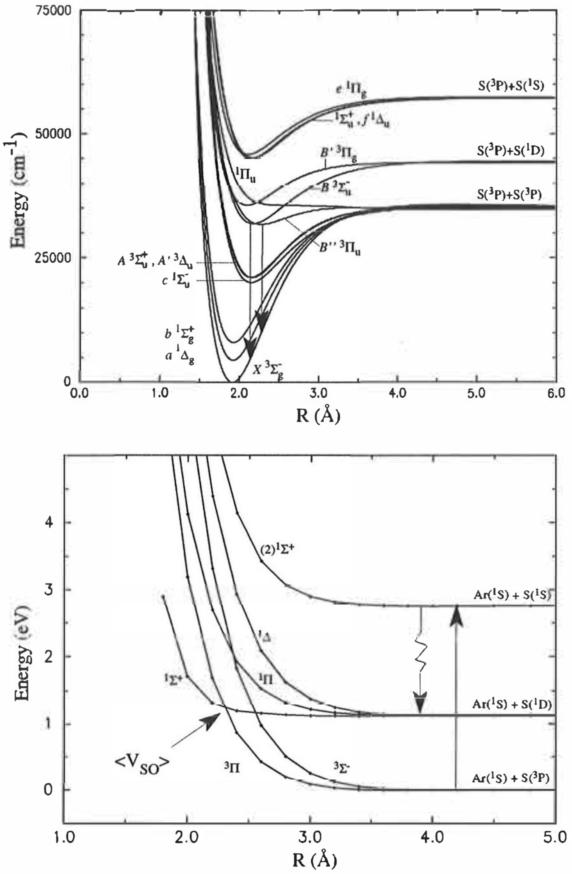

Figure 4.3: The electronic states of S_2 and ArS calculated by the internally contracted MRCI method utilizing CASSCF orbitals. In the upper panel the arrows indicate the relevant optical transitions that were also computed as a gas phase analogue to the bands observed at recombination. The photolytic process is sketched in the lower panel: The excitation at 456 nm (2.75 eV) is accompanied with atomic emission to the S(^1D) state, and the relaxation proceeds via $^1\Sigma^+$ state allowing for enhanced motion and spin-orbit mediated return to the ground state. The final step involves the 1.1 eV kinetic energy release which is observed as the $B'' \rightarrow X$ emission spectrum due to participation of phonons in the recombination process. This was simulated in terms of shock waves.

functions. However, the atomic excitation contributes indirectly to enhanced recombination as discussed below.

In order to unravel the mechanism behind the light induced S+S recombinant emission, two distinct approaches were tested. Local kinetic excitation of a lattice atom next to the trapped S atom pair was efficient in promoting recombination even in a perfect lattice, provided that the direction was properly chosen. The initial energy of this impulse (1.1 eV) was adjusted in accordance with the S(^1D)–S(^3P) energy separation, the amount released as phonon emission in collisional quenching when the $^3\Sigma^+/\,^3\Pi$ surfaces become populated at their repulsive walls (see Fig. 4.3). Quite obviously, introduction of lattice vacancies in a similar fashion to the thermal study further enhanced the recombination cross section. The shock waves arguably generated by the relaxation process were shown to propagate long distances in the lattice. For example, a shock wave carrying 2.0 eV initial energy was able to induce recombination through a chain of five argon atoms in the ⟨110⟩ crystallographic direction. However, the available energy of ca. 1.0 eV is sufficient only in a local process, hence long-range trapping does not contribute to the emissions.

The results of the simulation clearly support short-range trapping as a precursor configuration for the observed recombinant emissions. The experimental fact that a second glow appears at higher annealing temperatures can be ascribed to a trapping configuration with a minimal (1–2) number of vacancies. More extended mobility of distantly separated atoms seems a less probable cause for the additional luminescence. It is also experimentally observed that some of the S atoms remain unreacted at elevated temperatures.

The present study bears correspondence to the combined EPR and laser induced fluorescence (LIF) study of photolytically fragmented NO, where the short-range trapping to N$\cdots$Rg$\cdots$O like structures was shown to be responsible for the observed thermoluminescence [20]. While those assignments were made possible by the use of magnetic and optical spectroscopy, similar examination is not applicable for sulfur atoms due to their transparency in EPR measurement. Therefore, the theoretical treatment was required to raise the discussion of S_2 recombination dynamics to a quantitative level.

4.3 Atomic boron in axially symmetric sites

The work published in papers IV and V utilizes both magnetic (EPR) and optical (UV, LIF) spectroscopy, aided by theoretical investigation, in order to characterize trapping of boron atoms in rare gas solids. It is shown that magnetic and optical properties clearly offer a complementary pair of probes for investigating structures in solids. In addition to being useful in the structural analysis, the properties themselves are of interest for their rather peculiar behaviour. When embedded in solid argon, an EPR detectable boron atom (^2P) behaves like a $^2\Sigma^+$ state molecular radical species. In practice, this means that the orbital angular momentum is quenched and an EPR spectrum characteristic of an axial symmetric species is observed. This is clearly indicated by the appearance of the anisotropic hyperfine parameters $A_\perp$, $A_\parallel$ and g-tensor values $g_\perp$, $g_\parallel$ [18]. A particularly interesting phenomenon appeared as the matrix was changed from Ar to Kr, and further to Xe, in paper IV. This caused the g-shift ($\Delta g_\perp = g_\perp - g_e$) to change from negative to positive. The theoretical analysis revealed that the heavy-element effect, namely the Kr (and Xe) atom spin-orbit contribution, was responsible for the change of the sign. While severe matrix perturbation is seen in EPR, as the signals result from strong quenching, the optical transitions become at the same time heavily blueshifted from the gas phase position of the $2s^2 3s\,(^2S) \leftarrow 2s^2 2p\,(^2P)$ absorption. The extent of the observed blueshifts together with the occurrence of several distinct bands has confused the assignments [89, 90], and only very recently some clarity has been attained [4]. The renewed discussion gave the core-to-valence $2s2p^2\,(^2D) \leftarrow 2s^2 2p\,(^2P)$ transition as a partial explanation apart from the different trapping site effects suggested earlier. The present simulations predict less pronounced blueshifts than previously claimed for the $3s \leftarrow 2p$ absorption, and the new measurements revealed novel absorption bands consistent with the theory.

In this section the theoretical methods, namely the quantum chemical computation of diatomic information, the DIM-MD simulation for the description of the full system, and the ideas for generating the magnetic and optical spectra, are presented and the main results are discussed.

The many-body problem was approached by calculating pairwise *ab initio* data for all the interactions. First of all, the potential energy curves for the Rg(^1S)-Rg(^1S) pairs were obtained with CCSD(T) theory. The set of B(^2P)-Rg(^1S) states $\{^2\Sigma^+, {}^2\Pi_{x,y}\}$ or LS-coupled $\{^2\Sigma_{1/2}, {}^2\Pi_{3/2,1/2}\}$ were calculated by RHF-UCCSD(T) or MRCI+Q, respectively, using the MOLPRO code [62]. The excited $B\,^2\Sigma^+$ state of B(^2S)-Rg relevant to the optically accessed surface was produced by MRCI+Q as well. The spin-orbit (H_{SO}) and orbital-Zeeman (H_{OZ}) transition matrix elements of Eq. (2.25) for g-tensor evaluation were computed with unperturbed MRCI+Q wavefunctions. The spin-orbit part was fragmented into valence and core contributions and calculated separately [91]. The description of the energy separation in Eq. (2.25), that is, the $p_z - p_{x,y}$ orbital energy difference, or in other words, the crystal field effect breaking the orbital degeneracy, involves the DIM simulations demonstrated below. The hyperfine structure, $\mathbf{A}(R)$, for the $^2\Sigma^+$ and $^2\Pi$ states was computed with UHF-QCISD wavefunctions in the framework of GAUSSIAN package [63]. The correlation-consistent basis sets of Dunning and co-workers were used for B, whereas the RECPs of the Stuttgart group were utilized for Rg.

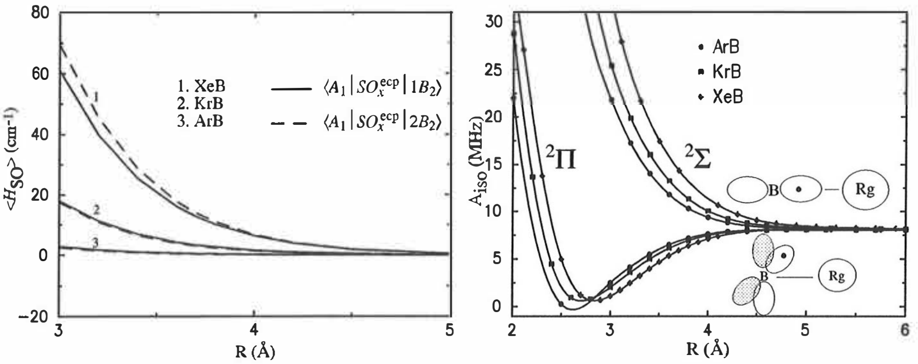

Figure 4.4: Left: The core contribution to spin-orbit matrix elements for B-Rg pairs as labeled by the state symmetries, A_1 for the ($\Lambda = 0$) ground state and B_2 for the lowest ($\Lambda = 1$) excited states. This is to be compared with the constant valence matrix element value of -5 cm^{-1}. Right: The state-specific distance dependence for isotropic Fermi contact coupling. The behaviour of the spin-dipolar term is somewhat similar.

It was observed in the quantum chemical computations that the valence (Breit-Pauli) spin-orbit matrix elements stay practically independent of the interatomic B-Rg distance. The core (RECP) contribution, however, begins to appear as the overlap increases (Fig. 4.4). This term is of opposite sign as compared to the valence contribution, and starts to dominate the atomic B value at short distances, especially with the heavier Kr and Xe. This ultimately explains the observed flip in the g-shift when the actual environment with many perturbers is considered. The behaviour of the hyperfine interaction is a result of the change of the spin density near the nucleus, and is observed to somewhat resemble the behaviour of the electronic energies in a fashion similar to the isotropic alkali metal and H atom cases. In the $^2\Sigma$ state the increasing orbital overlap introduces more s-wave nature into the wavefunction, mainly due to the spin-polarization effect. In the $^2\Pi$ state the perpendicular perturbation first reduces the spin density (Fig. 4.4).

Using the pair potentials as input, the adiabatic potential energy surfaces were constructed via minimal basis $\{p_x, p_y, p_z\}$ DIM scheme [92]

$$\begin{aligned} H_{\text{DIM}} &= \sum_{i<j} V(\text{Rg}_i, \text{Rg}_j) \otimes \mathbf{1} \\ &+ \sum_i \begin{pmatrix} V_i(^2\Pi) + x_i^2\Delta_i & x_i y_i \Delta_i & x_i z_i \Delta_i \\ x_i y_i \Delta_i & V_i(^2\Pi) + y_i^2\Delta_i & y_i z_i \Delta_i \\ x_i z_i \Delta_i & y_i z_i \Delta_i & V_i(^2\Pi) + z_i^2\Delta_i \end{pmatrix}, \end{aligned} \tag{4.3}$$

where $\Delta_i = V_i(^2\Sigma) - V_i(^2\Pi)$ and x_i, y_i, z_i denote the direction cosines of the lines joining the ^2P atom and ^1S atoms relative to the laboratory frame. Diagonalization of the interaction matrix yields the crystal field effect that is used as ΔE_{0n} in Eq. (2.25) for estimating the g-shift. The classical (velocity Verlet) simulation that used the DIM construct for the evaluation of forces consisted of a B doped 256 atom fcc lattice with periodic boundaries. In order to stabilize the initial lattice structures, the system was subject to simulated annealing and velocity-scaled thermalization prior to collecting the microcanonical ensemble averages. The three components of the **A** matrix, diagonal in the p-orbital frame, were collected at every tenth simulation step by using the DIM eigenvectors Γ_k to define the directional contributions as follows:

$$A_j = \sum_{i=1}^{n} \sum_{k=1}^{3} (d_i \cdot \Gamma_k)^2 \, a^{k,j}(r_i), \;\; j = 1, 2, 3 \tag{4.4}$$

where d_i is the direction cosine and $a^{k,j}$ contains the distance dependent FC and SD hyperfine (shifts from free atom) data. After summing over all the nearby lattice atoms i, the free atom $A_{\perp,\parallel}$ and A_{iso} values were added to this array. Next, the matrix **A** having the above array values in the diagonal was transformed into the fixed reference frame of laboratory where the averaging over the simulation period was performed. The same DIM formalism was exploited in the optical study. The lowest eigenenergy gives directly the magnitude of the ground state solvation for the lattice embedded B atom. The excited $B\ ^2\Sigma^+$ state, on the other hand, is isotropic and the interaction with the lattice atoms is a simple pairwise sum over the nearest ones. Therefore, the $3s \leftarrow 2p$ absorption was represented by recording the energy difference between the lowest energy eigenvalue and the potential energy evaluated at the excited $B\ ^2\Sigma^+$ state, and adding the free atom 249.75 nm offset. The spectrum was obtained simply from the histogram of these data and, since there is no operator involved in the treatment, it is not a property in the usual sense. The spectral width is thus purely a result of thermally driven configurational sampling of the Franck-Condon region in the trapping cage, with an assumption of a constant transition dipole.

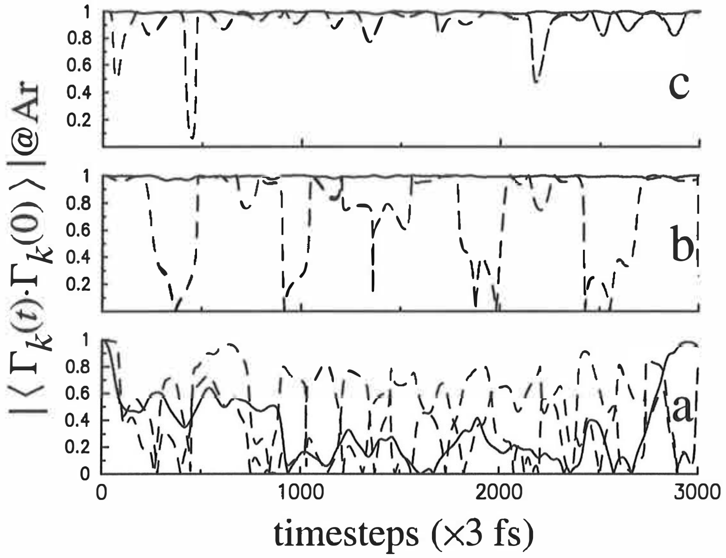

Figure 4.5: The boron $2p$-orbital time correlation functions for a substitutional site in Ar host. a) No vacancies, b) one vacancy, c) two vacancies in the unit shell issued. The solid line corresponds to the eigenvector of lowest energy and dashed lines stand for the xy-frame.

The DIM procedure lifts the degeneracy of the p orbitals, and depending on the relaxed lattice structure, different energetics is obtained. The axial symmetry, which is required for a B atom to be detected by EPR and for the concept of orbital angular momentum quenching, is in practice equivalent to orbital locking in some preferable direction. A convenient means to characterize this matter is offered by the orbital autocorrelation function, which in the present case can be defined in terms of DIM eigenvectors as

$$\mathcal{C}_k = \langle\, \Gamma_k(t) \cdot \Gamma_k(0)\, \rangle\,. \tag{4.5}$$

The result of the simulations was, as expected, that an axially symmetric lattice environment was required to produce the parameters $A_{\perp,\|}$ and $\Delta E_{zx} \approx \Delta E_{zy}$ showing axial (cylindrical) character. As an example of the time behaviour of the p-orbital orientation, the correlation functions for Ar lattice are presented in Fig. 4.5. Without vacancies, the orbital frame is seen to rotate freely and lose its memory of the initial orientation in a picosecond time scale. However, if a single nearest-neighbour vacancy is introduced, one of the eigenvectors (z) becomes locked and the others (x,y-frame) rotate. Furthermore, an additional vacancy yields a configuration where the whole frame is nearly fixed. Similar behaviour was observed also for the other two Rg's. The straightforward assignment for the magnetically detected B atoms then corresponds to trapping in single or two-vacancy environments. It should be noted here that an interstitial (O_h) initial position in an otherwise perfect lattice also produced strictly locked orbital orientation in Kr and Xe. However, this situation is not favored by energetics since only the lowest eigenstate is bound. The orbital locking is connected to the optical transitions in the sense that the axially symmetric case corresponds predominantly to a $^2\Sigma(\Lambda = 0)$ type ground state which is subject to certain dipole selection rules for allowed excitations.

Table II: Theoretical data involving substitutional trapping of the impurity B with a single lattice vacancy issued nearby. The DIM simulated energetics (E_n, ΔE) and hyperfine tensor ($A = A_{\mathrm{iso}}\mathbf{1} + \mathbf{A}_{\mathrm{dip}}$) values along with the 2nd order contributions to the g-tensor are presented. The orbital-Zeeman (L_x) $\simeq$ 1 a.u. and is gauge invariant.

E_n [meV]	$\Delta E_{z-x,y}$ [meV]	A [MHz]		SO_x [cm^{-1}]^{a}	SO_x^{recp} [cm^{-1}]^{a}		$\Delta g_\perp$ [ppm]
Ar							
−161.3	−77.1	‖	119.7	−4.91	0.64	540	−31 410
−104.0	−57.3	⊥	−47.5				
−84.2		⊥'	−46.7				
Kr							
−198.1	−48.5	‖	116.2	−4.91	2.63	340	−26 580
−163.4	−34.7	⊥	-42.4				
−149.6		⊥'	-37.7				
Xe							
−200.7	−110.4	‖	117.7	−4.91	10.2	680	30 500
−143.1	−57.6	⊥	−46.8				
−90.2		⊥'	−43.6				

[a] The Rg-B distances correspond to the estimated equilibrium values taken from DIM radial distribution functions (RDF): 3.6 Å for Ar, 3.9 Å for Kr, and 3.8 Å for Xe.

The DIM simulated magnetic parameters show rather similar hyperfine structure for B in all the Rg hosts. The heavy-element effect, however, contributes to the g-shift and inverts the whole spectrum as shown below. A representative collection of the simulation results is shown in Table II. Although the g-shift appears negative for a single B-Kr pair, it should be noted that already with two pairwise contributing Rg perturbers the sign changes as the SO_x^{recp} labeled term starts to dominate. The parameters illustrated above were used in the numerical EPR spectrum simulation program XEMR [93], with the implementation of the following effective Hamiltonian in the $|m_l \, m_s \, m_I\rangle$ basis

$$H_{\mathrm{eff}} = \mu_B \boldsymbol{B}(g_e \boldsymbol{S} + \boldsymbol{L}) + \zeta \boldsymbol{L} \cdot \boldsymbol{S} + \mu_N \boldsymbol{B} g_I \boldsymbol{I} + \boldsymbol{S} \cdot \mathbf{A} \cdot \boldsymbol{I} + H_{ttgl}(L) \,, \qquad (4.6)$$

where the orbital contributions are explicit (instead of usual spin Hamiltonian form $\mu_B \boldsymbol{B} \cdot \mathbf{g} \cdot \boldsymbol{S}$), ζ is the atomic spin-orbit coupling constant which was adjusted according to the above theoretical prediction, and the other symbols have their standard meaning. The crystal fields are defined by H_{ttgl} which in the case of tetragonal distortion has a reduced operator representation of the form [94]

$$H_{ttgl,d} = \alpha_t [3L_d^2 - \boldsymbol{L}(\boldsymbol{L}+1)\mathbf{1}] \,, \quad d = x, y, z \qquad (4.7)$$

where α_t is the distortion parameter and the following relations prevail: $3\alpha_{t,x} = \Delta E_{zx}$, $3\alpha_{t,y} = \Delta E_{zy}$, $\alpha_{t,z} = 0$. After solving the magnetic field values for resonance condition, the single crystal spectra were lineshape convoluted and integrated over the spherical angles to yield the synthetic powder spectra. Finally, the fitting to the experimental spectrum was performed with Monte Carlo or simplex based methods.

The outcome of the measurements and simulations is shown in Figs. 4.6 and 4.7 for Ar and Kr solids, respectively. In the fitting procedure $A_{||}$ was first adjusted to match the accurate experimental value, the averaged crystal field parameter was taken from DIM simulations, and the spin-orbit parameter ζ was varied accordingly. The presented numerical values, as a result of combination of experiment and theory, provide enhanced accuracy for the parameters obtained in Ar host and new results are given for Kr. The linewidths for parallel and perpendicular transitions, $\mathrm{LW}_{||} : \mathrm{LW}_{\perp} = 1 : 7$ in Ar, imply the spin-orbit mediated modulation of the spin-lattice relaxation in the xy-plane which broadens the $A_{\perp}$ transitions. The tentative assignment provided for the Xe matrix case is based on the results presented in Fig. 4.8, where the measured and synthetic spectra are shown along with the parameters. Finally, it is noted that the observed traces at 12 K in Ar and Kr hosts were effectively bleached at 16 K, whereas in Xe the disappearance of the atomic resonance was notably initiated

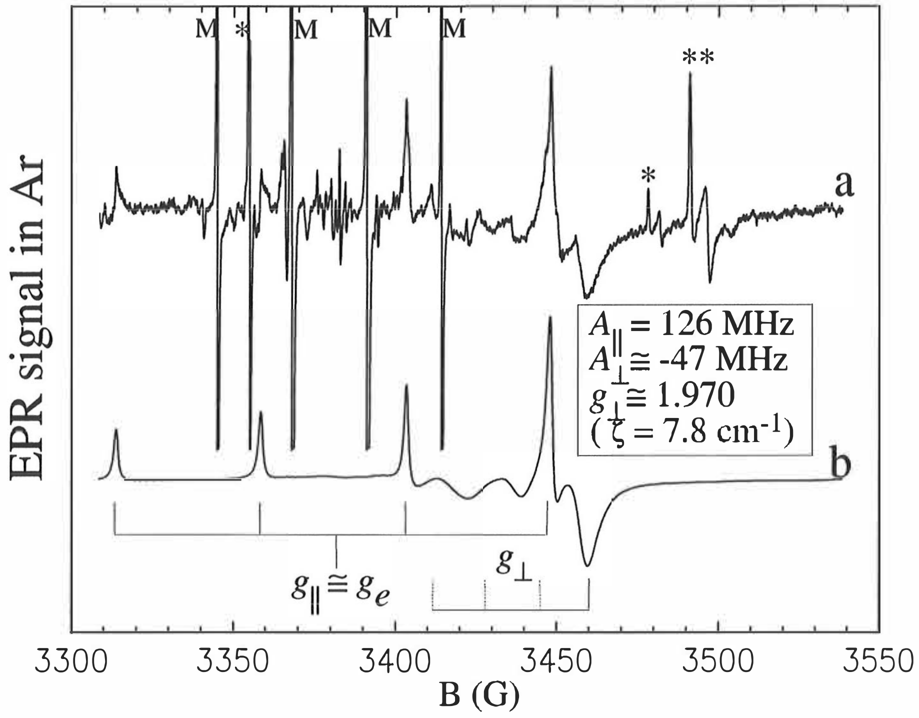

Figure 4.6: The EPR spectra of ^{11}B atoms in solid Ar: a) Experimental, b) simulated and fitted with axially symmetric theoretical parameters. Methyl radical impurity quartet is designated by M, and lines due to ^{11}BO (*) and ^{10}BO (**) are also marked. The difficulty lies in the broadened $A_{\perp}$ transitions that are not resolved in the spectra. (10 G = 1 mT = g/g_e 28.025 MHz)

at 35 K, accompanied with simultaneous appearance of signals due to the H_2BO molecule.

The simulation of the optical $3s \leftarrow 2p$ excitation was able to produce transition energies severely blueshifted, however, to a lesser extent than previously reported (e.g. 7000–8000 cm^{-1} in Ar) [89,90]. An expected outcome was the dependence on the vacancies, that is, a smaller blueshift for larger trapping sites. Although the results are very sensitive to the pair potentials used, the conclusion that these transitions cannot be blueshifted substantially more than the simulations predicted, was confirmed. Utilizing the knowledge obtained by magnetic resonance, i.e. that trapping occurs in an axially symmetric environment, the simulations yielded transition maxima at 236.5, 243.5, and 244 nm in Ar, Kr, and Xe, respectively. Because of these observations, new ex-

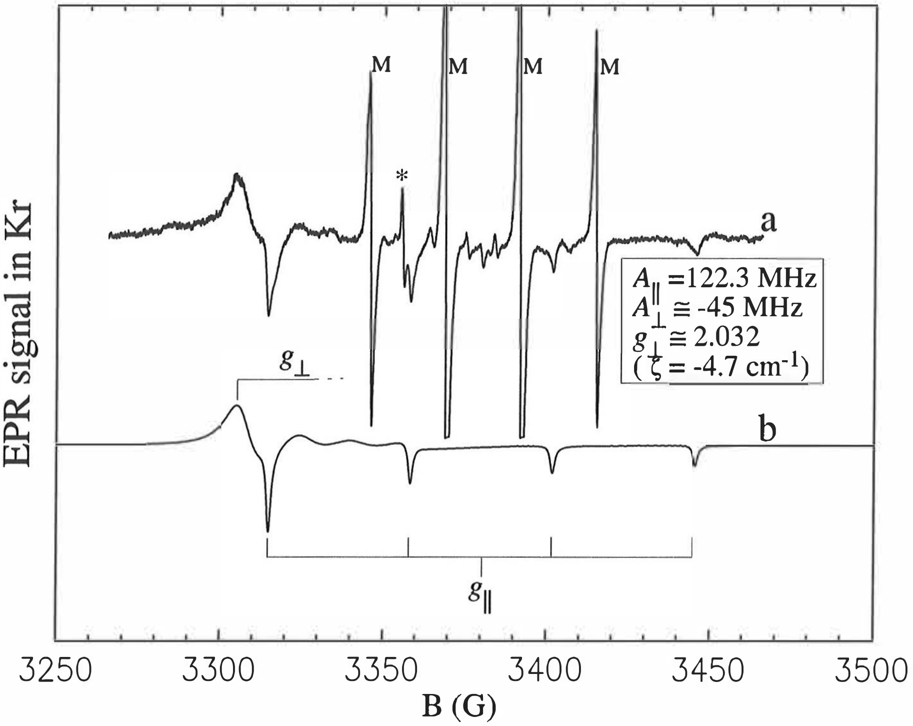

Figure 4.7: The experimental (a) and simulated (b) EPR spectra of ^{11}B atoms in solid Kr. Compared to the Ar case, the heavy-element effect is seen in that the spectrum is reversed, that is, $g_{\perp} > g_{\|}$ and the phase of the parallel transitions is turned around. This was simulated by changing the sign of the variable ζ.

periments were conducted to ascertain the theoretical prediction. The optical absorption measurements in the ultraviolet region, indeed, revealed bands in the expected range, showing a temperature dependence highly similar to that found for the atoms detected by EPR. Furthermore, the decrease of the signal intensity upon annealing was seen to correlate with the corresponding rise of a molecular species, the Σ-Σ band of B_2, formed by thermally mobilized atoms. The bands observed earlier, i.e., those on the high energy side of these novel transient atomic absorptions, were also reproduced here, and proved stable within the temperature range of the experiment. The measured laser induced fluorescence spectra provide complementary proof that the novel absorptions at 241–254 nm are caused by the $3s \leftarrow 2p$ transitions. The observed reduction of emission intensities at elevated temperatures means that the emitting species can be assigned to the same one responsible for the observed transient absorp-

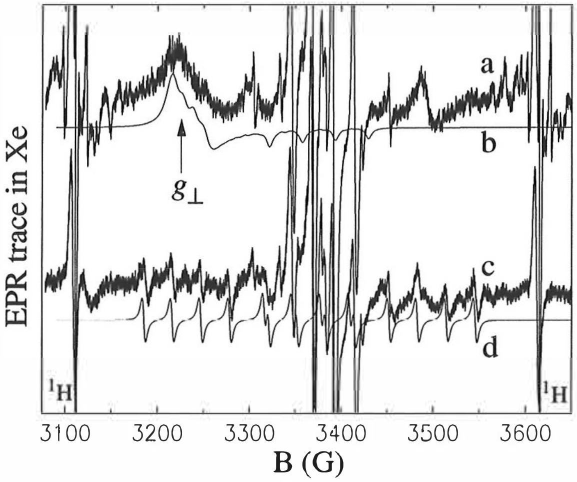

Figure 4.8: The EPR spectra of B in Xe matrix: a) Experimental at 12 K, b) simulated with parameters derived from theory, c) experimental at 50 K, d) the simulated spectrum of thermally formed $H_2{}^{11}BO$ ($g = 2.0075$, $A(H) = 375.8$ MHz, $A(B) = 87.6$ MHz). The broad feature at 3200 G is tentatively assigned to $g_{\perp}$ transition of boron. The simulation parameters were taken from the two-vacancy case: Averaged crystal field $\Delta E = 252$ cm^{-1}, nonaxial $A_{\|} = 101$ MHz, $A_{\perp} = 36.6$ MHz, $A'_{\perp} = 26.2$ MHz, and effective $\zeta = -11.4$ cm^{-1}.

tions. The features of the emission signals can be qualitatively explained with the aid of *ab initio* calculated pair potentials. Namely, the two distinct bands in Ar are due to a transition from the deeply bound inner part of the excited state potential (broad) and a transition from the vdW region (narrow). In other hosts, no barrier is formed between the vdW and inner regions and consequently only the broad band from the relaxed excited state appears.

The results concerning the optical studies are collected in Table III. The main observation was that the orbitally quenched atoms are trapped in quasi stable sites. These atoms are visible in the EPR, and have dipole allowed $3s \leftarrow 2p$ optical transition. The origin for the strong and stable (also designated as thermal in Xe) absorption bands was associated with trapping in sites not observable in EPR. Such a symmetry is, for example, present in the substitutional site, where the orbital frame is free to rotate and no preferable quantization axis is formed. The extent of blueshift would, however, definitely necessitate a too large value for the solvation per Rg atom based on the knowledge gained from pair potentials. For such a nonquenched atom the core-to-valence $2p \leftarrow 2s$ transition is

Table III: UV absorptions and LIF emissions in B doped Ar, Kr, and Xe matrices. Estimated accuracy of the last digit is given in parentheses. The simulated numbers correspond to the $3s \leftarrow 2p$ transition matrix-shifted from the gas phase value of 249.75 nm.

	Absorption		LIF	
Rg host	Type	λ (nm)	Type	λ (nm)
	stable	210.4(1)		
	stable	215.6(1)	broad	285(5)
Ar	transient	241(2)	narrow	254.2(3)
	simulated	236.5		
	B_2 (0,0)	331(1)		
	stable	210.7(2)		
	stable	226.7(3)		
Kr	transient	247(1)	broad	297(2)
	simulated	243.5		
	B_2 (1,0)	325(1)		
	B_2 (0,0)	335(1)		
	stable	213.7(1)		
	thermal	220.0(2)		
	thermal	231.5(1)		
Xe	transient	254(1)	broad	337(3)
	simulated	244		
	B_2 (1,0)	332(1)	$Xe_2^+H^-$	257(2)
	B_2 (0,0)	343(1)		

probably the origin for the observed lines in the 210–230 nm range, although this was not validated by any simulations.

Chapter 5

Summary

In this thesis theoretical methods have been used to interpret the spectroscopy of some atoms and molecules isolated in rare gas solids. The adopted computational approach combines quantum chemical and classical methods. The modeled systems, namely, large periodic rare gas lattices doped with atomic impurities, have thus been divided into quantum mechanically described diatomic fragments of which the whole system has been constructed by pairwise or DIM based summation. The dynamics of the constituent atoms, on the other hand, has been described by classical equations of motion. For the diatomics, *ab initio* electronic structure calculations exploiting e.g. the state of the art Coupled Cluster and MRCI formalisms have been performed in order to find the necessary parameters with the required accuracy. The finite-temperature MD simulations were based on forces dictated by potential energy surfaces of the calculated quantum chemical origin. The simulations have been carried out to obtain the time-averaged properties perturbed by the matrix environment. The emphasis has been put on magnetic interactions important for the EPR spectroscopy. The studies have covered the simple isotropic ^2S state cases of hydrogen and alkali metal atoms, and the more challenging anisotropic ^2P case of boron. Optical spectroscopy of the matrix isolated B atom has also been examined, and the emission bands due to recombination dynamics of sulfur atoms have been calculated. As a conclusion, in most cases the agreement of the theoretical results with the available experimental ones is good and the assignments are reliable in spite of the shortcuts introduced into the theoretical description.

One of the main topics of the present study is the spin density of the paramagnetic impurity atom. The geometry of the surrounding matrix has a perturbative effect on the spin distribution, in terms of the Pauli repulsion and vdW attraction forces, thus providing a straightforward relation between the hyperfine parameters and trapping site structures. The quantum chemical calculation of the interatomic distance dependence of the parameters and the subsequent dynamical averaging, performed in publications I, II, and IV, was able to confirm the experimental assignments and provide theoretical insights into the atomic dynamics. Moreover, the directional nature of interactions of the ^2P state impurity atom B is exploited in full detail in publication IV to characterize the novel EPR signals, and renewed interpretation is offered for the heavy-element effect on the spectra. It is also shown in publications IV and V that the optical and magnetic spectroscopies offer complementary means for the characterization of spectroscopy and chemical dynamics, along with the result that theoretical investigation with the present method produces enhanced accuracy for the microscopic interpretation and spectral parameters.

The simulation of recombination dynamics of a photolytically prepared pair of S atoms, separated in a metastable configuration, is carried out in publication III. The MD study explores substitutional trapping structures with vacancies that lower the barrier that prevents instantaneous recombination, and reproduces the experimental thermal behaviour along with the suggestion about the corresponding short-range trapping character. Two models are used for the light induced recombination, i.e. local kinetic energy excitation and artificial shock wave generation, which provide an explanation for the mechanism of phonon emission in the process.

Bibliography

[1] V. A. Apkarian and N. Schwentner, Chem. Rev. **99**, 1481 (1999).

[2] G. C. Pimentel, in *Formation and Trapping of Free Radicals*, edited by A. M. Bass and H. P. Broida (Academic, New York, 1960), Chap. Radical Formation and Trapping in the Solid Phase.

[3] B. Palaszewski, L. S. Ianovski, and P. Carrick, J. Propul. Power **14**, 641 (1998).

[4] S. Tam, M. Macler, M. E. DeRose, and M. E. Fajardo, J. Chem. Phys. **113**, 9067 (2000).

[5] J. R. Krumrine, S. Jang, M. H. Alexander, and G. A. Voth, J. Chem. Phys. **113**, 9079 (2000).

[6] *Rare Gas Solids*, edited by M. L. Klein and J. A. Venables (Academic, London, 1976).

[7] *Physics of Cryocrystals*, edited by V. G. Manzhelii and Y. A. Freiman (AIP, Woodbury, 1997).

[8] M. Pettersson, L. Khriachtchev, J. Lundell, and M. Räsänen, J. Am. Chem. Soc. **121**, 11904 (1999).

[9] L. Khriachtchev, M. Pettersson, N. Runeberg, J. Lundell, and M. Räsänen, Nature **406**, 874 (2000).

[10] P. Pyykkö, Science **290**, 64 (2000).

[11] R. Baumfalk, N. H. Nahler, and U. Buck, J. Chem. Phys. **114**, 4755 (2001).

[12] K. Vaskonen, J. Eloranta, T. Kiljunen, and H. Kunttu, J. Chem. Phys. **110**, 2122 (1999).

[13] J. Eloranta, K. Vaskonen, and H. Kunttu, J. Chem. Phys. **110**, 7917 (1999).

[14] K. Vaskonen, J. Eloranta, and H. Kunttu, Chem. Phys. Lett. **310**, 245 (1999).

[15] S. N. Foner, E. L. Cochran, V. A. Bowers, and C. K. Jen, J. Chem. Phys. **32**, 963 (1960).

[16] F. J. Adrian, J. Chem. Phys. **32**, 972 (1960).

[17] J. R. Morton, K. F. Preston, S. J. Strach, F. J. Adrian, and A. N. Jette, J. Chem. Phys. **70**, 2889 (1978).

[18] W. Weltner Jr., *Magnetic Atoms and Molecules* (Dover, New York, 1983).

[19] L. Khriachtchev, M. Pettersson, S. Pehkonen, E. Isoniemi, and M. Räsänen, J. Chem. Phys. **111**, 1650 (1999).

[20] J. Eloranta, K. Vaskonen, H. Häkkänen, T. Kiljunen, and H. Kunttu, J. Chem. Phys. **109**, 7784 (1998).

[21] C. W. Bauschlicher, S. R. Langhoff, and P. R. Taylor, Adv. Chem. Phys. **77**, 103 (1990).

[22] K. L. Bak, J. Gauss, P. Jørgensen, J. Olsen, and T. Helgaker, J. Chem. Phys. **114**, 6548 (2001).

[23] P. R. Taylor, in *European Summerschool in Quantum Chemistry III*, edited by B. O. Roos and P.-O. Widmark (University of Lund, Sweden, 1999), Chap. Accurate Calculations and Calibration.

[24] T. Helgaker, P. Jørgensen, and J. Olsen, *Molecular Electronic-Structure Theory* (Wiley, Chichester, 2000).

[25] P. W. Atkins and R. S. Friedman, *Molecular Quantum Mechanics*, 3rd ed. (Oxford University Press, Oxford, 1997).

[26] F. Jensen, *Introduction to Computational Chemistry* (Wiley, Chichester, 1999).

[27] A. Szabo and N. S. Ostlund, *Modern Quantum Chemistry*, first, revised ed. (Dover, New York, 1996).

[28] J. Olsen, O. Christiansen, H. Koch, and P. Jørgensen, J. Chem. Phys. **105**, 5082 (1996).

[29] R. J. Bartlett and G. D. Purvis, Int. J. Quantum Chem. **14**, 561 (1978).

[30] J. A. Pople, J. S. Binkley, and R. Seeger, Int. J. Quantum Chem. Symp. **10**, 1 (1976).

[31] B. O. Roos, in *European Summerschool in Quantum Chemistry II*, edited by B. O. Roos and P.-O. Widmark (University of Lund, Sweden, 1999), Chap. Multiconfigurational (MC) Self-Consistent (SCF) Theory.

[32] J. F. Stanton and R. J. Bartlett, J. Chem. Phys. **98**, 7029 (1993).

[33] B. Liu and A. D. McLean, J. Chem. Phys. **59**, 4557 (1973).

[34] S. F. Boys and F. Bernardi, Mol. Phys. **19**, 553 (1970).

[35] D. Sundholm, J. Chem. Phys. **102**, 4895 (1995).

[36] V. A. Rassolov and D. M. Chipman, J. Chem. Phys. **103**, 10058 (1995).

[37] J. Čížek, J. Chem. Phys. **45**, 4256 (1966).

[38] T. Crawford and H. Schaefer, in *Reviews in Computational Chemistry*, edited by K. B. Lipkowitz and D. B. Boyd (Wiley-VCH, Weinheim, 2000), Vol. 14, Chap. An Introduction to Coupled Cluster Theory for Computational Chemists.

[39] R. J. Bartlett, I. Shavitt, and G. D. Purvis III, J. Chem. Phys. **71**, 281 (1979).

[40] J. Noga and R. J. Bartlett, J. Chem. Phys. **86**, 7041 (1987).

[41] J. F. Stanton, Chem. Phys. Lett. **281**, 130 (1997).

[42] R. J. Buenker and S. D. Peyerimhoff, Theor. Chim. Acta **35**, 33 (1974).

[43] P. E. M. Siegbahn, Int. J. Quantum Chem. **18**, 1229 (1980).

[44] P. J. Knowles, M. Schütz, and H.-J. Werner, in *Modern Methods and Algorithms of Quantum Chemistry*, edited by J. Grotendorst (NIC, Jülich, 2000), Chap. Ab initio methods for electron correlation in molecules.

[45] H.-J. Werner and E.-A. Reinsch, J. Chem. Phys. **76**, 3144 (1982).

[46] H.-J. Werner and P. J. Knowles, J. Chem. Phys. **89**, 5803 (1988).

[47] S. R. Langhoff and E. R. Davidson, Int. J. Quantum Chem. **8**, 61 (1974).

[48] M. R. A. Blomberg and P. E. M. Siegbahn, J. Chem. Phys. **78**, 5682 (1983).

[49] J. A. Pople, M. Head-Gordon, and K. Raghavachari, J. Chem. Phys. **87**, 5968 (1987).

[50] T. H. Dunning, Jr., J. Chem. Phys. **90**, 1007 (1989).

[51] D. E. Woon, K. A. Peterson, and T. H. Dunning, Jr., J. Chem. Phys. **109**, 2233 (1998).

[52] A. Nicklass, M. Dolg, H. Stoll, and H. Preuss, J. Chem. Phys. **102**, 8942 (1995).

[53] R. E. Moss, *Advanced Molecular Quantum Mechanics* (Chapman and Hall, London, 1973).

[54] J. E. Harriman, *Theoretical Foundations of Electron Spin Resonance* (Academic, New York, 1978).

[55] W. Kutzelnigg, Theor. Chim. Acta **73**, 173 (1988).

[56] W. Kutzelnigg, Z. Phys. D **11**, 15 (1989).

[57] J.-M. Lévy-Leblond, Commun. Math. Phys. **6**, 286 (1967).

[58] R. McWeeny, *Spins in Chemistry* (Academic, New York, 1970).

[59] R. McWeeny, J. Chem. Phys. **42**, 1717 (1965).

[60] J. Olsen and P. Jørgensen, J. Chem. Phys. **82**, 3235 (1985).

[61] O. Vahtras, B. Minaev, and H. Ågren, Chem. Phys. Lett. **281**, 186 (1997).

[62] MOLPRO is a package of *ab initio* programs written by H.-J. Werner and P. J. Knowles, with contributions from R. D. Amos et al.

[63] GAUSSIAN 98, M. J. Frisch et al., Gaussian Inc., Pittsburgh PA, 1998.

[64] J. F. Stanton, J. Chem. Phys. **101**, 371 (1994).

[65] G. H. Lushington, P. Bündgen, and F. Grein, Int. J. Quantum Chem. **55**, 377 (1995).

[66] R. Car and M. Parrinello, Phys. Rev. Lett. **55**, 2471 (1985).

[67] R. N. Barnett and U. Landman, Phys. Rev. B **48**, 2081 (1993).

[68] E. J. Meijer and M. Sprik, J. Chem. Phys. **105**, 8684 (1996).

[69] F. O. Ellison, J. Am. Chem. Soc. **85**, 3540 (1963).

[70] J. C. Tully, J. Chem. Phys. **58**, 1396 (1973).

[71] I. H. Gersonde and H. Gabriel, J. Chem. Phys. **98**, 2094 (1993).

[72] B. L. Grigorenko, A. V. Nemukhin, and V. A. Apkarian, Chem. Phys. **219**, 161 (1997).

[73] B. L. Grigorenko, A. V. Nemukhin, A. A. Buchachenko, N. F. Stepanov, and S. Y. Umanskii, J. Chem. Phys. **106**, 4575 (1997).

[74] R. B. Gerber, M. V. Korolkov, J. Manz, M. Y. Niv, and B. Schmidt, Chem. Phys. Lett. **327**, 76 (2000).

[75] G. C. Maitland, M. Rigby, E. B. Smith, and W. A. Wakeham, *Intermolecular Forces: Their Origin and Determination* (Oxford Science, Oxford, 1987).

[76] K. Rośsciszewski, B. Paulus, P. Fulde, and H. Stoll, Phys. Rev. B **62**, 5482 (2000).

[77] M. P. Allen and D. J. Tildesley, *Computer Simulation of Liquids* (Clarendon, Oxford, 1987).

[78] K. Refson, *Moldy User's Manual* (Oxford University Press, Oxford, 1998).

[79] L. C. Balling and J. J. Wright, J. Chem. Phys. **79**, 2941 (1983).

[80] M. Weissbluth, *Atoms and Molecules* (Academic, London, 1978).

[81] J. C. Tully, in *Semiempirical Methods of Electronic Structure Calculation*, edited by G. A. Segal (Plenum, New York, 1977), Chap. Diatomics-in-Molecules.

[82] V. S. Batista and D. F. Coker, J. Chem. Phys. **105**, 4033 (1996).

[83] E. A. Popov and Y. Dmitriev, private discussion (unpublished).

[84] T. Kiljunen (unpublished).

[85] I. F. Silvera and V. V. Goldman, J. Chem. Phys. **69**, 4209 (1978).

[86] H. Partridge, C. W. Bauschlicher, Jr., J. R. Stallcop, and E. Levin, J. Chem. Phys. **99**, 5951 (1993).

[87] M. Faubel, F. A. Gianturco, F. Ragnetti, L. Y. Rusin, F. Sondermann, U. Tappe, and J. P. Toennies, J. Chem. Phys. **101**, 8800 (1994).

[88] S. M. Cybulski and R. R. Toczyłowski, J. Chem. Phys. **111**, 10520 (1999).

[89] W. R. M. Graham and W. Weltner Jr., J. Chem. Phys. **65**, 1516 (1976).

[90] G. Jeong and K. J. Klabunde, J. Am. Chem. Soc. **108**, 7103 (1986).

[91] A. Berning, M. Schweizer, H.-J. Werner, P. J. Knowles, and P. Palmieri, Mol. Phys. **98**, 1823 (2000).

[92] J. P. Visticot, P. de Pujo, J. M. Mestdagh, A. Lallement, J. Berlande, O. Sublemontier, P. Meynadier, and J. Cuvellier, J. Chem. Phys. **100**, 158 (1994).

[93] J. Eloranta, http://epr.chem.jyu.fi/xemr.

[94] M. T. Hutchings, Solid State Phys. **16**, 227 (1964).

PAPER I

https://doi.org/10.1063/1.479173

Reprinted with permission from T. Kiljunen et al, “Ab Initio and molecular-dynamics studies on rare gas hydrides: Potential energy curves, isotropic hyperfine properties, and matrix cage trapping of atomic hydrogen,” *The Journal of Chemical Physics* **110**, 1999, pp. 11814–11822.

JOURNAL OF CHEMICAL PHYSICS VOLUME 110, NUMBER 24 22 JUNE 1999

Ab initio and molecular-dynamics studies on rare gas hydrides: Potential-energy curves, isotropic hyperfine properties, and matrix cage trapping of atomic hydrogen

Toni Kiljunen,[a] Jussi Eloranta, and Henrik Kunttu
Department of Chemistry, University of Jyväskylä, P.O. Box 35, FIN-40531 Jyväskylä, Finland

(Received 22 February 1999; accepted 31 March 1999)

Ground-state potential-energy curves and distance dependent isotropic hyperfine coupling (IHC) constants for ground-state H–RG (=Ne, Ar, Kr, Xe) are obtained at CCSD(T) (coupled-cluster single double triple) and MP4(SDQ) (fourth-order Moller–Plesset single double quadruple) levels, respectively, with an augmented basis set aug-Stuttgart (RG)/aug-cc-pVQZ (H). The obtained R_m and ϵ are for NeH: 3.45 Å and −1.36 meV; ArH: 3.65 Å and −3.48 meV; KrH: 3.75 Å and −4.32 meV; XeH: 3.90 Å and −5.22 meV. The computed pair potentials are utilized in classical molecular-dynamics simulations of H–RG lattices. Along the classical trajectory, the many-body perturbation on the H atom hyperfine coupling constant is computed by pair-wise addition of the individual RG–H contributions obtained from the present quantum-chemical calculations. The computed IHC shifts are compared with electron paramagnetic resonance (EPR) spectra obtained in low-temperature matrix isolation experiments. For most cases this theoretical treatment agrees very well with the experiment and confirms the previous site assignments. However, for H–Xe, the theory would suggest stability of both interstitial O_h and substitutional sites, whereas only one site is observed in the experiment. Based on the present calculations this site can be assigned as a nearly undistorted substitutional site. © *1999 American Institute of Physics.* [S0021-9606(99)31124-7]

I. INTRODUCTION

The weak van der Waals (vdW) interactions in chemical systems including neutral rare-gas (RG) atoms has been subject to a vast number of previous electronic structure calculations.[1–9] Most of the early work has relied on the multiconfiguration self-consistent field (MCSCF) method in the calculation of interaction energies and equilibrium structures.[1–3] However, the basis set superposition error[4] (BSSE) has not been considered in these studies. Consequently, artificial stabilization along with excessive bond strengths are frequently reported. The most accurate work has concentrated on small diatomics such as the helium dimer, where BSSE effects have thoroughly been accounted for.[4–7] The computational approaches in these investigations are typically based on Møller–Plesset (MP) perturbation theory, coupled cluster (CC), configuration interaction (CI), or multireference CI (MRCI) methods. An important issue affecting the reliability of the method is the size consistency which is fulfilled by MP, CC, and full CI. Since the corrections required for truncated CI approaches are not exact, many of the recent studies on ground-state electronic properties are based on size-consistent theories.

Theoretical description of the H–RG ground-state vdW interaction has been a concern of both theoretical and experimental studies.[2,3,10,11] Although the early MCSCF work by Das *et al.*[3] produced a seemingly good agreement with the scattering data of Ref. 11, the calculated depths of the potential wells exceed the experimental ones for Ne, Ar, and Kr indicating severe shortcomings of the method. On the other hand, interpretation of scattering data in terms of potentials is by no means a straightforward procedure, so there may be some inaccuracies in the experimental results as well. For these obvious reasons, re-evaluation of the pair potential-energy curves (PEC) for RG–H dimers with the present-day methodology is well justified, and yet challenging since we are dealing with very small interaction energies compared to the total electronic energy of the system (order of 1×10^{-5} a.u. vs 10 a.u., respectively). In practice, difficulties arising from this reason are connected to BSSE and incompleteness of the basis set, and are of the same magnitude as the stabilization energy under investigation. Related studies discussing these effects for RG–H_2 have appeared recently.[8,9]

Calculation of the IHC is often referred to be a problematic task for *ab initio* methods. The challenge is in the local nature of the spin-density evaluation, and the isotropic component of the hyperfine interaction, which may also be composed of indirect effects, spin polarization and electron correlation.[12–14] A proper theoretical approach would necessitate a high quality basis set combined with substantial effort in treating the electron correlation. Although evaluation of the Fermi contact term is relatively straightforward for the present system, i.e., hydrogen atom perturbed by a RG atom, we have not compromised either of these requirements. Various theoretical methods have been used in the past for obtaining the IHC constants. The MRCI is often considered as the most accurate method, while density-functional theory (DFT) is widely used for larger systems. Other methods based on unrestricted Hartree–Fock (UHF) wave function

---

[a] Electronic mail: kiljunen@epr.chem.jyu.fi

are MP and CC. In addition to these, the quadratic CI (QCI) has been shown to yield comparative results.[13] The concept of spin contamination supports the use of CC methods: Due to the infinite nature of CC operator the contamination of the underlying UHF is better reduced. Finally, an elegant manifestation of the power of many-body perturbation theory (MBPT) has been presented by Kristiansen and Veseth.[15] We are, however, interested in attaining relative shifts, not absolute values for the coupling, and therefore, only a sparse comparison of methodology is performed in this study.

Classical molecular-dynamics (MD) simulation is a well suited method for studies on time dependent as well as time averaged properties. Crucial for the simulation is the quality of the pair potentials dressed in some convenient analytic formula from which the forces can be evaluated. The use of pair potentials of rather modest accuracy makes some of the earlier MD and Monte Carlo (MC) studies on H–RG systems somewhat doubtful.[16] Most of the latest development in the field has been directed into hybrid quantum–classical or completely quantum methods.[17] However, even for systems containing light atoms, the classical treatment is usually preferred due to its lower computational demand and, moreover, relative straightforward relationship between computed trajectories and various physical observables.

Low-temperature RG solids or matrices doped with atomic hydrogen provide a nearly ideal test ground for our understanding of weak intermolecular interactions at first principles level. The wealth of photophysics, dynamics, and spectroscopy in H–RG being exploited experimentally by electron paramagnetic resonance (EPR), optical absorption spectroscopy, and laser induced fluorescence (LIF) methods is far too vaste to be reviewed in detail. In short, the hydrogen atoms generated by *in situ* photolysis occupy substitutional and octahedral interstitial sites in face-centered-cubic (FCC) lattice as confirmed by both experimental and theoretical work.[18] However, there is still some confusion about the interstitial trapping site symmetries,[19] and some new trapping sites have been recently reported.[20] The hydrogen atom IHC shifts observed in the EPR spectra are interpreted in terms of Pauli repulsion and vdW attraction. The former yields increase and the latter decrease of the IHC compared to the gas-phase value of free H atom.

The first part of this paper concentrates on accurate calculation of the pair potentials of H–RG (=Ne, Ar, Kr, Xe) vdW complexes. Along with the ground-state PECs, the hydrogen atom IHC shifts as a function of RG–H distance are evaluated. The second part deals with MD simulation of the hydrogen atom motion in RG lattices. The aim is at obtaining averaged cage geometries for different trapping sites and, most importantly, rationalization of the observed EPR spectra in terms of cage dynamics and additive IHC.

II. COMPUTATIONAL METHODS

Coupled-cluster theory including single and double excitations with perturbative treatment of the connected triples contribution [CCSD(T)][21] is used as the highest level of theory in obtaining PECs for H–RG pairs. Other methods applied are CCD and fourth-order MP with singles, doubles and quadruples [MP4(SDQ)] for reasons discussed below. BSSE is corrected in all calculations by full Boys–Bernardi (counterpoise, CP) procedure,[22] in which the individual atoms are calculated using the basis set of the supermolecule (RG–H), and these energies are subtracted from the dimer energy at each internuclear distance.

The IHC constant, a_N (in MHz), of H atom is given by the Fermi contact term of the nucleus

$$a_N=(\tfrac{2}{3})\mu_0 g_e g_N \mu_B \mu_N h^{-1}|\psi(0)|^2, \tag{1}$$

where μ_0 is the vacuum permeability, g_e and g_N are the g-values of electron and proton, respectively, and μ_B and μ_N are the Bohr and nuclear magnetons, respectively. The normalized spin density $|\psi(0)|^2$ can be obtained from one particle density matrices by standard methods.[23] This is, however, not implemented in the GAUSSIAN software[24] for methods based on more sophisticated correlation treatment than CCD and MP4(SDQ). Consequently, these two methods are applied in obtaining the IHC constants for RG–H pairs. The IHC shifts, Δa_N, are then obtained by a CP procedure

$$\Delta a_N(R)=a_N^{\mathrm{RGH}}(R)-a_N^{\mathrm{RG''H}}(R), \tag{2}$$

where the first term on the right-hand-side is the CCD/MP4(SDQ) IHC value for a H atom in the RG–H dimer, whereas the second is the IHC calculated with the supermolecule basis, RG being a ghost atom.

An alternative approach for obtaining normalized spin density at the nucleus relies on the finite field perturbation theory, in which the observable property is a first-order response of the system subjected to a perturbation.[25] Thus, the Fermi contact term can be treated as a perturbation associated with a finite field λ in the Hamiltonian, and numerical derivative of the total energy with respect to λ gives the exact response, i.e. the spin density. In the case of an exact wave function the outcome is the well-known Hellmann–Feynman theorem

$$\left|\frac{\partial E(\lambda)}{\partial\lambda}\right|_{\lambda=0}=\langle\Psi|\frac{\partial \mathbf{H}}{\partial\lambda}|\Psi\rangle. \tag{3}$$

It should be stressed out that Eq. (3) does not hold for approximative methods such as CC and MP because their wave functions are not completely optimized with respect to all parameters. Nevertheless, finite field method with proper inclusion of all non-Hellmann–Feynman terms is applicable to models including high excitations, CCSD(T) for example, and the approximative formula for the numerical derivative is[26]

$$|\Psi(0)|^2=\frac{\partial E(\lambda)}{\partial\lambda}=\frac{(E_\lambda-E_{-\lambda})}{2\lambda}. \tag{4}$$

A typical field value of $\pm 5\times 10^{-4}$ a.u. is adapted in this central difference approach. Although finite field approach has shown success if combined with high quality *ab initio* methodology,[14] the procedure proved not to be applicable in the present case.

Due to the methodological limitations, CCD and MP4(SDQ) are the most advanced correlation treatments yielding analytic hyperfine properties within the GAUSSIAN package,[24] we have focused more attention to numerically establish the description of RG electronic structure by means of properly augmented basis sets.[27] Throughout this work, hydrogen is described by the correlation consistent polarized valence quadruple zeta basis set of Dunning augmented with one set of diffuse functions for each angular symmetry (aug-cc-pVQZ).[28] A simple test calculation of static polarizability of hydrogen atom verifies the convergence of this expansion, and thus justifies the use of the quadruple zeta level. As mentioned in Sec. I, our emphasis is strongly on predicting the relative behavior of the IHC rather than its absolute description. This effect is reflected via diffuse functions in the van der Waals region and, consequently, does not necessitate augmentation of any tight s-type Gaussians. In this respect the present computational task differs from ordinary calculation of the Fermi contact contribution for spin–spin coupling.

For RG atoms our approach relies on the effective core potentials (ECP) developed by the Stuttgart group.[29] Realizing that diffuse functions are important in particular for hyperfine properties, and that they contribute significantly to the binding energies of weakly bound system, we were forced to augment the valence part of the Stuttgart basis with a set of diffuse $[1s,1p,1d,1f]$ functions. For Ne and Ar the diffuse augmentation was obtained from the augmented Dunning basis set (aug-cc-pVQZ).[30] Unfortunately, this basis set does not support Kr and Xe so the following relation was used:

$$\frac{\exp(\mathrm{Xe},i)}{\exp(\mathrm{Kr},i)}=\frac{\exp(\mathrm{Kr},i)}{\exp(\mathrm{Ar},i)}=\frac{\exp(\mathrm{Ar},i)}{\exp(\mathrm{Ne},i)}, \tag{5}$$

where $i=\{s,p,d,f\}$ and exp denotes the diffuse function exponent. The rightmost ratio was obtained from the aug-cc-pVQZ basis set. The resulting diffuse parts of all the RGs were multiplied by a RG specific scaling factor C_{RG}:

$$\exp'(\mathrm{RG},i)=C_{\mathrm{RG}}\exp(\mathrm{RG},i), \tag{6}$$

where $\exp'(\mathrm{RG},i)$ is the actual exponent used in the calculations. In order to find optimal scaling factor for each RG a twofold optimization procedure was performed at the CCD level of theory: The CP corrected single point energy of RG–H was minimized while the RG atomic polarizability was targetted at the maximum value. In summary, the resulting number of basis functions is 100 and the basis as a whole is denoted as aug-Stuttgart/aug-cc-pVQZ for RG–H, respectively. Finally, we notice that despite of significant effort, the MRCI approach was not applicable for the RG–H systems due to the lack of a reliable counterpoise procedure for the BSSE correction.

Depending on the level of theory, the potential energy and IHC shift were initially evaluated for each RG–H pair at 10–18 internuclear distances R between 3 and 6 Å. Moreover, the short distance IHC shift turn-over behavior was further examined with additional points below 3 Å. The obtained points were then fitted using a generic function of the form

$$\phi(R)=Ae^{-BR}+\frac{C}{R^{12}}-\frac{D}{R^{4}}-\frac{E}{R^{6}}-\frac{F}{R^{8}}. \tag{7}$$

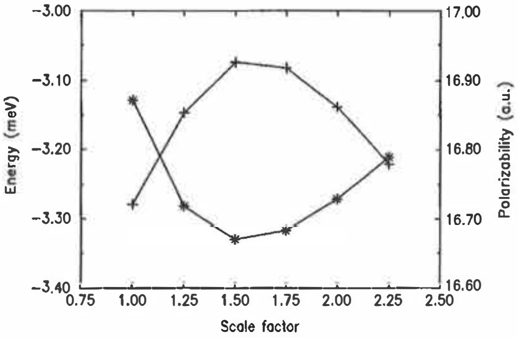

FIG. 1. Optimization of the diffuse set for Kr. The CP corrected CCD energy for KrH (*) and atomic dipole polarizability for Kr (+).

Equation (7) yields sufficiently good fits for both computed quantities. For potential energy the mean deviation between calculated and fitted poins is of the order of 0.01 meV. The RG–RG potentials were obtained from Ref. 31 and least squares fitted to Eq. (7) as well. These two-body interactions were utilized additively to construct the complete potential-energy surface defining the classical force field in which the atoms move. The atom–atom potentials were considered explicitely up to a cutoff at 8 Å and the missing long-range part was compensated by standard procedures.[32] A single hydrogen atom was introduced as a substitutional or interstitial impurity in a perfect FCC lattice consisting of 1371 or 1372 RG atoms, respectively. Initial conditions were generated by assigning velocity for each atom randomly from Maxwell–Bolzmann distribution corresponding to the desired temperature. Prior to collecting the atomic trajectories, the system was allowed to thermalize for 2.5 ps. During the thermalization period standard velocity scaling was applied to regulate the temperature. The system was then followed for an additional 37.5 ps as a micro-canonical (NVE) ensemble. A modified version of the Beeman algorithm[33] with a time step of 0.5 fs was used for integration of the equations of motion. Periodic boundary conditions were considered by the linked-list-method, in which the system is spatially divided into cells interacting only with themselves and with neighboring cells.[34] Finally, the IHC shift of the H-atom was evaluated at each time step by pair-wise summation over all RG–H pairs and stored as a rolling average over 30 time steps.

The calculations reported in this paper were carried out with GAUSSIAN 98 software package[24] and a modified version of the MD software MOLDY.[35]

III. RESULTS AND DISCUSSION

A. *Ab Initio* calculations

The optimized scaling factors C_{RG} for the diffuse sets were 0.5, 0.75, 1.5, and 3.0 for Ne, Ar, Kr, and Xe, respectively. The convergence of this optimization routine for Kr–H at interatomic distance of 3.6 Å is demonstrated in Fig. 1. As observed, most satisfactory situation for both well depth and RG atomic polarizability (α) is obtained with scale factor of 1.5. For comparison, our value of 16.926 a.u. for α

TABLE I. Augmentation of the Stuttgart ECP basis set. Exponents and CCD level atomic dipole polarizabilities α (in a.u.) for rare gases.

	Ne	Ar	Kr	Xe
S	0.0527	0.0457	0.0529	0.0612
P	0.040 89	0.0326	0.0346	0.0369
D	0.1365	0.0870	0.0739	0.0630
F	0.3445	0.2205	0.1875	0.1605
α	2.586	10.937	16.926	27.428
α calc.[a]	2.595	11.076	⋯	⋯
α calc.[b]	2.645	10.974	16.942	27.493
α expt.[c]	2.669	11.08	16.79	27.16

[a] Reference 30, CCSD(T).
[b] Reference 29, CCSD.
[c] Reference 40.

is close to 16.942 a.u. reported by the Stuttgart group at the CCSD level and an extended $[6s,6p,6d,6f]$ basis set.[29] For Ne and Ar, the obtained polarizabilities can also be compared to the actual aug-cc-pVQZ basis set calculations of Dunning,[30] as indicated in Table I. In the weakly bound RG–H species the stabilization energy is strongly dependent on the polarizability of the RG atom, thus increasing from Ne–H to Xe–H. In fact, this effect is clearly observed in the scale factor optimization, where the maximum of the polarizability coincides with the minimum of the binding energy (see Fig. 1). The improvement of the binding energy achieved by scaling varied from 0.05 meV (Ne) to 0.7 meV (Xe). Based on these considerations we feel confident that the augmented ECP set developed here is adequate for describing the electronic properties of RG atoms and, more importantly for our experimental interests, weakly bound RG–H species. The resulting exponents for diffuse sets of $[s,p,d,f]$ functions are listed in Table I.

As mentioned in Sec. II, the requirement of analytic evaluation of the Fermi contact term limited the level of theory to CCD and MP4(SDQ). The use of an extensive basis set limited the highest feasible theories to MP4 and CCSD(T) in the electronic energy calculation. The methodological benchmarking of these methods, based on the pair interaction energy of Ne–H, is presented in Fig. 2. The usually observed order of accuracy, e.g., CCD<MP4(SDQ)<MP4<CCSD(T), is again reproduced and follows the completeness of the method. The obtained CCSD(T) potential energy curves are collected in Fig. 3. Based on their energetics, the curves can be divided into two groups. The NeH dimer possesses relatively shallow well compared to the other group formed by the rest of dimers, which shows a systematic increase in the binding energy. Another observation concerns the shape of the PECs and is illustrated in Fig. 4. Here $E(R)/\epsilon$ are plotted against R/R_m for all RG–H. The reduced potentials of Fig. 4 show again that NeH can be distinguished into its own group the other three being nearly identical.

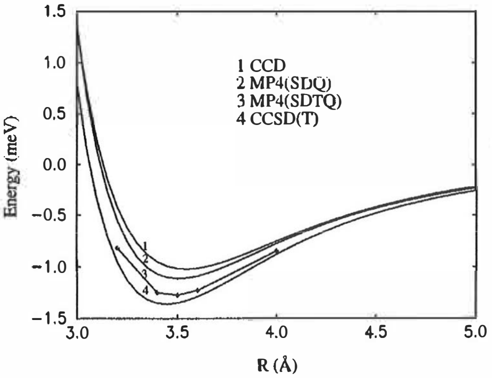

FIG. 2. Comparison of the Ne–H pair interaction obtained in various theoretical treatments. The curves 1, 2, and 4 are fitted according to Eq. (7).

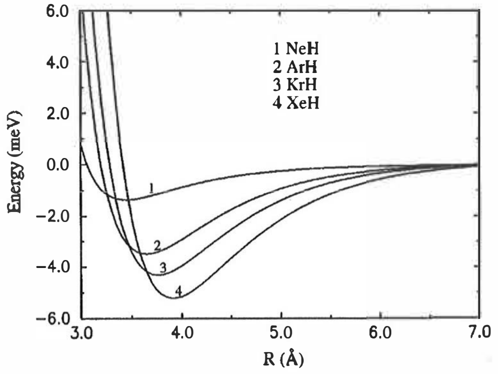

FIG. 3. The CCSD(T) potential-energy curves for rare-gas hydrides. The smooth trend of increase in the well minimum location R_m follows the interpretation of experimental data in Ref. 36.

The full PECs were calculated for RG–H at CCD, MP4(SDQ), and CCSD(T) levels and the obtained well depths and equilibrium distances are given in Table II. Comparison of our CCSD(T) well depths with the experimental numbers of Tang and Toennies[36] shows as much as 26% difference for ArH and KrH, however, the absolute difference being only 1.5 meV. This is well below what is usually

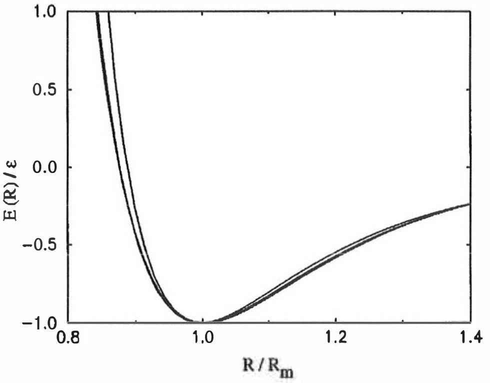

FIG. 4. The reduced potential curves for rare gas hydrides. The curve distinguishing from the others belongs to NeH, whereas ArH, KrH, and XeH behave nearly identically.

TABLE II. Equilibrium distances R_m and minimum potential energies ϵ for rare gas hydrides.

	NeH		ArH		KrH		XeH	
Method	R_m [Å]	ϵ [meV]	R_m [Å]	ϵ [meV]	R_m [Å]	ϵ [meV]	R_m [Å]	ϵ [meV]
CCD	3.55	−1.02	3.75	−2.91	3.85	−3.66	4.00	−4.44
MP4(SDQ)	3.50	−1.11	3.70	−2.91	3.80	−3.62	4.00	−4.37
CCSD(T)	3.45	−1.36	3.65	−3.48	3.75	−4.32	3.90	−5.22
expt.[a]	3.43	−1.49	3.54	−4.67	3.64	−5.82	3.85	−6.20

[a] Reference 36.

considered as the chemical accuracy. On this ground we feel confident to apply these potential data in the molecular-dynamics simulations. Table III gives parametrization of the CCSD(T) potentials in terms of Eq. (7).

An example of the failure of the finite field approach in evaluating the distance dependency of the IHC shifts for RG–H is presented in Fig. 5. The curves shown are obtained at the CCSD(T) level with a value of ±0.0004 a.u. for the perturbative field. The CCD calculations yielded similar results. As observed, the finite field method is unable to model negative shift for IHC in the region where vdW attraction dominates. This is, however, somewhat expected as the two computational strategies [Eqs. (1) and (4)] for IHC should give identical results for fully variational methods only.

The IHC curves obtained directly from one particle MP4(SDQ) spin-density matrices are presented in Fig. 6. The general shape of the IHC curves from relative short distances to the long-range part is rather similar to the pair potentials of Fig. 3, and can thus be fitted to the generic function of Eq. (7). Rather similar curves were obtained from the CCD wave function with the exception of ArH, for which CCD and MP4(SDQ) differ significantly. In fact, CCD predicts a shallow minimum very similar to what is obtained for NeH at the MP4(SDQ) level. These two results are compared in Fig. 7. Due to this obvious inconsistency in systematics we have chosen the MP4(SDQ) results for subsequent MD studies. The minima of the IHC shifts are located at slightly larger internuclear distances than the corresponding PECs, however, the two properties have rather evident correlation with each other. The idea that the magnitude and sign of IHC shift should follow the pair interaction strength was first presented by Adrian[18] and is based on the fact that the density of the unpaired electron at the proton is directly proportional to the vdW energy. At shorter internuclear distances an abrupt turn-over of the spin density, and Fermi contact term, is observed indicating extensive shielding of the unpaired electron from the proton. The points of the IHC collapse are located at 3.0, 2.5, 2.2, and 1.7 Å for Xe, Kr, Ar, and Ne, respectively. For comparison a recent study by Meyer and Frommhold showed the same effect starting at 1.6 Å for He–H.[37] Although the turn-over for lighter rare gases is associated with distances not accessible due to strong repulsion, it may have implications for the EPR spectra of H doped Xe solids.

TABLE III. The pair potential fit based on Eq. (7) for RG–H dimers at CCSD(T) level. All values are in dimensions that yield energy in meV.

	NeH	ArH	KrH	XeH
A	−13.6301	−0.285 006	−44.5745	−43.24
B	51.8535	4.8541	22.3272	19.5649
C	$2.985\,74\cdot 10^6$	−10 480.9	$-6.851\,37\cdot 10^6$	$-1.575\,41\cdot 10^7$
D	−91.2163	−905.45	−1566	−2337.43
E	7670.24	56 894.7	97 855.4	155 242
F	−29 996.9	−487 555	−932 289	$-1.609\,13\cdot 10^6$

For weakly interacting systems such as vdW complexes, BSSE may contribute a significant fraction of the binding energy and thus yield artificially short equilibrium distances. This problem is routinely corrected by standard CP correction procedure. The present work is not an exception in this respect. Since the effect of BSSE on energy and bonding is rather well understood, we will not discuss it in detail. However, to demonstrate the importance of BSSE in RG–H we note that neglect of BSSE correction at CCSD(T) level for XeH yield R_m and ϵ of 3.65 Å and −8.63 meV, respectively. This corresponds to ~65% error in energy. Table IV shows the effect of BSSE on the IHC curves. Here BSSE in corrected by a CP-type procedure of Eq. (2). As observed, only for NeH BSSE affects energetics and IHC in a similar manner. For the other dimers this effect is less noteworthy and not systematic. This would prevent further conclusions of this issue. Instead, BSSE seems to act as a shape determining factor for the IHC curves. The implication of the CP correction is that the region of negative IHC shift extends to larger internuclear distances, hence increasing the contribution of the distant RG atoms on the H atom EPR spectrum under matrix isolation conditions.

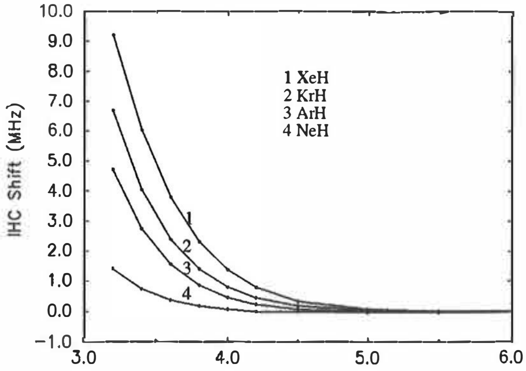

FIG. 5. The shifts of hydrogen atom isotropic hyperfine coupling constant for rare-gas hydrides obtained with finite field approach at the CCSD(T) level of theory.

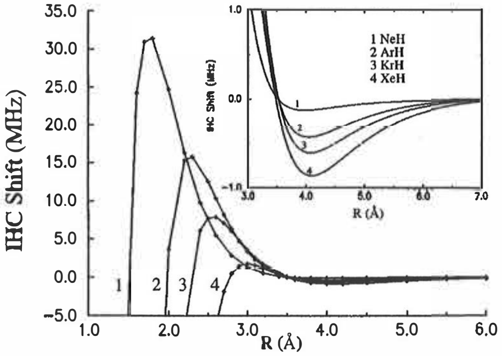

FIG. 6. The distance dependency of IHC shifts for RG–H pairs as obtained analytically from the MP4(SDQ) spin densities. The insert shows the fit [Eq. (7)] of the data between 3.0 and 7.0 Å.

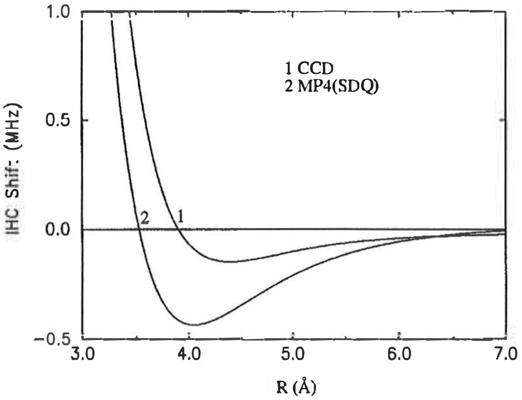

FIG. 7. Comparison of CCD and MP4(SDQ) IHC shifts for ArH.

B. Simulations

The purpose of the present MD simulations is to obtain classical trajectories for nuclear motion in a lattice with a single H atom introduced as a substitutional or interstitial impurity. Along the trajectory we then compute the many-body perturbation on the H atom IHC. This is accomplished by pair-wise addition of the individual RG–H contributions obtained from accurate quantum-chemical calculations (see Fig. 6). There are two major approximations involved in this approach, namely classical treatment of the H atom motion, and the assumption of pair-wise additive IHC shift. Implications of the first one are neglect of the zero-point energy of the light H atom and continuous energy spectrum of its caged motion. The error due to three-body and higher order terms on IHC shift is not straightforward to quantify. A realistic guess for the error would be few percent as is the case for three-body terms in potential energy. These effects would obviously be operative at short distances, i.e., in tight interstitial trapping sites. In practice, the requirement of very accurate wave function for evaluation of the Fermi contact term necessitates the use of computational approaches presently afforded for small systems only. It should be emphasized that according to our knowledge the present investigation is the first one of this type and the existing literature does not provide supporting backup. Thus, besides providing quantitative predictions for the IHC constants for different trapping sites in H–RG lattices, our aim is to demonstrate the prospects of the mixed quantum–classical approach extracting structural information from EPR spectra.

Tables V–VIII summarize the results of the present simulations and compare the relative IHC shifts with those obtained experimentally in low-temperature matrices. As seen in Table V, the MD simulations would suggest that H atoms trap exclusively in substitutional cavities in Ne lattice. The final number of nearest neighbors and the nearest-neighbor distance in the equilibrated simulation shell are rather insensitive to the initial symmetry of the H atom site. Thus, extensive lattice relaxation removes memory of the octahedral and tetrahedral interstitial sites in time scale of the simulation at all temperatures. The final Ne–H distance of 3.1 Å corresponds to the Ne–Ne equilibrium distance and shows nearly zero interaction along the Ne–H coordinate. Interpretation of the H–Ne matrix EPR spectrum based on the IHC curves in Fig. 6 would clearly involve positive IHC shift of ~1 MHz/atom due to the nearest neighbors and partial cancellation by the negative contribution of the second solvation shell. Taken into account the approximations involved in the calculations, the agreement between experiment and theory is satisfactory and confirms the previous tentative site assignment rather nicely.[18]

For H–Ar lattice the MD simulations predict stability of both substitutional and O_h interstitial sites (Table VI). In the latter case, thermalization of the system yields conciderable expansion of the cavity due to repulsive Ar–H interaction and subsequent lattice relaxation. In fact, the O_h site in Ar is the smallest cavity where H atoms could be stabilized. Initiation of trajectories from tight T_d sites terminated in struc-

TABLE IV. The effect of BSSE on calculated IHC properties. The well depths ϵ (MHz) and locations of the well minima R_m (Å) are tabulated with and without CP correction at CCD and MP4(SDQ) levels of theory.

		NeH		ArH		KrH		XeH	
Method		R_m [Å]	ϵ [MHz]	R_m [Å]	ϵ [MHz]	R_m [Å]	ϵ [MHz]	R_m [Å]	ϵ [MHz]
CCD	CP	4.00	−0.117	4.40	−0.148	4.10	−0.600	4.10	−0.842
	no CP	3.95	−0.141	4.30	−0.164	4.05	−0.573	4.10	−0.788
MP4	CP	4.00	−0.126	4.05	−0.432	4.10	−0.609	4.10	−0.866
	no CP	3.90	−0.173	4.00	−0.426	4.05	−0.619	4.05	−0.791

TABLE V. Trapping site structure and IHC shifts for H–Ne lattice as obtained from MD simulations at various temperatures. The IHC shifts are calculated from the trajectory by pair-wise summation of contributions due to individual H–Ne pairs [see Eq. (2)]. δ refers to the Gaussian width of the transition distribution. The simulation shell consists of 1371 or 1372 Ne atoms and a single H atom. The total simulation time is 40 ps.

T/K	Initial site	Nearest neighbors initial–final	R_{RgH} initial–final [Å]	IHC shift [MHz]	δ [MHz]
5	subs.	12/12	3.1/3.1	+5.0	1.0
10	subs.	12/12	3.1/3.1	+5.5	1.3
15	subs.	12/12	3.1/3.1	+5.9	1.5
20	subs.	12/12	3.1/3.1	+6.1	1.7
5	O_h	6/12	2.2/3.2	+4.0	2.0
10	O_h	6/12	2.2/3.2	+4.7	1.8
15	O_h	6/12	2.2/3.1	+5.5	2.0
20	O_h	6/12	2.2/3.1	+6.3	2.1
4	T_d	4/12	1.9/3.1	+4.2	2.4
4	Experimental Ne matrix			+6.1[a]	

[a] Reference 18, IHC shift with respect to experimental free atom value of 1420.4 MHz.

tures with six nearest neighbors and internuclear distances similar to the O_h site. Inspection of the IHC curves in Fig. 6 suggests that at Ar–H distance of 3.6 Å, corresponding to the thermalized substitutional cavity, the perturbation of the Fermi contact term by the nearest neighbors is small. Hence, about half of the total contribution to the negative ∼−3.5 MHz IHC shift is due to contribution of more distant Ar atoms. For the tight O_h site, where the nearest-neighbor Ar–H pair interaction in strictly repulsive, the net perturbation due to Ar atoms is realized as a large positive IHC shift. For this site both positive (Pauli repulsion) and negative (vdW attraction) contributions are simultaneously effective providing an excellent test case for theory. Considering the approximations involved in the calculations, the correspondence between experiment and theory is quite satisfactory. Finally, we note that in a recent EPR investigation by Komaguchi *et al.* on x-ray irradiated H_2–Ar solids yielded three distinct H atom doublets with IHC shifts +24.4, +21.0, and +1.7 MHz.[19] These resonances were assigned to T_d, O_h, and substitutional sites, respectively. The obvious contradiction between Ref. 19 and the rest of the literature on the subject[18,20] may be at least partially due to different sample preparation technique (frozen solution) applied in Ref. 19.

The situation in H–Kr lattice resembles that described for Ar. The H atom fits rather perfectly in a substitutional cavity and only very minor compression of the cage is observed in the MD simulations (Table VII). Since the obtained nearest-neighbor distance of ∼4 Å has a close coincidence with the Kr–H pair potential minimum, the interpretation of the negative IHC shift is straightforward and can be ascribed

TABLE VI. Trapping site structure and IHC shifts for H–Ar lattice as obtained from MD simulations at various temperatures. The IHC shifts are calculated from the trajectory by pair-wise summation of contributions due to individual H–Ar pairs [see Eq. (2)]. δ refers to the Gaussian width of the transition distribution. The simulation shell consists of 1371 or 1372 Ar atoms and a single H atom. The total simulation time is 40 ps.

T/K	Initial site	Nearest neighbors initial–final	R_{RgH} initial–final [Å]	IHC shift [MHz]	δ [MHz]
5	subs.	12/12	3.7/3.6	−3.9	0.3
10	subs.	12/12	3.7/3.6	−3.7	0.5
20	subs.	12/12	3.7/3.6	−3.5	0.5
30	subs.	12/12	3.7/3.6	−3.1	0.8
40	subs.	12/12	3.7/3.6	−2.6	1.0
4	Experimental Ar matrix			−6.5[a]	
5	O_h	6/6	2.6/2.9	+20.9	4.2
10	O_h	6/6	2.6/2.9	+20.9	3.5
20	O_h	6/6	2.6/2.9	+21.1	3.3
30	O_h	6/6	2.6/2.9	+20.9	3.7
40	O_h	6/6	2.6/2.9	+20.7	3.8
4	Experimental Ar matrix			+16.3[a]	
5	T_d	4/6	2.3/2.9	+20.4	3.1

[a] Reference 18, IHC shift with respect to experimental free atom value of 1420.4 MHz.

TABLE VII. Trapping site structure and IHC shifts for H–Kr lattice as obtained from MD simulations at various temperatures. The IHC shifts are calculated from the trajectory by pair-wise summation of contributions due to individual H–Kr pairs [see Eq. (2)]. δ refers to the Gaussian width of the transition distribution. The simulation shell consists of 1371 or 1372 Kr atoms and a single H atom. The total simulation time is 40 ps.

T/K	Initial site	Nearest neighbors initial–final	R_{RgH} initial–final [Å]	IHC shift [MHz]	δ [MHz]
5	subs.	12/12	4.0/4.0	−7.4	0.1
10	subs.	12/12	4.0/3.9	−7.2	0.3
20	subs.	12/12	4.0/3.8	−6.8	0.6
30	subs.	12/12	4.0/4.0	−6.4	0.8
40	subs.	12/12	4.0/3.9	−6.5	0.7
4	Experimental Kr matrix			−8.38[a]	
5	O_h	6/6	2.9/3.1	+11.4	2.1
10	O_h	6/6	2.9/3.1	+11.6	1.8
20	O_h	6/6	2.9/3.1	+11.6	2.0
30	O_h	6/6	2.9/3.1	+11.8	2.5
40	O_h	6/6	2.9/3.0	+11.3	2.6
4	Experimental Kr matrix			+6.7[a]	
5	T_d	4/6	2.5/3.0	+10.8	1.8

[a] Reference 18, IHC shift with respect to experimental free atom value of 1420.4 MHz.

TABLE VIII. Trapping site structure and IHC shifts for H–Xe lattice as obtained from MD simulations at various temperatures. The IHC shifts are calculated from the trajectory by pair-wise summation of contributions due to individual H–Xe pairs [see Eq. (2)]. δ refers to the Gaussian width of the transition distribution. The simulation shell consists of 1371 or 1372 Xe atoms and a single H atom. The total simulation time is 40 ps.

T/K	Initial site	Nearest neighbors initial–final	R_{RgH} initial–final [Å]	IHC shift [MHz]	δ [MHz]
5	subs.	12/12	4.4/4.3	−9.4	0.2
10	subs.	12/12	4.4/4.3	−9.3	0.2
20	subs.	12/12	4.4/4.2	−8.8	0.6
30	subs.	12/12	4.4/4.3	−9.1	0.4
40	subs.	12/12	4.4/4.2	−8.9	0.5
4	Experimental Xe matrix			−14.77[a]	
5	O_h	6/6	3.1/3.2	+2.6	0.8
10	O_h	6/6	3.1/3.2	+2.5	0.7
20	O_h	6/6	3.1/3.2	+2.4	0.8
30	O_h	6/6	3.1/3.2	+2.3	1.1
40	O_h	6/6	3.1/3.2	+2.3	1.1
5	T_d	4/6	2.7/3.2	+1.1	1.0

[a] Reference 18, IHC shift with respect to experimental free atom value of 1420.4 MHz.

mostly to nearest-neighbor interactions and the contribution of the second solvation shell is small. Quite the opposite is observed for the O_h trapping site. This site shows significant repulsion in the Kr–H pair interaction (Fig. 3) and, consequently, a large net positive IHC shift composed of a positive nearest-neighbor contribution and a small negative one due to more distant Kr atoms. In this case the theory tends to overestimate the IHC shift, however, the site assignment is unambiguous.

The simulation data in Table VIII for H–Xe would predict the existence of two stable trapping sites for H atoms in Xe samples of FCC structure. The substitutional site shows slight compression from a perfect lattice structure, and a relatively large negative IHC shift. The relaxed structure coincides rather closely with the Xe–H pair potential minimum and would imply strictly negative IHC shift contributions of all closest Xe–H pairs (see Fig. 6). On the other hand, the H atom trapped in an O_h site is subject to significant repulsion, which in turn yields strong positive IHC shift due to the nearest neighbor Xe atoms. The positive shift is, however, almost entirely cancelled by the long-range negative IHC shift. The imbalance of these effecs would predict a IHC shift of +2 MHz for the O_h site. The high-resolution EPR spectrum of H doped Xe matrix shows very complex line patterns due to superhyperfine coupling due to magnetic ^{129}Xe and ^{131}Xe nuclei.[18] Although the experimental site assignment, i.e., substitutional vs O_h, has been subject to some contradiction, it is generally accepted that a single trapping site is responsible for the observed resonances.[18] Our data would clearly suggest this site as a nearly undistorted substitutional site. Experiments with monoisotopic Xe combined with present-day spectral simulation tools would resolve this issue. The very weak EPR signal due to H atoms trapped in Xe[38] and the nonexistence of O_h sites is hard to justify based on the pair potentials and MD simulations, which would claim thermal stability of this site. Furthermore, the recently discovered rich chemistry of thermally mobilized H atoms would clearly imply that the number density of trapped H atoms in photolysed HX–Xe solids is, indeed, high.[39] The turn-over of the IHC curve for XeH occurs relatively close to the average Xe–H distance in thermalized O_h site. Near this distance it is quite expected that the pair-additivity of the IHC might not be a valid assumption and, consequently, the EPR spectrum of H atom may change dramatically. Experiments to unravel the possible exitence of ''magnetically transparent'' H atoms in Xe matrix are underway.

IV. CONCLUSIONS

We have reported accurate ground-state potential-energy curves and distance dependent shifts of the isotropic hyperfine coupling constant for RG–H pairs. For RG–H distances near the potential-energy minimum the two curves show rather similar shape. However, at short internuclear separation the Fermi contact term shows a dramatic turn-over and a change of sign. The obtained potential data is used in MD simulations of H–RG lattices to investigate the structure and stability of different trapping sites. Along the classical trajectory, the IHC shift of the H atom is calculated pair-wisely from individual diatomic contributions. It is shown that this approach, indeed, yields rather similar total IHC shifts to those reported from low-temperature matrices. For most cases the theory confirms the experimental site assignment. However, for H doped Xe lattice there is an obvious contradiction between experiment and theory.

ACKNOWLEDGMENT

The Center of Scientific Computing (CSC, Espoo Finland) is acknowledged for providing computer resources.

[1] G. Das and A. C. Wahl, Phys. Rev. A **4**, 825 (1971).

[2] A. F. Wagner, G. Das, and A. C. Wahl, J. Chem. Phys. **60**, 1885 (1974).

[3] G. Das, A. F. Wagner, and A. C. Wahl, J. Chem. Phys. **68**, 4917 (1978).

[4] B. Liu and A. D. McLean, J. Chem. Phys. **59**, 4557 (1973).

[5] F.-M. Tao, J. Chem. Phys. **98**, 3049 (1993).

[6] B. Liu and A. D. McLean, J. Chem. Phys. **91**, 2348 (1989); R. J. Vos, F. B. van Duijneveldt, and J. H. van Lenthe, Mol. Phys. **67**, 1011 (1989); R. J. Vos, J. H. van Lenthe, and F. B. van Duijneveldt, J. Chem. Phys. **93**, 643 (1990); F-M. Tao and Y-K. Pan, *ibid.* **97**, 4989 (1992); E. P. F. Lee, J. Chem. Soc., Faraday Trans. **89**, 645 (1993); I. Mayer, Á. Vibók, and P. Valiron, Chem. Phys. Lett. **224**, 166 (1994).

[7] D. E. Woon, J. Chem. Phys. **100**, 2838 (1993).

[8] W. Meyer, P. C. Hariharan, and W. Kutzelnigg, J. Chem. Phys. **73**, 1880 (1980); D. W. Schwenke, S. P. Walch, and P. R. Taylor, *ibid.* **98**, 4738 (1993); C. Bissonette, C. E. Chuaqui, K. G. Crowell, R. J. Le Roy, R. J. Wheatley, and W. J. Meath, *ibid.* **105**, 2639 (1996).

[9] N. Runeberg, M. Seth, and P. Pyykkö, Chem. Phys. Lett. **246**, 239 (1995).

[10] D. Bassi, M. G. Dondi, F. Tommasini, F. Torello, and U. Valbusa, Phys. Rev. A **13**, 584 (1976).

[11] J. P. Toennies, W. Welz, and G. Wolf, J. Chem. Phys. **71**, 614 (1979).

[12] D. M. Chipman, Theor. Chim. Acta **82**, 93 (1992).

[13] D. Feller, J. Chem. Phys. **93**, 579 (1990).

[14] D. Feller, E. D. Glendening, E. A. McCullough, Jr., and R. J. Miller, J. Chem. Phys. **99**, 2829 (1993).

[15] P. Kristiansen and L. Veseth, J. Chem. Phys. **84**, 2711 (1986); **84**, 6336 (1986).

[16] M. Perry, G. J. Mains, and L. M. Raff, J. Phys. Chem. **98**, 13766 (1994).

[17] A. García-Vela and R. B. Gerber, J. Chem. Phys. **98**, 427 (1993); **103**, 3463 (1995).

[18] S. Foner, E. L. Cochran, V. A. Bowers, and C. K. Jen, J. Chem. Phys. **32**, 963 (1960); F. J. Adrian, *ibid.* **32**, 972 (1960); J. R. Morton, K. F. Preston, S. J. Strach, F. J. Adrian, and A. N. Jette, *ibid.* **70**, 2889 (1979); W. Weltner, Jr., *Magnetic Atoms and Molecules* (Dover, New York, 1983).

[19] K. Komaguchi, T. Kumada, Y. Aratono, and T. Miyazaki, Chem. Phys. Lett. **268**, 493 (1997).

[20] K. Vaskonen, J. Eloranta, T. Kiljunen, and H. Kunttu, J. Chem. Phys. **110**, 2122 (1999).

[21] K. Raghavachari, G. W. Trucks, J. A. Pople, and M. Head-Gordon, Chem. Phys. Lett. **157**, 479 (1989).

[22] S. F. Boys and F. Bernardi, Mol. Phys. **19**, 553 (1970).

[23] R. McWeeny, *Methods of Molecular Quantum Mechanics* (Academic, London, 1992).

[24] GAUSSIAN 98, Revision A.3, M. J. Frisch, G. W. Trucks, H. B. Schlegel, G. E. Scuseria, M. A. Robb, J. R. Cheeseman, V. G. Zakrzewski, J. A. Montgomery, Jr., R. E. Stratmann, J. C. Burant, S. Dapprich, J. M. Millam, A. D. Daniels, K. N. Kudin, M. C. Strain, O. Farkas, J. Tomasi, V. Barone, M. Cossi, R. Cammi, B. Mennucci, C. Pomelli, C. Adamo, S. Clifford, J. Ochterski, G. A. Petersson, P. Y. Ayala, Q. Cui, K. Morokuma, D. K. Malick, A. D. Rabuck, K. Raghavachari, J. B. Foresman, J. Cioslowski, J. V. Ortiz, B. B. Stefanov, G. Liu, A. Liashenko, P. Piskorz, I. Komaromi, R. Gomperts, R. L. Martin, D. J. Fox, T. Keith, M. A. Al-Laham, C. Y. Peng, A. Nanayakkara, M. Challacombe, P. M. W. Gill, B. Johnson, W. Chen, M. W. Wong, J. L. Andres, C. Gonzalez, M. Head-Gordon, E. S. Replogle, and J. A. Pople, Gaussian, Inc., Pittsburgh, PA, 1998.

[25] J. A. Pople, J. W. McIver, Jr., and N. S. Ostlund, J. Chem. Phys. **49**, 2960 (1968).

[26] H. Sekino and R. J. Bartlett, J. Chem. Phys. **82**, 4225 (1985).

[27] Basis sets were obtained from the Extensible Computational Chemistry Environment Basis Set Database, Version 1.0, as developed and distributed by the Molecular Science Computing Facility, Environmental and Molecular Sciences Laboratory which is part of the Pacific Northwest

Laboratory, P.O. Box 999, Richland, Washington 99352, USA, and funded by the U.S. Department of Energy. The Pacific Northwest Laboratory is a multi-program laboratory operated by Battelle Memorial Institute for the U.S. Department of Energy under contract DE-AC06-76RLO 1830. Contact David Feller, Karen Schuchardt, or Don Jones for further information.

[28] R. A. Kendall, T. H. Dunning, Jr., and R. J. Harrison, J. Chem. Phys. **96**, 6796 (1992).

[29] A. Nicklass, M. Dolg, H. Stoll, and H. Preuss, J. Chem. Phys. **102**, 8942 (1995).

[30] D. E. Woon and T. H. Dunning, Jr., J. Chem. Phys. **100**, 2975 (1994).

[31] G. C. Maitland, M. Rigby, E. B. Smith, and W. A. Wakeham, *Intermolecular Forces: Their Origin and Determination* (Oxford Science Publications, Oxford, 1987).

[32] M. P. Allen and D. J. Tildesley, *Computer Simulations of Liquids* (Claredon, Oxford, 1987).

[33] D. Beeman, J. Comput. Phys. **20**, 130 (1976); K. Refson, Physica B **131**, 256 (1985).

[34] B. Quentrec and C. Brot, J. Comput. Phys. **13**, 430 (1975).

[35] K. Refson, *Moldy User's Manual* (Oxford University Press, Oxford, 1998).

[36] T. Tang and J. P. Toennies, Chem. Phys. **156**, 413 (1991).

[37] W. Meyer and L. Frommhold, Theor. Chim. Acta **88**, 201 (1994).

[38] J. Eloranta, K. Vaskonen, and H. Kunttu, J. Chem. Phys. **110**, 7917 (1999).

[39] M. Pettersson, J. Lundell, L. Khriachtchev, and M. Räsänen, J. Chem. Phys. **109**, 618 (1998), and references therein.

[40] A. Kumar and W. J. Meath, Can. J. Chem. **63**, 1661 (1985).

PAPER II

https://doi.org/10.1063/1.480825

Reprinted with permission from J. Ahokas, T. Kiljunen et al, “Theoretical analysis of alkali metal trapping sites in rare gas matrices,” *The Journal of Chemical Physics* **112**, 2000, pp. 2420–2426.

JOURNAL OF CHEMICAL PHYSICS VOLUME 112, NUMBER 5 1 FEBRUARY 2000

Theoretical analysis of alkali metal trapping sites in rare gas matrices

Jussi Ahokas, Toni Kiljunen,[a] Jussi Eloranta, and Henrik Kunttu
Department of Chemistry, University of Jyväskylä, P.O.Box 35, FIN-40351 Jyväskylä, Finland

(Received 13 July 1999; accepted 9 November 1999)

The rare gas (Ne, Ar, Kr, Xe)–alkali metal (Li, Na) ground-state pair interaction potentials and distance-dependent isotropic hyperfine coupling constants are evaluated by coupled-cluster approaches at the van der Waals region of the dimers. The computed properties are further utilized in classical molecular dynamics simulations of rare gas lattices doped with alkali atoms. Atomic trajectories and time averaged hyperfine constants are obtained from the simulations and exploited to provide theoretical insights into experimentally observed atomic trapping and dynamics of alkali metal atoms in rare gas matrices. The simulations support our previous electron paramagnetic resonance (EPR) data [Chem. Phys. Lett, **310**, 245 (1999)], suggesting that alkali metal atoms, while generated by laser vaporization, do trap in single substitutional sites, whereas thermal atom sources yield trapping in multiple substitutional sites. In order to theoretically reproduce the EPR spectra for the latter case, more than six neighboring vacancies had to be included in the model system. Based on the simulations, the trapped atoms are able to move rather freely within the extended cage. [S0021-9606(00)30705-X]

I. INTRODUCTION

Alkali metal atoms (M; Li or Na) trapped in solid rare gas (Rg; Ne, Ar, Kr, or Xe) matrices have been subject to a number of experimental studies by optical and magnetic resonance spectroscopies.[1–5] In the early studies, a Knudsen oven atom source was used for vaporizing the alkali metal into the sample chamber. Electron paramagnetic resonance (EPR) measurements indicate that samples prepared by this method yield trapping in two or more different matrix sites. Arguments based on the strongly repulsive nature of the ground-state Rg–M pair potential have led to the conclusion that multiple substitutional sites are responsible for M atom trapping.[6] Previously, Fajardo *et al.*[7] introduced a new sample preparation method based on laser ablation of the alkali metal target which revealed, according to the optical absorption spectra, a new atomic trapping site. More recently, trapping sites were characterized in detail by Vaskonen *et al.*[5] using EPR spectroscopy and a semiempirical theory developed by Adrian.[8] The conclusion derived from this investigation was that the novel site is, indeed, due to purely substitutional trapping. Further experimental evidence for such a tight trapping site was extracted from the observed strong isotropic superhyperfine coupling between the unpaired electron of the alkali metal atom and the magnetic nuclei of the Xe matrix atoms.

Atomic ground-state pair interaction between Rg and M atoms within their van der Waals (vdW) region has been studied both experimentally (by scattering[9] and laser spectroscopic[10] means) and theoretically.[11–13] Despite the number of theoretical studies, most of the effort has been concentrated in semiempirical description of the interaction potentials.[11] Only a limited number of *ab initio* electronic structure calculations with either all-electron or pseudopotential approach has been carried out for ground-state vdW interactions between alkali metal atoms and rare gases. More recent and the most accurate of these studies considers lighter rare gases (He and Ne),[12] whereas somewhat dated work exists for heavier systems (Ar and Xe).[13] Moreover, problems associated with the size consistency of the computational model as well as the basis-set superposition errors (BSSE) have not been carefully analyzed in the existing studies. In this respect, modern size-consistent methods such as the coupled-cluster (CC) theory provide significant improvement compared to the previously adapted methods. In addition, elimination of the BSSE from the computed pair interaction energies is currently well established. When dealing with very small interaction energies, as is the case for weak vdW interactions, careful consideration of both of these aspects is crucial for the obtained computational accuracy.

When M atoms are trapped in Rg matrix, the isotropic hyperfine coupling (IHC), i.e., an observable of the EPR measurement, is shifted with respect to the gas phase isolated atom values. The IHC shifts are either positive or negative, and characteristic of the size and geometry of the trapping site. Adrian[8] has presented a semiempirical theory for aiding the interpretation of the IHC shifts observed in matrices. In short, the theory is based on the following straightforward effects being operational in dense medium: Pauli repulsion which causes orbital compression of the unpaired M atom electron and hence a positive IHC shift, and vdW attraction having the opposite effect on the electron density. The latter would then yield a negative IHC shift. Thus, for tight trapping sites positive IHC shifts are observed and, correspondingly, loose trapping sites are characterized with negative IHC shifts. Recently, Kiljunen *et al.*[14] have combined electronic structure *ab initio* calculations with classical molecular dynamics (MD) simulations for obtaining the IHC shifts for hydrogen atoms trapped in Rg matrices. The pair inter-

---

[a] Electronic mail: kiljunen@epr.chem.jyu.fi

0021-9606/2000/112(5)/2420/7/$17.00

action potentials and distance-dependent IHC curves were calculated by CC-based methods and the thermally averaged many-body IHC shifts and site structures were obtained from classical trajectories. This relatively straightforward approach was shown to yield a satisfactory agreement with the experimentally observed IHC shifts of hydrogen atoms trapped in low-temperature matrices.

In this study, we have computed the pair interaction potentials and distance-dependent IHC curves for Rg–M dimers within their vdW region. We further extend the methodology developed in Ref. 14 to model various trapping sites of Rg matrices doped with M atoms. It will be shown that the EPR spectra obtained for laser vaporized samples is most evidently due to only slightly perturbed substitutional trapping, whereas thermal atom sources create a number of lattice vacancies near the trapping centers.

II. COMPUTATIONAL DETAILS

The ground-state pair interaction energies of Rg–M dimers were obtained by using the coupled-cluster single double triple CCSD(T) method,[15] which includes single and double excitations and uses a perturbative treatment for the connected triples for all electrons. The underlying reference state for CC was obtained by the unrestricted Hartree–Fock (UHF) method. In order to obtain interaction energies of sufficient quality for the vdW region, the Dunning cc-pVQZ basis set[16] was used for alkali metal atom and the augmented Stuttgart ECP basis set[14,17] for Rg. The number of explicitly treated electrons was thus 11 for Li–Rg pairs and 19 for Na–Rg pairs. The BSSE artifacts were removed from the atomic pair interaction energies by the Boys–Bernardi counterpoise method.[18] The interaction energies were evaluated in the 3–20 Å range at 20–25 different internuclear distances. For simulation purposes, the resulting data were parametrized by the following function:

$$\phi(R)=Ae^{-BR}+\frac{C}{R^{12}}-\frac{D}{R^{6}}-\frac{E}{R^{8}}, \tag{1}$$

where R is the internuclear distance between the two nuclei (in Å) and A, B, C, D, and E are parameters specific to the interacting pair of atoms. All parameters are given in units which return energy $\phi(R)$ in eV. On the contrary to the model potential studies of Ref. 11, the actual form of the applied potential function is not important to our interests. The purpose is to accurately represent the calculated energies in some analytic form from which energy gradient, the force between pairs of atoms, can be conveniently evaluated. The selected potential form is essentially a modified version of the Buckingham potential augmented with an additional positive Lennard-Jones type R^{-12} term for repulsion. The least-squares fitted parameters of Eq. (1) yielded a well-defined potential energy curve with an average deviation of 0.04 meV for the computed energy points. The CC calculations were performed using the GAUSSIAN98 program.[19]

The isotropic hyperfine coupling constant (a_N in MHz) can be obtained from the normalized spin density at the given nucleus N by the following relation:

$$a_N=(2/3)\mu_0 g_e g_N \mu_B \mu_N h^{-1}|\Psi(0)|^2, \tag{2}$$

where μ_0 is the vacuum permeability, g_e and g_N are the g values of free electron and the alkali metal atom, respectively, and μ_B and μ_N are the Bohr and nuclear magnetons, respectively. The normalized spin density $|\Psi(0)|^2$ can be computed from one-particle spin density matrices by standard methods.[20] In the applied software, the required spin density matrices are not available at the CCSD(T) level and therefore the IHC calculations were performed at the CCD level only. It should be noted that the method where Fermi contact term is treated as perturbation and the IHC is obtained via finite difference approximation is not applicable here, as we have shown earlier.[14] In this study we aim at calculating the alkali metal atom IHC shift (with respect to the gas phase value) as a function of Rg–M distance, and therefore it is not necessary to add any tight s-type Gaussians into the alkali metal atom basis set, as is the case for evaluation of absolute values of the Fermi contact term. The obtained IHC curves were corrected for BSSE by the Boys–Bernardi type procedure as outlined in Ref. 14. Finally, instead of fitting to Eq. (1), a linear interpolation procedure of the numerical data was used for pairwise evaluation of the IHC shift for the caged atom.

The MD simulations were carried out in a microcanonical ensemble (NVE) employing only two-body interactions of the form given in Eq. (1). Parameters of Eq. (1) for Rg–M pairs were obtained as described above, whereas for the Rg–Rg pairs we rely on the experimental data of Ref. 21 least-squares fitted to Eq. (1). Pair interactions were explicitly evaluated up to 8 Å (Ne and Ar) or 9 Å (Kr and Xe) and the missing long-range part was compensated by standard procedures.[22] The simulation cube was constructed by generating a face-centered-cubic (fcc) Rg lattice (1372 Rg atoms or less) with a lattice constant indicated by the Rg–Rg pair-potential minimum. A single alkali metal atom was then introduced as an octahedral, single substitutional, or multiple substitutional impurity. Initial conditions for the simulation were generated by assigning velocity for each atom randomly from Maxwell–Boltzmann distribution corresponding to the desired temperature (5 K for Ne and 15 K for other Rgs). Prior to collecting the atomic trajectories and IHC data, the system was allowed to thermalize for 2.5 ps. During thermalization a standard velocity scaling was applied to regulate the temperature. After this period, thermally averaged quantities were collected during the main simulation period of 17.5 ps. A modified version of the Beeman algorithm[23] with a time step of 0.5 fs was used for integration of the equations of motion. Periodic boundary conditions were considered by the linked-list method, in which the system is spatially divided into cells interacting only with themselves and with the neighboring cells.[24] Finally, thermally averaged IHC values were obtained by pairwise summation of linearly interpolated values over all Rg–M pairs (interaction cutoff same as for energies) and stored as a rolling average over 30 time steps. All the MD simulations were carried out with a modified version of MOLDY software.[25]

TABLE I. Pair potential data for Rg–M atoms as obtained from CCSD(T) calculations. R_m denotes the potential minimum, ε the potential depth, and parameters A through E of Eq. (1) are in units that result energy in eV. The experimental uncertainties have been included when available.

Rg–M	R_m[Å]	ε[meV]	A	B	C	D	E
Ne–Li	5.38	0.838	76.3656	2.032 15	10 592.2	33.3221	597.356
a	5.82	0.55					
b	5.05	1.11					
Ar–Li	5.01	4.27	305.94	2.044 58	112496	63.0305	4611.33
b	5.27	5.08					
b	4.95	5.31					
Kr–Li	4.94	7.02	375.44	2.007 7	168 969	122.938	6331.83
b	5.18	8.24					
b	4.87	8.55					
b	4.6±0.4	7.9±0.8					
Xe–Li	4.98	10.34	493.694	1.960 37	301 496	203.138	10 108.9
b	5.28	12.6					
b	4.90	13.17					
Ne–Na	5.62	0.731	67.227	1.954 06	15 547.1	37.1298	704.277
a	6.03	0.55					
b	4.2±0.2	1.37±0.06					
c	5.29±0.05	1.00±0.11					
Ar–Na	5.17	4.17	184.428	1.927 81	85 255.8	146.894	2 718.44
b	5.01	5.55					
b	4.8±0.2	5.2±0.3					
c	5.008±0.005	5.17±0.10					
Kr–Na	5.08	6.84	273.115	1.924 82	164 767	206.386	4 800.09
b	4.96	8.68					
b	4.7±0.2	8.6±0.2					
c	4.918±0.004	8.48±0.06					
Xe–Na	5.14	10.1	221.212	1.805 31	158 049	477.07	2 539.25
b	5.06	13.0					
b	4.91±0.08	12.4±0.2					
c	4.95±0.04	14±2					

[a] Calculated. Ref. 12.

[b] Scattering. Ref. 9.

[c] Laser spectroscopic. Ref. 10.

III. RESULTS

A. *Ab initio* calculations

The ground-state Rg–M potential energy curves (PEC) were computed at the CCSD(T) level with cc-pVQZ basis set for M and the augmented Stuttgart basis set for Rg. The latter basis set has been especially tailored for the vdW interactions.[14] Since a similar type of augmented basis set is not available for the alkali metal atoms, we performed a simple comparison between the Pople style basis set 6-311G++(3*df*,3*pd*) and Dunning's cc-pVQZ for Li–Ar pair interaction. Both basis sets perform relatively well and the cc-pVQZ produced only 0.15 meV deeper minimum with 0.04 Å shorter equilibrium distance. By this argument the cc-pVQZ basis set was used throughout this study. The calculated potential parameters along with those derived from the experimental scattering and laser spectroscopic data are shown in Table I. The suitable range for fitting the potentials according to Eq. (1) is ca. 3–20 Å. The ground-state PECs for Rg–Li and Rg–Na are shown in Figs. 1(a) and 1(b), respectively.

The Rg–M IHC curves were obtained at the CCD level and are shown in Figs. 2(a) and 2(b). All IHC curves show a sudden collapse at short distances after which the shift rapidly reaches very large negative values. The obtained parameters (R_m, ε, and R_{collapse}) are given in Table II.

B. MD simulations

Initial lattice geometries for the MD simulations were prepared by introducing alkali metal atoms at interstitial octahedral, substitutional, or multiple substitutional sites with 1, 3, 6, 8, and 12 vacancies around the M atom. For some cases, the time evolution of M atom's IHC and position was followed for longer times than 17.5 ps in order to verify that proper time averages are obtained within the simulation period. During the last 10 fs of simulation, the radial distribution function (RDF) was collected and the number of nearest-neighbor Rg atoms was recorded. The results of the MD simulations along with the experimentally observed IHC shifts for Li and Na are shown in Tables III and IV, respectively. The variation ranges for the tabulated IHC shifts (indicated by±in Tables III and IV) were obtained from the standard deviations of the time-averaged IHC values. When

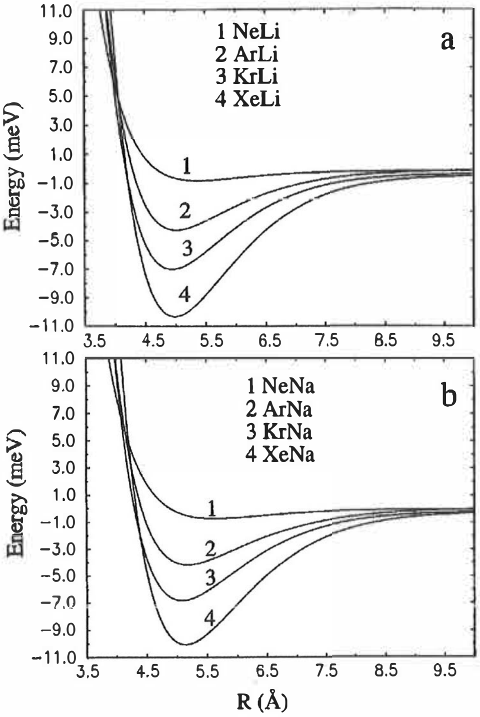

FIG. 1. The CCSD(T) potential energy curves for Rg–M pairs.

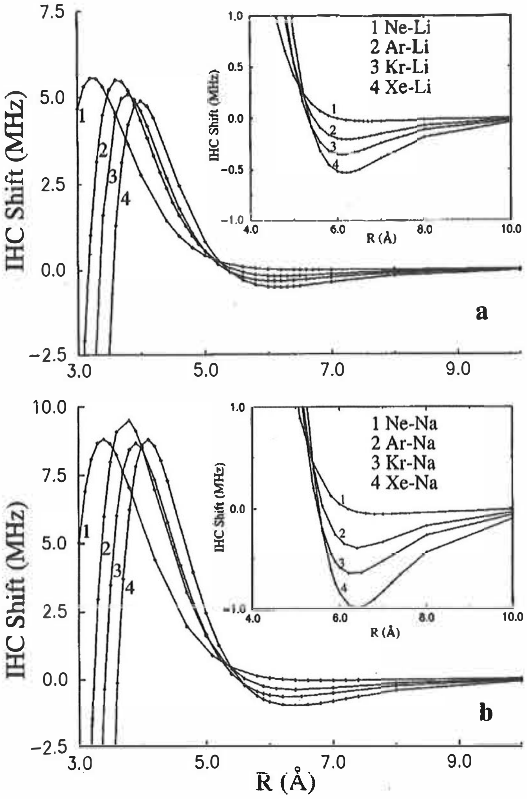

FIG. 2. The calculated IHC constant shifts of alkali metal atoms in Rg–M pairs as obtained by the CCD method.

M atoms were initially placed in interstitial O_h sites in simulation cells corresponding to Ne and Ar lattices, fast lattice relaxation within few ps yielded structures in which the alkali metal impurity was trapped essentially in a substitutional site. This would mean that octahedral trapping is not thermally stable in Ne and Ar even at the lowest temperatures. However, in Kr and Xe the M atoms can be stabilized in interstitial O_h sites. In large cavities corresponding to multiple substitutional sites, the M atoms undergo relatively large amplitude motion which obviously affects the time-averaging processes in those cases. As an example of such extensive in-cage motion, a Li atom trajectory in a multiple substitutional site in Xe is presented in Fig. 3.

IV. DISCUSSION

Taking into account the extreme weakness of the interactions involved in the Rg–M systems, the computationally obtained well depth and equilibrium distance for the Ne–Li dimer are in acceptable agreement with the experimental numbers. The computed well depth is ca. 75% of the experimentally defined value, the absolute error being only ca. 0.3 meV. For comparison, a previous calculation of Czuchaj *et al.*[12] reproduced 50% of the experimental well depth. The neglect of the BSSE effect in Ref. 12 may have, however, caused artificial stabilization and thus better, but erroneous, agreement with the experiment. It was observed in the present work that removal of the BSSE typically reduced the well depth by 20%. It should be noted that the experimental values derived from scattering data may also have rather high error margins due to the relatively low mass of both Ne and Li. A similar comparison may be performed for the Ne–Na pair, for which the computed well depth represents 73% of the experimental 1 meV value. For the heavier Rgs, the previous electronic structure calculations of Laskowski *et al.*[13] were not able to account for the vdW binding due to limitations of their valence basis set, and the work of Saxon *et al.*[13] for Na–Ar yielded excessive binding probably due to limitations of their configuration interaction (CI) procedure. In general, our calculated well depths correspond to ~70%–80% of the experimental values. For all Rg–M pairs the interpretation of the experimental data is not unambiguous and, consequently, the energetic comparisons may not yield a fully correct picture. The present calculation would give

TABLE II. Rg–M IHC curve parameters as obtained from the CCD calculations. R_m denotes the IHC curve minimum, ε the IHC curve depth as compared to zero shift, and R_c the region where collapse of the IHC shift occurs.

	NeLi	ArLi	KrLi	XeLi	NeNa	ArNa	KrNa	XeNa
R_m[Å]	6.7	6.2	6.1	6.2	6.9	6.4	6.3	6.4
ε[Hz]	30	207	349	528	57	400	653	994
R_c[Å]	3.2	3.6	3.8	4.0	3.4	3.8	3.9	4.1

TABLE III. Initial/final trapping site geometries, number of closest neighbor matrix atoms, the closest neighbor distances, and IHC shifts relative to the gas phase values for Rg/Li MD.···denotes an undefined geometry. Experimental values for IHC shifts are included for reference purposes.

Initial/final trapping site geometry	Initial/final # of neighbors	Initial/final Rg–Li distance [Å]	IHC shift [MHz]
In neon			
Subst./Subst.	12/12	3.08/3.70	47±1
Subst.+1 vac./···	11/···	3.08/3.80	40±2
Subst.+3 vac./···	9/···	3.08/3.90	36±1
Subst.+6 vac./···	6/···	3.08/3.80	29±2
Subst.+8 vac./···	4/···	3.08/3.90	25±1
Subst.+12 vac./···	6/···	4.36/4.60	9±1
O_h/···	6/···	2.18/3.80	41±2
In argon			
Subst./Subst.	12/12	3.75/3.90	46±2
[a]	···	···	56
Subst.+1 vac./···	11/···	3.75/3.80	36±1
Subst.+3 vac./···	9/···	3.75/4.10	24±1
Subst.+6 vac./···	6/···	3.75/3.90	15±1
Subst.+8 vac./···	4/···	3.75/4.20	11±2
[b]	···	···	12
[a]	···	···	14
Subst.+12 vac./···	6/···	5.30/4.80	−3±2
[b]	···	···	−7
O_h/···	6/···	2.65/3.20	30±2
In krypton			
Subst./Subst.	12/12	4.03/4.10	36±1
[a]	···	···	44
Subst.+1 vac./···	11/···	4.03/4.20	28±2
Subst.+3 vac./···	9/···	4.03/4.40	13±1
Subst.+6 vac./···	6/···	4.03/4.00	12±2
[b]	···	···	9
Subst.+8 vac./···	4/···	4.03/4.40	3±1
Subst.+12 vac./···	6/···	5.70/4.70	−2±1
[b]	···	···	−7
O_h/O_h	6/6	2.85/3.40	0±3
In xenon			
Subst./Subst.	12/12	4.42/4.40	26±1
Subst.+1 vac./···	11/···	4.42/4.50	21±1
Subst.+3 vac./···	9/···	4.42/4.50	13±3
Subst.+6 vac./···	6/···	4.42/4.60	9±2
Subst.+8 vac./···	4/···	4.42/4.70	9±3
Subst.+12 vac./···	6/···	6.25/4.80	0±2
[b]	···	···	−5
O_h/O_h	6/6	3.13/3.50	−14±12

[a] Experimental. Atoms produced by laser ablation. Ref. 5.

[b] Experimental. Atoms produced thermally (Knudsen oven). Ref. 1.

TABLE IV. Initial/final trapping site geometries, number of closest neighbor matrix atoms, the closest neighbor distances, and IHC shifts relative to the gas phase values for Rg/Na MD. ···denotes an undefined geometry. Experimental values for IHC shifts are included for reference purposes.

Initial/final trapping site geometry	Initial/final # of neighbors	Initial/final Rg–Na distance [Å]	IHC shift [MHz]
In neon			
Subst./Subst.	12/12	3.08/3.80	95±4
Subst.+1 vac./···	11/···	3.08/3.80	83±3
Subst.+3 vac./···	9/···	3.08/3.90	77±3
Subst.+6 vac./···	6/···	3.08/3.90	60±4
Subst.+8 vac./···	4/···	3.08/4.10	50±2
Subst.+12 vac./···	6/···	4.36/4.60	24±1
O_h/···	6/12	2.18/3.90	85±4
In argon			
Subst./Subst.	12/12	3.75/4.00	87±2
Subst.+1 vac./···	11/···	3.75/3.90	69±2
Subst.+3 vac./···	9/···	3.75/3.70	49±3
Subst.+6 vac./···	6/···	3.75/4.10	32±1
Subst.+8 vac./···	4/···	3.75/4.20	24±3
Subst.+12 vac./···	6/···	5.30/4.80	−11±1
O_h/···	6/12	2.65/3.60	79±2
In krypton			
Subst./Subst.	12/12	4.03/4.10	68±1
[a]	···	···	115
Subst.+1 vac./···	11/···	4.03/4.10	53±3
Subst.+3 vac./···	9/···	4.03/3.90	27±1
Subst.+6 vac./···	6/···	4.03/4.00	21±1
[b]	···	···	11
Subst.+8 vac./···	4/···	4.03/4.60	7±1
Subst.+12 vac./···	6/···	5.70/4.60	−10±7
[b]	···	···	−14
O_h/O_h	6/6	2.85/3.70	20±6
In xenon			
Subst./Subst.	12/12	4.42/4.50	52±2
[a]	···	···	97
Subst.+1 vac./···	11/···	4.42/4.50	43±2
Subst.+3 vac./···	9/···	4.42/4.30	12±2
Subst.+6 vac./···	6/···	4.42/4.50	15±2
Subst.+8 vac./···	4/···	4.42/4.50	−4±1
Subst.+12 vac./···	6/···	6.25/5.10	−7±4
[b]	···	···	−12
O_h/O_h	6/6	3.13/3.70	−5±21

[a] Experimental. Atoms produced by laser ablation. Ref. 5.

[b] Experimental. Atoms produced thermally (Knudsen oven). Ref. 5.

some general guidelines for analysis of such data. The main errors originate from the partial treatment of electron correlation and incompleteness of the applied basis sets. Nevertheless, the obtained level of agreement with the experimental data convince us that the computed pair potentials are of sufficient quality to be utilized in the subsequent MD simulations of M/Rg lattices.

A common feature for the computed PECs is that they follow very closely the form of the potential function defined in Eq. (1). The adequacy of a single analytic potential function simplifies the construction of the multidimensional force field for the MD simulations. However, extending the least-squares fitting to much shorter internuclear distances than 3 Å causes Eq. (1) to fail near the vdW region. On the other hand, ignoring data points at internuclear distances less than 3 Å yields potential fits of insufficient quality in this region. It is particularly important for theoretical treatment of tight trapping geometries that the fitted potentials, and IHC curves, behave correctly over the entire distance range. A straightforward approach for dealing with IHC curves was to use the primary numerical data and perform linear interpolation between the calculated data points. The obvious shortcoming of this method is that the obtained results cannot be conveniently expressed in any parametrized form. A general feature of the IHC curves is that they all reach a minimum at internuclear distances about 1.3 Å longer than the corresponding PECs. The shape of the IHC curves closely resembles the PECs except for the rapid turnover near 3–4 Å,

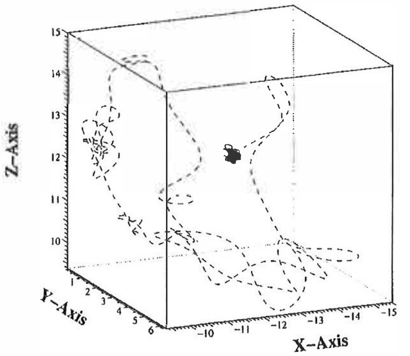

FIG. 3. A representative example of atomic mobility in different lattice surroundings. Solid line: Li atom trajectory in a substitutional site of Xe. Dashed line: Li atom trajectory in Xe where 12 vacancies have been introduced. The simulation trajectory in perfect lattice is well localized within ca. (0.4×0.4×0.4) Å^3 volume, whereas the 12 vacancies yield sampling of at least (6×6×6) Å^3 volume with the same simulation time of 20 ps.

where the IHC shift collapses towards large negative values. This collapse indicates severe shielding of the unpaired electron from the M nucleus. The collapse behavior of the IHC constant has been predicted in previous studies on Rg–H systems,[14,25,26] but not, according to our knowledge, verified experimentally.

There are several obvious approximations involved in obtaining the matrix shifts for IHC of M atoms isolated in solid Rg. The first approximation is connected to the electronic structure calculations as stated above. For the classical MD simulations, the success (or failure) depends crucially on the force field on which the atoms move. In this study, we have constructed the force field additively from pair interaction of the atoms. A general estimate is, however, that several percent of the total energy of a real Ar lattice consists of a higher order than two-body interactions. Furthermore, our simulations rely on classical mechanics with neglect of the zero-point energies and assumption of continuous energy spectrum. These approximations are not expected to be severe for the heavier atoms but may have some implications for systems containing Ne or Li. The last approximation concerns the pairwise additivity of the IHC, i.e., how well can the total IHC shift be obtained by summation over contributions of individual Rg–M pairs. As discussed in Ref. 14, the magnitude of the many-body contributions on the total IHC shifts is not currently quantified. A relatively well-grounded estimate would be that these effects are of the same order as the many-body contributions to the energy. This estimate is based on the close connection between the pair potentials and the IHC curves as first shown by Adrian.[8] The three-body and higher-order contributions for IHC shifts are expected to become larger at small internuclear distances. Despite the approximations involved in the current method, our previous investigation on trapping of atomic hydrogen in Rg matrices showed, indeed, that EPR resonances due to different trapping sites can be unambiguously identified by computational methods. More complex atomic systems will ultimately reveal the reliability of the current quantum-classical approach.

In order to characterize the alkali metal atom trapping sites in Rg matrices, various initial trapping conditions were explored. In Ne ($T=5$ K) and Ar matrices ($T=15$ K) the interstitial O_h site was not thermally stable and relaxed within a few ps into geometries resembling substitutional sites. On the contrary, the O_h sites provide thermally stable deep traps for Li and Na in Kr and Xe matrices. As can be seen from Tables III and IV, the interstitial O_h site is very tight in these lattices and the M atom causes considerable expansion of the original cavity. Due to the tightness of the trapping site, the MD trajectories sample internuclear distances near the point where the sudden collapse of the IHC curves occur. This effect is pronounced in Xe, where the IHC shifts are negative and have large standard deviations. By the usually applied sample preparation methods, Knudsen oven source and laser ablation, this trapping site probably cannot be accessed since both methods deposit M as atoms into the matrix. The situation can be compared with atomic hydrogen which traps exclusively in pure substitutional sites upon atom beam deposition, whereas *in situ* photolysis of hydrogen-containing precursor molecules produces both interstitial O_h and substitutional trapping sites. Thus, in principle, it should be possible to reach the IHC shift collapse region in the experiments when a suitable M atom generation scheme is chosen.

The pure substitutional sites are thermally stable at applied temperatures for all Rg/M combinations and exhibit large positive IHC shifts. For Ne/M matrices no experimental data are available, but the MD simulations predict that the substitutional sites should exist and have positive IHC shifts of ca. 47 MHz with respect to the gas phase value. In {Ar and Kr}/Li the calculated results are close to the IHC shifts obtained in the laser ablation experiments, the relative difference being 18% for both cases. Thus, it can be concluded that sample preparation by laser ablation yields pure substitutional trapping of Li atoms in Ar and Kr matrices. Unfortunately, due to the experimental problems with Xe/Li,[5] no comparison can be made for this combination. Due to spectral congestion in Ar/Na EPR data, the experimental parameters are not available and comparison is afforded for Kr and Xe only. If comparison is made against the IHC shifts of laser ablated samples, the relative differences are ca. 40%. Hence, it appears that for Rg/Na only a qualitative agreement with the experiment can be obtained.

In order to characterize the trapping site structures of Rg/M solids being prepared by a thermal Knudsen oven source, we introduced an increasing number of lattice vacancies around the trapping center of the metal. Experimental Knudsen oven data exist for all Rg/M combinations except for Ne, and in most cases EPR spectra indicate trapping in several nonequivalent lattice sites. In Li-doped Ar, two distinct trapping sites are observed by EPR and the data in Table III tentatively assign these signals as originating from 8 and 12 vacancy cases. For Kr/Li the corresponding number of vacancies is 6 and 12, whereas for Xe/Li the number of vacancies is at least 12. In principle, for Xe/Li the assignment to interstitial O_h site would also be possible although highly unlikely as the results for Rg progression are followed from Ar to Xe. In conclusion, it can be asserted that the alkali metal atoms generated from a Knudsen oven source are trapped in sites associated with more than six neighboring vacancies. By following the M atom trajectories during the MD simulation, the rather extensive mobility within this extended cage is clearly seen. In fact, such in-cage motion has been deducted from analysis of EPR line broadening in Ar/Li solids.[27]

The applied computational method performs well with Rg/Li lattices but does much worse with Na doping. The error in Rg/Na most likely originates from the *ab initio* calculation of the pair potential and/or the IHC curves. For both cases, the calculations could have been enhanced by augmenting the M atom basis sets with suitable diffuse Gaussians. At the present, such augmentation is not available for the Dunning basis sets. A possible error related to the calculations concerning multiple substitutional sites is obviously connected to the relatively short simulation times in MD, which may not fully account for the in-cage motion of the alkali metal atom (see Fig. 3). Since the time scale for this motion may in fact be comparable to the EPR time scale, it would require excessively long simulation times to fully account for such phenomena.

V. CONCLUSIONS

In this study we have extended the methodology developed in Ref. 14 to a more complex system consisting of alkali metal atom, lattice vacancies, and rare gas atoms. The present results give further support for the applicability of the quantum-classical simulation approach for obtaining IHC shifts for matrix isolated atoms. The major obstacle in obtaining sufficient accuracy with the present method is the accurate evaluation of the potential energy and IHC curves by high-quality electronic structure methods. In this respect, the coupled-cluster methods seem accurate enough for Li, whereas more sophisticated treatments would be essential for Na in order to improve the computed IHC shifts. Despite the lower accuracy of the simulation results for Na, the site assignments can still be performed with confidence. According to our calculations, laser ablated atoms occupy single substitutional sites, whereas thermally generated atoms are trapped in large multiple substitutional sites with more than six vacancies around the alkali metal atom.

ACKNOWLEDGMENT

Financial support from the Academy of Finland is greatly acknowledged.

[1] C. K. Jen, V. A. Bowers, E. L. Cochran, and S. N. Foner, Phys. Rev. **126**, 1749 (1962).

[2] L. Andrews and G. C. Pimentel, J. Chem. Phys. **47**, 2905 (1967).

[3] J. P. Goldsborough and T. R. Koehler, Phys. Rev. **133**, 135 (1964).

[4] L. C. Balling, M. D. Havey, and J. F. Dawson, J. Chem. Phys. **69**, 1670 (1978).

[5] K. Vaskonen, J. Eloranta, and H. Kunttu, Chem. Phys. Lett. **310**, 245 (1999).

[6] J. H. Ammeter and D. C. Schlosnagle, J. Chem. Phys. **59**, 4784 (1973).

[7] M. E. Fajardo, P. G. Garrick, and J. W. Kenney, III, J. Chem. Phys. **94**, 5812 (1991); M. E. Fajardo, *ibid.* **98**, 110 (1993); S. Tam and M. E. Fajardo, *ibid.* **99**, 854 (1993); D. C. Silverman and M. E. Fajardo, *ibid.* **106**, 8964 (1997).

[8] J. F. Adrian, J. Chem. Phys. **32**, 972 (1960).

[9] E. W. Rothe, P. K. Rol, and R. B. Bernstein, Phys. Rev. **130**, 2333 (1963); U. Buck and H. Pauly, Z. Phys. **208**, 390 (1968); R. Düren, G. P. Raabe, and Ch. Schlier, *ibid.* **214**, 410 (1968); R. Düren, A. Frick, and Ch. Schlier, J. Phys. B **5**, 1744 (1972).

[10] W. P. Lapatovich, R. Ahmad-Bitar, P. E. Moskowitz, I. Renhorn, R. A. Gottscho, and D. E. Pritchard, J. Chem. Phys. **73**, 5419 (1980); G. Aepfelbach, A. Nunnemann, and D. Zimmermann, Chem. Phys. Lett. **96**, 311 (1983); R. Brühl, J. Kapetanakis, and D. Zimmermann, J. Chem. Phys. **94**, 5865 (1991); P. Baumann, D. Zimmermann, and R. Brühl, J. Mol. Spectrosc. **155**, 277 (1992).

[11] D. Cvetko, A. Lausi, A. Morgante, F. Tommasini, P. Cortona, and M. G. Dondi, J. Chem. Phys. **100**, 2052 (1994); U. Kleinekathöfer, K. T. Tang, J. P. Toennies, and C. L. Yiu, Chem. Phys. Lett. **249**, 257 (1996); S. H. Patil, J. Chem. Phys. **94**, 8089 (1991).

[12] E. Czuchaj, F. Rebentrost, H. Stoll, and H. Preuss, Chem. Phys. **136**, 79 (1989); M. Jungen and V. Staemmler, J. Phys. B **21**, 463 (1988).

[13] B. C. Laskowski, S. R. Langhoff, and J. R. Stallcop, J. Chem. Phys. **75**, 815 (1981); R. P. Saxon, R. E. Olson, and B. Liu, *ibid.* **67**, 2692 (1977).

[14] T. Kiljunen, J. Eloranta, and H. Kunttu, J. Chem. Phys. **110**, 11814 (1999).

[15] K. Raghavachari, G. W. Trucks, J. A. Pople, and M. Head-Gordon, Chem. Phys. Lett. **157**, 479 (1989).

[16] D. E. Woon and T. H. Dunning, Jr. (unpublished results).

[17] A. Nicklass, M. Dolg, H. Stoll, and H. Preuss, J. Chem. Phys. **102**, 8942 (1995).

[18] S. F. Boys and F. Bernardi, Mol. Phys. **19**, 553 (1970).

[19] GAUSSIAN 98, Revision A.3, M. J. Frisch, G. W. Trucks, H. B. Schlegel, G. E. Scuseria, M. A. Robb, J. R. Cheeseman, V. G. Zakrzewski, J. A. Montgomery, Jr., R. E. Stratmann, J. C. Burant, S. Dapprich, J. M. Millam, A. D. Daniels, K. N. Kudin, M. C. Strain, O. Farkas, J. Tomasi, V. Barone, M. Cossi, R. Cammi, B. Mennucci, C. Pomelli, C. Adamo, S. Clifford, J. Ochterski, G. A. Petersson, P. Y. Ayala, Q. Cui, K. Morokuma, D. K. Malick, A. D. Rabuck, K. Raghavachari, J. B. Foresman, J. Cioslowski, J. V. Ortiz, B. B. Stefanov, G. Liu, A. Liashenko, P. Piskorz, I. Komaromi, R. Gomperts, R. L. Martin, D. J. Fox, T. Keith, M. A. Al-Laham, C. Y. Peng, A. Nanayakkara, M. Challacombe, P. M. W. Gill, B. Johnson, W. Chen, M. W. Wong, J. L. Andres, C. Gonzalez, M. Head-Gordon, E. S. Replogle, and J. A. Pople, Gaussian, Inc., Pittsburgh, PA, 1998.

[20] R. McWeeny, *Methods of Molecular Quantum Mechanics* (Academic, London, 1992).

[21] G. C. Maitland, M. Rigby, E. B. Smith, and W. A. Wakeham, *Intermolecular Forces: Their Origin and Determination* (Oxford Science, Oxford, 1987).

[22] M. P. Allen and D. J. Tildesley, *Computer Simulations of Liquids* (Clarendon, Oxford, 1987).

[23] D. Beeman, J. Comput. Phys. **20**, 130 (1976); K. Refson, Physica B **131**, 256 (1985).

[24] B. Quentrec and C. Brot, J. Comput. Phys. **13**, 430 (1975).

[25] K. Refson, MOLDY *User's Manual* (Oxford, 1998).

[26] W. Meyer and L. Frommhold, Theor. Chim. Acta **88**, 201 (1994).

[27] A. Schrimpf, R. Rosendahl, T. Bornemann, H.-J. Stöckmann, F. Faller, and J. Manceron, J. Chem. Phys. **96**, 7992 (1992).

PAPER III

https://doi.org/10.1063/1.481345

Reprinted with permission from T. Kiljunen et al, "Electronic structure and short-range recombination dynamics of S_2 in solid argon," *The Journal of Chemical Physics* **112**, 2000, pp. 7475–7486.

JOURNAL OF CHEMICAL PHYSICS VOLUME 112, NUMBER 17 1 MAY 2000

Electronic structure and short-range recombination dynamics of S_2 in solid argon

Toni Kiljunen,[a] Jussi Eloranta, and Henrik Kunttu
Department of Chemistry, University of Jyväskylä, P. O. Box 35, FIN-40351 Jyväskylä, Finland

Leonid Khriachtchev, Mika Pettersson, and Markku Räsänen
Laboratory of Physical Chemistry, P. O. Box 55, FIN-00014, University of Helsinki, Finland

(Received 29 November 1999; accepted 10 February 2000)

Potential energy curves for 13 lowest electronic states of S_2 and 6 lowest states of ArS are computed at the MRCI level utilizing the CASSCF orbitals. The electronic structure of S_2 is described by the correlation consistent cc-pVQZ basis set, whereas for ArS the augmented version of this basis is combined with ten electron-core pseudopotential basis set for S and Ar, respectively. Thermal and shock wave induced recombination dynamics of sulfur atoms trapped in Ar lattice are investigated by classical Molecular Dynamics simulations. It is observed that atoms separated by nearest neighbor distance of the lattice do immediately recombine even at 1 K with no thermal activation. While separated by one lattice constant, the S atoms stay stable up to 80 K and no recombination is observed in the classical trajectories. Consequently, the simulation was able to reproduce the experimental S+S glow curve only by lowering the reaction barrier by introducing lattice vacancies in the four atom plane separating the S–S pair. Local 1.1 eV kinetic excitation of a lattice atom next to the trapped S–S pair or artificial shock waves initiated by more distant excitation at 2 eV or more greatly enhanced the probability for recombination. Nonradiative $^1D-^3P$ relaxation of sulfur provides a mechanism for such phonon emission and is discussed as a potential reason for the observed photoinduced recombination in low temperature Ar matrix. *© 2000 American Institute of Physics.* [S0021-9606(00)30317-8]

I. INTRODUCTION

Trapping of reactive species such as atoms, radicals, or chemical intermediates and their subsequent recombination upon controlled annealing are issues of key importance for chemical energy storage in cryogenic solids.[1] In fact, the obvious need for deeper understanding of these fundamental questions initiated active developments in experimental techniques which are now combined under the title ''matrix isolation'' (MI). Due to their conceptual simplicity, rare gas (Rg) matrices or crystals doped with atomic or small molecular impurities provide a nearly ideal prototype for dynamics such as cage-effect, mobility, and recombination which are all controlled by complex multi-body scattering events. Moreover, microscopic description of the observed dynamics and spectroscopy at the first-principles level is more easily attained in atomic solids of well-defined structures than in liquid.

The present work is a continuation to the previous investigations by Khriachtchev and co-workers on photophysics and chemistry of fragments photogenerated from H_2S and H_2S_2 precursor molecules.[2,3] The low temperature thermoluminescence of sulfur observed in photolysed H_2S_2/Ar matrix was ascribed to short-range mobility of atoms separated by one Ar lattice constant.[3] Thermal activation of this quasistable configuration by annealing at 10–15 K yields strong luminescence due to $B'' \, ^3\Pi_u - X \, ^3\Sigma_g^-$ transition of S_2 molecule. Higher annealing temperatures revealed an additional emission, which was interpreted to originate from more extensive mobility of thermally activated atoms. Quite interestingly, while photoexcited at 456 nm, the S atoms were observed to undergo efficient recombination already at 7.5 K. A tentative explanation for this behavior was based on activation by lattice phonons created in the photoexcitation.[3]

In order to provide more rigorous insights into the observed atomic mobility and thermoluminescence spectra, classical Molecular Dynamics (MD) simulations based on *ab initio* potential energy curves (PEC) for the S–S and S–Ar pairs are carried out for Ar lattice with two lattice points occupied by S atoms. A similar approach has recently shown success in describing cage trapping geometry and isotropic hyperfine properties of hydrogen and alkali metal atoms in rare gas matrices.[4] The present calculations aim at providing microscopic description of both thermal and photoinduced recombination observed in the experiments, and simultaneously to further extend the applicability of classical MD simulations in studies of atomic and molecular properties in condensed media.

The electronic structure of diatomic sulfur has previously been subject to theoretical interest. Swope *et al.*[5] calculated 13 lowest bound electronic states with a moderate configuration interaction (CI) method. The B and B'' states relevant to optical spectroscopy in the visible region have been studied by accurate multireference CI (MRCI) methods: Wheeler *et al.*[6] studied predissociation of the B state and computed some of the repulsive states as well, whereas

---

[a] Author to whom correspondence should be addressed. Electronic mail: kiljunen@epr.chem.jyu.fi

Pradhan and Partridge[7] reported oscillator strengths, transition probabilities, and radiative lifetimes for the $B-X$ and $B''-X$ systems. Since our interest is strongly on the $S+S \rightarrow S_2$ recombination reaction in Ar lattice, which necessitates accurate description of the van der Waals region of the S–S and Ar–S pairs, the PECs for various electronic states are re-evaluated at a sufficient level of theory. Along with the PECs, the gas phase emission spectra of S_2 was calculated for those transitions, which are observed under MI conditions. According to our knowledge no previous calculations exist for excited states of ArS. Electronic properties of rare gas oxides, RgO, have been rather extensively studied by several authors some time ago,[8] and more recently a renewed attention has been paid to electronic states of XeO and XeS.[9] Finally, Nemukhin *et al.*[10] computed six valence states and three ion-pair states of KrS as input for a diatomics-in-molecules (DIM) potential energy surface.

II. METHODS OF CALCULATION

The quantum chemical calculations comprise the treatment of 13 lowest lying bound singlet and triplet electronic states of diatomic sulfur (S_2) and six lowest valence states of argon sulfide (ArS). The correlation consistent basis set (cc-pVQZ, or vqz for short) of Woon and Dunning[11] was used in the S_2 calculations. For ArS, the augmented version (avqz) of the cc-pVQZ basis set and relativistic 10-electron-core pseudopotential basis set developed by the Stuttgart group[12] were used for sulfur and argon, respectively. The calculations were performed at the MRCI[13] (with internally contracted CI) level utilizing complete active space self-consistent field (CASSCF)[14] orbitals as implemented in the MOLPRO suite of codes.[15] The active space for S_2 consists of full valence space: 12 electrons distributed into eight orbitals ($4\text{-}5\sigma_g$, $4\text{-}5\sigma_u$, $2\pi_u$, and $2\pi_g$), extended with the $3\pi_u$ orbital as found necessary for proper treatment of the transition moments.[7] Moreover, inclusion of $3\pi_u$ has a significant contribution (ca. 4%) in the MRCI binding energy of the ground state. The described representation yields 2588 CAS configuration state functions and 646 530 configurations for the ground state in the CI stage after contraction. The potential energy curves for S_2 were constructed from 29 single state MRCI calculations at internuclear separations from 1.4 to 20 Å. In cases where the state is not the lowest energy one in the particular irreducible representation, the state-averaged (SA) CASSCF orbitals were used. ArS was treated similarly with 14 correlated electrons. The PECs for ArS were obtained from 17 single point calculations at internuclear separations between 1.8 and 6.5 Å.

For both S_2 and ArS the free atom asymptotes correlating to ground or excited state sulfur atoms were scaled to the experimentally determined ${}^3P_2-{}^1D_2$ and ${}^3P_2-{}^1S_0$ splittings of 9239.0 cm^{-1} and 22 181.4 cm^{-1}, respectively.[16] Size extensivity was considered routinely by performing the multireference analogue of the Davidson correction for the higher excitations,[17] denoted by MRCI+Q in the results. In addition, multireference averaged coupled-pair functional calculation, MR-ACPF,[18] was performed for some of the states.

The dipole transition moments were obtained for the $B\,{}^3\Sigma_u^- - X\,{}^3\Sigma_g^-$ and $B''\,{}^3\Pi_u - X\,{}^3\Sigma_g^-$ systems of S_2 using SA-CASSCF orbitals in MRCI at 20 internuclear distances between 1.4 and 3.6 Å. The *ab initio* potentials and transition moments were further utilized for producing thermoluminescence spectra. For this purpose, the *X*, *B*, and B'' state potential data were fitted according to polynomial-exponential expansion given in Ref. 7. The vibrational Schrödinger equation was then solved numerically in these potentials by the finite difference approximation method.[19] The eigenvalues and eigenvectors of the resulting matrix were solved by the NAG library routine F02EBF.[20] The transition intensities were obtained by evaluating the squares of the overlap integrals between the $v'=0$ vibrational level of the excited state and the vibronic manifold of the ground state. The degeneracy of the B'' state (π_x, π_y) was taken into account by multiplying the intensities by a factor of 2. The spectroscopic constants for all states were determined by least squares fitting of the six lowest vibrational levels into an expression yielding ω_e and $\omega_e x_e$.

Molecular dynamics simulations were performed in microcanonical (NVE) ensemble with a modified version of MOLDY software.[21] Initial kinetic energies for atoms were picked from the Maxwell–Boltzmann distribution at the desired temperature and standard kinetic energy scaling was applied for regulating the system temperature. The simulation temperature ranged from 5 to 50 K. MOLDY uses a modified Beeman algorithm for integration of the equations of motion.[22] In this work an integration time-step of 0.5 fs was used with a typical total simulation time of 20 ps (1 ps for thermalization and 19 ps for simulation). In order to decrease the computational demand of the simulations, the linked-list method and potential interaction cutoff of 8 Å were used.[23] The remaining missing long-range part was compensated by standard procedures.[24] The simulation cell is a face centered cubic (fcc) lattice consisting of 1370 argon atoms and two impurity sulfur atoms. Periodic boundary conditions were applied for the simulation cube of 37.1 Å×37.1 Å×37.1 Å. The MD simulation is purely classical with a potential energy surface pair-wisely constructed from the *ab initio* calculated S–S and Ar–S interactions and experimentally determined Ar–Ar interaction.[25] For parametrization of the van der Waals bound complexes Ar–S and Ar–Ar, the purpose is to present the pair interaction in terms of a suitable analytic formula from which the force field for atomic motion can be conveniently evaluated. For this we use a modified Buckingham potential augmented with an additional Lennard–Jones type R^{-12} term for repulsion:

$$\phi(R) = Ae^{-BR} + \frac{C}{R^{12}} - \frac{D}{R^6} - \frac{E}{R^8}. \tag{1}$$

The MD algorithm of MOLDY was modified in order to allow kinetic excitation of a selected lattice atom and therefore to bypass the NVE conditions momentarily. The magnitude of this excess momentum and its direction were varied to generate various types of shock waves into the lattice. A similar approach for studying shock wave propagation in argon lattice has been employed by Cenian *et al.*[26] who demonstrated that once initiated by a local excitation, the shock waves

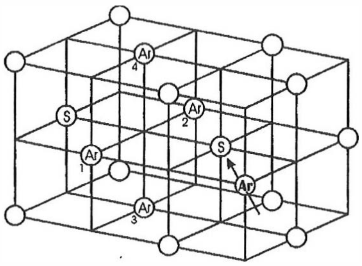

FIG. 1. A portion of an fcc argon lattice showing the two impurity sulfur atoms at their quasistable configuration. The argon atoms marked explicitly induce the cage barrier preventing the S+S recombination. The reactive direction of shock wave propagation is indicated by an arrow.

propagate along the ⟨110⟩ crystallographic direction defined by the nearest neighbor lattice atoms. Therefore, we choose the excited atom from the ⟨110⟩ plane containing one of the S atoms and direct the excitation in a way that promotes S+S recombination (see Fig. 1).

III. RESULTS

A. PECs of S_2

Short-range recombination reaction, as proposed in Ref. 3, would involve a capture radius comparable with the lattice constant of the host matrix. Thus simulation of such reaction is particularly prone for accurate description of atom–atom forces at long distances near the S–S dissociation region. In this respect, potentials constructed from the parameters available in the literature[27] are not adequate for the simulation of recombination dynamics, which takes place from essentially zero interaction region. Most importantly, when calculating the static cage barrier caused by the lattice atoms, it is the region between 3 and 5 Å that contributes most. As observed in Fig. 2, most of the PECs correlating to the ground state atoms behave relatively similarly in this region. Consequently, a branching ratio near unity can be expected between the ground and excited state recombination paths. Exceptions are the $B''\,{}^3\Pi_u$ state possessing a dipole allowed transition to the ground state, and the pre-dissociative ${}^1\Pi_u$ state. In addition to these, the bound high-spin ${}^5\Pi_g$ state has a well depth of 0.355 eV at 2.655 Å and thus possesses strongest interaction at large R (not shown in Fig. 2). Neglect of the spin-orbit interaction in the calculations should lead to a situation where PECs correlating with a common atomic limit approach the same energy at long distances. In the present case the computed asymptotes at 20 Å lie within 76.6, 76.7, and 18.1 cm^{-1} for the $S({}^3P+{}^3P)$, $S({}^3P+{}^1D)$, and $S({}^3P+{}^1S)$ separated atom limits, respectively. These numbers place the mean excitation energies for the $S({}^3P+{}^1D)$ and $S({}^3P+{}^1S)$ limits at 9203.1 cm^{-1} and 18 427.8 cm^{-1}, respectively. As stated, the vdW region is most important for the simulation. Thus to avoid the obvious error arising from fitting the entire interatomic range with a single analytic function, the MD simulations were carried out with a more accurate potential fit constrained to distances from 2.5 Å. Within this region no deviation between the calculated points and the fit is observed in the meV scale. The threshold distance of 2.5 Å was used as the criteria for S+S recombination.

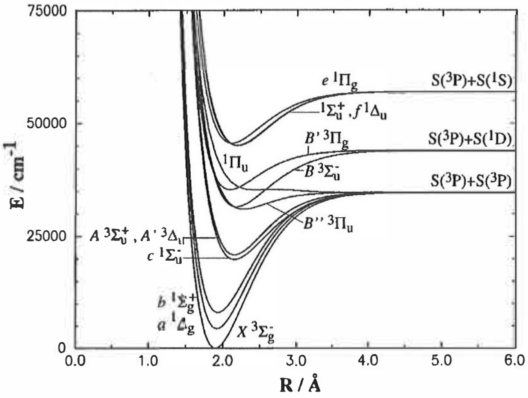

FIG. 2. Calculated potential energy curves for the bound electronic states of S_2 molecule arising from the ${}^3P$, ${}^1D$, and ${}^1S$ separated atom limits. The curves have been scaled to experimental ${}^3P_2-{}^1D_2$ and ${}^3P_2-{}^1S_0$ splittings.

Table I collects the T_0 values and potential parameters for the computed PECs. A comparison is made against the values reported by Swope *et al.*[5] who applied the Davidson correction once at the equilibrium distances. It should be noted that the limited internuclear range and single reference nature of the treatment in Ref. 5 do not afford comparison of $\omega_e x_e$ and D_e values. The computed zero-point energies (ZPE) for the X, B'', and B states of 359.8, 170.0, and 215.5 cm^{-1} are in acceptable agreement with the previous numbers of 359.2, 161.6, and 216.4 cm^{-1} by Pradhan and Partridge.[7] The electronic origins T_e for the B'', and B states are 3.832 eV and 3.909 eV, respectively.

B. Electronic transitions

The calculated electric dipole transition moments are given in Table II. The Fermi golden rule treatment yields a conversion from transition moment to transition probability:

$$W_{fi}=\frac{32}{3}\pi^3 c\alpha(5.29\times10^{-11})^2\times10^6\tilde{\nu}^3|R|^2\frac{1}{s}, \tag{2}$$

where c is the velocity of light, α is the fine-structure constant, $\tilde{\nu}$ is the transition energy in cm^{-1}, and $|R|$ is the vibronically averaged transition moment in atomic units as explained in Sec. II. The numerical constants convert W_{fi} to s^{-1}. The transition probabilities of the relaxed ($v'=0$) emission as obtained from Eq. (2) are given in Table III for $B-X$ and $B''-X$ systems up to ground state $v''=24$ level. The transition probability vanishes for higher vibrational levels. The computed stick spectra are shown in Fig. 3. The maxima of the two emission systems are located at 380 nm ($B-X$) and 445 nm ($B''-X$), and their 0–0 transitions are at 316 nm and 318 nm, respectively. The radiative lifetime of a transition is given as the inverse of the total transition probability, that is

$$\tau=\left(\sum W_{fi}\right)^{-1}, \tag{3}$$

TABLE I. Relative energies (T_0) and potential parameters of the 13 electronic states. The values in parentheses are those calculated by Swope *et al.* in Ref. 5 from whence the experimental reference values (in square brackets) are also taken.

State	T_0 [cm^{-1}]	R_e [Å]	D_e [eV]	ω_e [cm^{-1}]	$\omega_e x_e$ [cm^{-1}]
$e\ ^1\Pi_g$	45 355	2.116	1.406	449.7	3.83
	(43 300)	(2.143)		(430)	
$^1\Sigma_u^+$	44 808	2.179	1.473	436.1	3.18
	(53 800)	(2.128)		(500)	
	[45 100]	[–]		[428.5]	
$f\ ^1\Delta_u$	44 810	2.174	1.473	440.1	3.44
	(44 100)	(2.138)		(500)	
	[41 600]	[2.156]		[438.3]	
$^1\Pi_u$	35 270[a]	2.45[a]			
	(37 600)	(2.243)			
$B'\ ^3\Pi_g$	35 141	2.095	1.067	439.7	4.94
	(35 300)	(2.106)		(450)	
	[35 300]	[2.08]		[~500]	
$B\ ^3\Sigma_u^-$	31 388	2.185	1.532	432.5	3.04
	(32 500)	(2.142)		(490)	
	[31 689]	[2.168]		[434.0]	
	31 672[b]	2.171[c]	1.585±0.04[c]	434.0[c]	2.54[c]
		2.170[d]	1.608±0.008[d]	434.0[d]	2.75[d]
$B''\ ^3\Pi_u$	30 717	2.291	0.464	343.1	6.05
	(32 100)	(2.219)		(430)	
	[≤31 700]	[<2.28]		[–]	
	31 069[b]	2.281[c]	0.516±0.04[c]	325.4[c]	4.52[c]
		2.302[d]	0.5577±0.010[d]	335.2[d]	4.5[d]
$A\ ^3\Sigma_u^+$	20 842	2.166	1.694	479.8	2.55
	(19 700)	(2.176)		(580)	
	[21971]	[2.15]		[488.2]	
$A'\ ^3\Delta$	20 866	2.166	1.694	480.1	2.56
	(19 100)	(2.168)		(480)	
	[20 974]	[2.146]		[488.2]	
$c\ ^1\Sigma_u^-$	19 756	2.159	1.832	486.0	3.16
	(17 900)	(2.160)		(489)	
	[20 000]	[–]		[–]	
$b\ ^1\Sigma_g^+$	8001	1.931	3.300	657.6	3.31
	(8960)	(1.914)		(732)	
	[8500]	[–]		[700.8]	
$a\ ^1\Delta$	4458	1.918	3.741	684.9	3.00
	(4820)	(1.907)		(746)	
	[4700]	[1.898]		[702.4]	
$X\ ^3\Sigma_g^-$	0.0	1.901	4.296	721.5	3.96
		(1.900)		(760)	
		1.896[c]	4.392±0.03[c]	719.8[c]	2.81[c]
		1.889[d]	4.410±0.008[d]	725.7[d]	2.844[d]

[a] The potential shows a shallow minimum at 2.45 Å and a small maximum at 2.65 Å which the potential fit was not able to produce. The value 35 270 cm^{-1} is T_e, defined as a difference of the potential curve minima.

[b] Deperturbation analysis data of Green and Western in Ref. 30.

[c] Calculated (complete basis set limit) values of Pradhan and Partridge in Ref. 7.

[d] Collected experimental data as cited in Ref. 7.

where the summation is over the 25 tabulated values for transition probability. This yields radiative lifetimes of 35.2 ns and 6.25 μs for the $B(v'=0)$ and $B''(v'=0)$ states, respectively.

C. PECs of Ar–S

The computed PECs of ArS derived from the ^3P, ^1D, and ^1S atomic states of sulfur are shown in Fig. 4. As expected, the similarity with the Rg–O systems is obvious.[8] Particularly, the nearly flat interaction potential of the lowest $^1\Sigma^+$ state at internuclear distances down to 2 Å is very similar to Ar–O, and may contribute to the observed recombination dynamics by impulsive nonradiative energy transfer. In effect, populating the $^1\Sigma^+$ state either by direct atomic excitation of $^3P \rightarrow {}^1D$ sulfur or by relaxation of the excited ^1S provides a mechanism in which, due to spin-orbit coupling, the $^3\Sigma^-/^3\Pi$ surfaces could be populated at their repulsive walls. The kinetic energy release in this collisional quenching is ~1 eV and can be considered as a possible source for shock wave generation and, consequently, promote S_2 recombination. This is in accord with the experimental observation that excitation of the sample by visible light induces recombinant emission of S_2.[3]

Due to its nonspherical ground state, dynamics of S atom trapped in an Ar matrix is dictated by anisotropic many-body

TABLE II. Transition dipole moments (a.u.).

R [Å]	$B\ ^3\Sigma_u^- - X\ ^3\Sigma_g^-$	$B''\ ^3\Pi_u - X\ ^3\Sigma_g^-$
1.4	0.0000	0.3707
1.5	0.2774	0.2966
1.6	0.6343	0.2157
1.7	0.8144	0.1464
1.8	0.9088	0.1002
1.9	0.9489	0.0738
2.0	0.9520	0.0602
2.1	0.9298	0.0538
2.2	0.8910	0.0512
2.3	0.8409	0.0503
2.4	0.7819	0.0497
2.5	0.7139	0.0489
2.6	0.6359	0.0476
2.7	0.5471	0.0456
2.8	0.4497	0.0430
2.9	0.3500	0.0400
3.0	0.2567	0.0368
3.2	0.1187	0.0301
3.4	0.0504	0.0238
3.6	0.0221	0.0186

interactions. The accurate description of the system would involve treatment of both $^3\Sigma^-$ and $^3\Pi$ states weighted by some angle-dependent function or, less rigorously, by some averaged contribution of the two PECs. However, as seen in Fig. 4, the two curves differ only slightly at internuclear distances important for the initial step of recombination. Thus we feel confident to rely only on the ground $^3\Pi$ state in the simulation. The calculated energies for $1\ ^1\Sigma^+$, $2\ ^1\Sigma^+$, $^3\Sigma^-$, $^1\Pi$, $^3\Pi$, and $^1\Delta$ states are collected in Table IV.

The concept of BSSE always present in calculations based on atomic orbitals may contribute significantly to the obtained binding energies of weakly interacting molecular systems. For MRCI theory the BSSE correction is not, however, a straightforward procedure. We have omitted this concern since our MRCI+Q/avqz-Stutt. Calculation for the ground state matches almost exactly the previous CCSD(T)/avqz computation where BSSE was corrected for.[3] The magnitude of the BSSE correction was estimated as 13.7 cm^{-1} for the well depth. The main difference between the two calculations lies probably in the basis set of Ar. The avqz basis yields stronger interaction that is then reduced by the BSSE correction. The net effect leads to numbers very similar to what is obtained in the present work relying on valence electron correlation alone. Furthermore, we observed no significant difference between the ACPF and Davidson cor-

TABLE III. The calculated transition probabilities W_{fi} (s^{-1}) for the $B\ ^3\Sigma_u^-$ and $B''\ ^3\Pi_u$ state emissions to the ground $X\ ^3\Sigma_g^-$ state along with the radiative lifetimes τ (μs).

Vibronic level v''	$B(v'=0)\rightarrow X(v'')$ $W_{fi}\times 10^3$ [s^{-1}]	$B''(v'=0)\rightarrow X(v'')$ $W_{fi}\times 10^3$ [s^{-1}]
0	5.769	0.000
1	52.46	0.001
2	235.0	0.008
3	691.2	0.039
4	1 502	0.139
5	2 574	0.398
6	3 614	0.949
7	4 267	1.935
8	4 303	3.431
9	3 755	5.380
10	2 878	7.571
11	1 976	9.669
12	1 239	11.36
13	712.0	12.23
14	364.9	12.07
15	159.1	10.93
16	57.48	9.143
17	18.58	7.151
18	6.865	5.280
19	3.320	3.683
20	1.432	2.401
21	0.268	1.447
22	0.002	0.808
23	0.002	0.426
24	0.002	0.216
Lifetime τ [μs]	0.0352 (0.032)[a]	6.25 (4.16)[a]

[a] Values in parentheses are those of Green and Western (Ref. 30) for pure (nonmixed) B and $B''(\Omega=2)$ states.

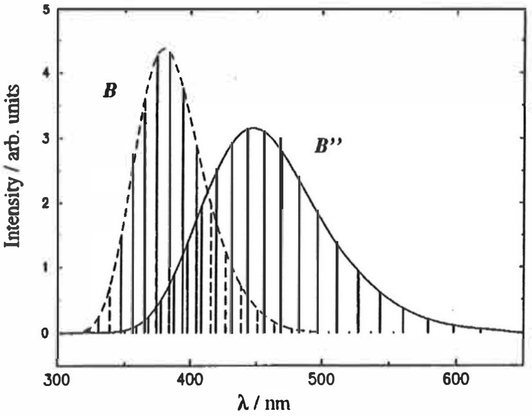

FIG. 3. The calculated emission spectra for $B''\ ^3\Pi_u \rightarrow X\ ^3\Sigma_g^-$ and $B\ ^3\Sigma_u^- \rightarrow X\ ^3\Sigma_g^-$ (dashed lines) band systems of S_2. The intensities of the B'' state emission are scaled up by a factor of 256. The envelopes are added to guide the eye.

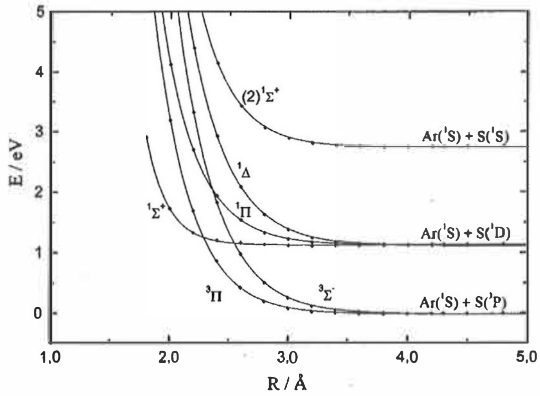

FIG. 4. Calculated points of potential energy curves for the states of ArS considered in this study. No scaling of the free atom limits is performed.

TABLE IV. Calculated MRCI+Q energies (a.u.) for ArS states of $^3\Pi$, $^3\Sigma^-$, $^1\Sigma^+$, $^1\Pi$, and $^1\Delta$ symmetries relative to −418.0 a.u.

R[Å]	$^3\Pi$	$^3\Sigma^-$	$^1\Sigma^+$	$^1\Pi$	$^1\Delta$	(2) $^1\Sigma^+$
1.8	−0.576 395 2	−0.429 095 4	−0.686 152 9	−0.544 792 0	−0.393 425 8	−0.362 234 8
2.0	−0.675 083 2	−0.577 842 8	−0.729 322 6	−0.640 774 6	−0.539770 2	−0.503 120 2
2.2	−0.730 199 8	−0.670 376 3	−0.743 943 1	−0.693 375 3	−0.630 801 9	−0.590 340 3
2.4	−0.760 390 7	−0.725 135 7	−0.748 254 9	−0.721 382 0	−0.684 759 1	−0.640 006 7
2.6	−0.776 581 3	−0.756 351 2	−0.749 721 1	−0.736 067 4	−0.715 545 1	−0.666 449 6
2.8	−0.785 023 2	−0.773 629 5	−0.750 561 9	−0.743 670 2	−0.732 577 3	−0.679 646 5
3.0	−0.789 273 9	−0.782 966 5	−0.751 067 2	−0.747 530 8	−0.741 759 4	−0.685 990 8
3.2	−0.791 321 5	−0.787 901 7	−0.751 267 7	−0.749 430 0	−0.746 592 9	−0.688 991 6
3.4	−0.792 243 0	−0.790 445 7	−0.751 260 1	−0.750 312 2	−0.749 068 9	−0.690 382 1
3.6	−0.792 604 9	−0.791 709 0	−0.751 145 9	−0.750 675 3	−0.750 287 1	−0.690 990 3
3.8	−0.792 699 7	−0.792 297 4	−0.750 994 3	−0.750 781 2	−0.750 846 2	−0.691 217 9
4.0	−0.792 676 8	−0.792 539 1	−0.750 843 5	−0.750 768 1	−0.751 069 3	−0.691 265 1
4.2	−0.792 610 1	−0.792610 3	−0.750 71 1 0	−0.750 707 7	−0.751 129 1	−0.691 233 4
4.5	−0.792 499 2	−0.792 587 5	−0.750 556 3	−0.750 600 4	−0.751 097 2	−0.691 141 3
4.8	−0.792 408 2	−0.792 522 8	−0.750 449 6	−0.750 509 3	−0.751 028 5	−0.691 051 7
5.5	−0.792 287 1	−0.792 403 4	−0.750 320 6	−0.750 385 0	−0.750 907 0	−0.690 921 3
6.5	−0.792 228 0	−0.792 336 7	−0.750 260 6	−0.750 323 0	−0.750 840 3	−0.690 854 2

rected results, both in absolute values and well parameters; thus the two methods for approximately attaining size consistency proved to yield equivalent results. The test calculations on the S_2 ground state showed that the selected active space when combined with the vqz or avqz basis sets yields slight decrease of the well depth when Davidson correction was applied to the MRCI calculation. By adapting a smaller, say $12e/8o$ space, the situation was reversed. These observations are in accord with previous findings that large CASSCF space in the MRCI treatment of dissociation approaches size consistency already, and inclusion of Davidson correction results in artificial lowering of the separated atom limit due to double counting of some correlation effects.[28] The calculated correction for the X state is −0.82 eV at $R=1.9$ Å and −0.86 eV near the dissociation region. The resulting reduction of D_e is of the same magnitude as reported for N_2 in Ref. 28. This is, however, not the case generally. For example, Davidson correction increased significantly binding of the B'' state.

D. Thermally induced recombination

Placing the two sulfur atoms as nearest neighbors in the lattice (S–S separation ca. 3.76 Å) led to immediate recombination during temperature scaling even at 1 K simulation temperature. In order to test if instability of the system during temperature scaling was responsible for recombination at such a low temperature, the attractive ground state S–S potential was replaced with the Ar–Ar potential for the period of temperature scaling. After temperature scaling was switched off, the correct potential was returned. Even with this precaution, recombination occurred directly after the potential switch. This result clearly implies that the nearest neighbor configuration is not stable and thus not responsible for the observed low temperature S+S thermoluminescence in sulfur doped matrices.

The lattice configuration where sulfur atoms are separated by one lattice constant (see Fig. 1) was thermally stable and no recombination was observed in the simulations up to 80 K. A simple pairwise calculation using a static lattice structure yields an approximate barrier height of 1360 cm^{-1} (ca. 0.17 eV) for the S+S recombination. Thus in a perfect lattice thermoluminescence due to pairs trapped in this configuration seems unlike at temperatures below 20 K. The potential barrier can be lowered by issuing lattice vacancies in the plane perpendicular to the diatomic reaction coordinate. The four relevant Ar atoms are labeled Ar_1 to Ar_4 in Fig. 1. The percentage of reactive trajectories leading to S+S recombination, when 2, 3, or 4 vacancies were introduced, is shown in Fig. 5. The first onset of recombination is at ca. 5 K and the second at ca. 15 K corresponding to four and three vacancies, respectively. The total number of trajectories considered for each temperature was 16. Although single vacancy did not promote recombination within the simulation time even at 80 K, it still may contribute in the experimental

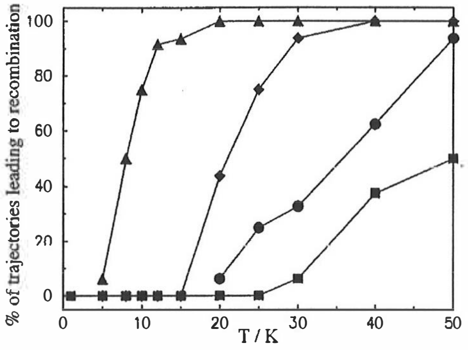

FIG. 5. Thermally induced recombination of S atoms in Ar lattice with lattice vacancies in the four atom plane perpendicular to the reaction coordinate (see Fig. 1). Percentage of reactive trajectories showing clear thermal onsets are displayed. Statistical accumulation was obtained from 16 simulations. The opposite (Ar_1 and Ar_2 removed) and neighbor (Ar_1 and Ar_3 removed) two vacancy cases are marked with squares (■) and circles (●), respectively. The diamonds (◆) and triangles (▲) indicate three and four vacancies, respectively.

time scale. On the contrary, the high reactivity of the three and four vacancy cases might make these configurations too short lived to be observed in the glow curve measurements.

The simulations involving excited electronic states were performed for perfect and vacancy doped lattices in a similar way as explained. It should be noted that the true situation is, however, more complex. The excited nonspherical $S(^1D)$ atom is subject to anisotropic interactions with its neighbors in the lattice. Effectively, the interaction is dependent on the orbital orientation and involves the $^1\Sigma^+$, $^1\Pi$, and $^1\Delta$ potentials. Although the effects of nonspherical interactions are outside our present scope, we performed some test calculations based on a less rigorous approach. Since it is quite expected that at moderate photon densities only one of the S atoms in the trapped pair is excited, only this situation is explored. The appropriate pair potentials are thus: Ar–Ar ground state, $Ar–S(^3P)$, $Ar–S(^1D)$, and $S(^3P)–S(^1D)$, that is, the $^3\Pi$, $1\,^1\Sigma^+$, and $B\,^3\Sigma_u^-$ states, respectively. The thermal motion of the excited S atom is dictated by the singlet states, $1\,^1\Sigma^+$ being the one which, based on the computed trajectories, allows largest amplitude motion in the cage. At the first glance, this could be expected to enhance the probability for recombination. However, the effect proved to be the opposite as the more bound $1\,^1\Sigma^+$ state prevents recombination by stronger trapping as seen in the radial distribution functions. By introducing four or three vacancies onsets of reactive trajectories similar to Fig. 5 are observed at 15 K and 25 K. Before continuing, we note that all simulations except the above discussed excitation case are based on ground state S–S potential and the $^3\Pi$ state potential of Ar–S.

E. Shock wave induced recombination

In order to unravel the microscopic mechanism behind the experimental observation, i.e., that optical excitation in the visible range induces S+S recombinant emission in matrix samples doped with atomic sulfur,[3] two distinct approaches were tested in the simulations. In the local excitation model the nearest neighbor Ar atom in the S···S···Ar configuration (135° angle) was subject to kinetic excitation toward the nearest S atom. The initial energy of this impulsive excitation was adjusted to 1.1 eV corresponding to the energy separation of the two lowest states of atomic sulfur, which is the only absorber in the wavelength of the experiment. Thus the recombination cross section is dependent on the component of the kinetic energy along the line of reactive S centers. Table V collects the recombination probabilities extracted for this model. Although the statistics of this analysis is rather limited, it is obvious that local excitation at this energy does efficiently promote recombination even in a perfect lattice. By introducing lattice vacancies near the reaction center, the probability for recombination can be further increased. In this respect, a vacancy situated along the line of initial excitation (Ar_2 in Fig. 1) has the strongest influence on the reaction.

Kinetic excitation of more remote lattice atoms can also promote reaction. In fact, shock wave induced ground state S+S recombination with initial kinetic excitation energies of 2 eV or more is very efficient provided that the direction of the wave is favorable for one of the sulfur atoms to gain kinetic energy in the S–S direction (see Fig. 1). Lower energies are not sufficient for this process; for example, 1.0 eV can induce recombination only by local excitation of the nearest neighbor Ar atom. This is due to the fact that only part of the kinetic energy is transferred along the S–S direction. Consistent with the energy transfer law, excitation along the ⟨100⟩ direction containing both S atoms diverged effectively along the lattice diagonals and thus missed the sulfur atoms. With correct direction and sufficient energy (ca. 2 eV) a shock wave can travel through at least five argon atoms and still induce the S–S pair to recombine. The wave itself can travel long distances exceeding the dimensions of the periodic cube. These artificial effects were taken into account when analyzing the data. An example of shock wave propagation in a pure argon lattice is shown in Fig. 6. After the time period shown the shock wave reaches the periodic boundary.

TABLE V. Trajectory statistics for the S+S recombination induced by local 1.1 eV kinetic energy excitation of the nearest neighbor Ar atom in perfect (64 trajectories) and vacancy doped (16 trajectories) lattices (see text and Fig. 1 for details). The total simulation time is 20 ps with 5 ps thermalization time. In most cases, reaction occurs within 0.3–0.4 ps after excitation.

Vacant site	# of recombination	Vacant site	# of recombination
–	4	3,2,4	16
1	1	1,2,3	16
2	16	3,1,4	4
3	3		
1,2	16	1,2,3,4	16
2,3	16		
3,4	7		
1,3	3		

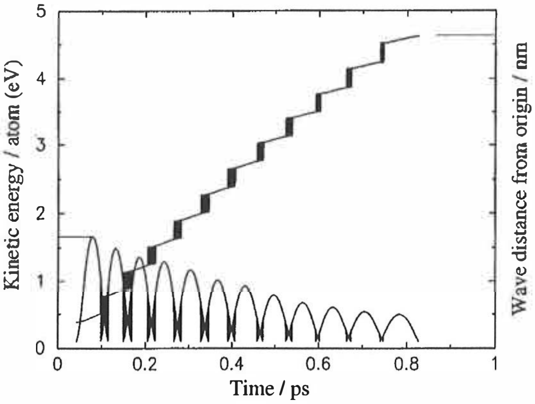

FIG. 6. Time behavior of a shock wave generated by 2.0 eV kinetic energy excitation of one argon lattice atom. The direction of the excitation is toward one of the nearest neighbor atoms. Wave propagation perpendicular to the excitation direction is minor. Step height in the wave distance graph corresponds to the nearest neighbor distance (3.76 Å) in the argon lattice.

IV. DISCUSSION

Although the present calculation does not exceed the accuracy obtained in Ref. 7 for the molecular parameters of S_2, for our purpose, however, the PECs are of sufficient quality and the T_0 and T_e values for states of spectroscopic interest are in good agreement with the experiments. Moreover, the rest of the calculated potentials are in accordance with the quantitative picture given in Ref. 5 over 20 years ago, and the available experimental data. The spectra predicted by vibronic averaging of the transition moments can be compared to gas phase $B\,^3\Sigma_u^- - X\,^3\Sigma_g$ and Ne matrix isolated $B''\,^3\Pi_u - X\,^3\Sigma_g$ emissions. The values for λ_{00} given in Ref. 27 are 315.6 nm and 323.1 nm, respectively. The transition observed in the gas phase has a perfect coincidence with our calculation and the 233 cm^{-1} difference relative to the measurement in the Ne matrix may be considered as a typical matrix red shift. The computed vibronic envelope of the $B''-X$ transition shows maximum intensity at 445 nm, whereas, depending on the temperature, the measured maximum intensity is in the range 410–420 nm.[27] This comparison indicates some additional modification of the potentials by lattice effects. The obtained radiative lifetime 35.2 ns for the $B(v'=0)$ level agrees perfectly with the previous computational work by Pradhan and Partridge[7] and the experimental values of 35 ns and 32 ns reported in Refs. 29 and 30, respectively. On the other hand, our result 6.25 μs for the B'' state shows clear deviation from the earlier calculation (25.5 μs)[7] but is in better accordance with the experiments. A recent detailed analysis of the $B''-X$ emission system yielded a radiative lifetime of 4.2 μs for the nonmixed $\Omega=2$ component of the B'' state.[30] For comparison, the Ne matrix value for this transition is 1.4 μs.[27]

On the grounds of the above discussion we conclude that *ab initio* pair potential data fulfil the requirements needed for subsequent simulation of recombination dynamics. The obvious shortcomings of the simulation are related to relatively short simulation time, relatively limited statistics, and the neglect of quantum effects. Continuous energy spectrum of S atom motion and neglect of zero-point energies are inevitable consequences of the classical treatment, and may affect the obtained reliability by some extent. Second, the effects of Ar–S anisotropy and multi-body interactions not described by simple pair additivity are by no doubt issues which play a role in a real system. Nevertheless, we believe that the present treatment is of sufficient sophistication to shed new light into short-range recombination reactions in solids and, in practice, to raise the discussion in Ref. 3 to a more quantitative level.

The clear outcome of the present classical simulations is that S atoms separated by one lattice constant do not recombine thermally in a perfect Ar lattice. Consequently, only by introducing lattice vacancies near the trapped S atoms, thermal recombination behavior quite similar to the experiments can be reproduced. Considering the actual situation in the experiments, i.e., *in situ* photolysis of relatively large H_2S_2 molecule, it is not unexpected that multiple substitutional trapping sites might contribute to the observed thermally induced recombination. Further evidence for short-range recombination mechanism is provided by recent experiments with different photolysis wavelengths.[31] It was observed that photolysis of H_2S_2 at 193 nm leads not only to pairwise trapping of S atoms, but also isolated S atoms. These atoms are thermally stable and do not contribute to the thermoluminescence signal. It is important to note that laser radiation at this photon energy yields purely in-cage photodissociation with no cage-exit of sulfur atoms. In fact, the source for the isolated S atoms is the H_2S impurity in the sample. On the other hand, if photolysis is carried out at 266 nm, no isolated S atoms are produced since H_2S is transparent to this wavelength. Instead, annealing of extensively irradiated solids shows strong thermoluminescence and bleach of S atoms.

The electronic states of S_2 correlating to ground state S atoms all behave in very similar fashion at large interatomic distances. Therefore, the simulation data obtained for the ground state should also apply for the excited states of S_2 possessing the same free atom asymptote. Recombination via the radiative B'' state is expected to proceed with a smaller branching probability due to weaker atom–atom force provided by this potential curve at long distances, but should show similar dynamics as the ground state does. One of the initial hypotheses in Ref. 3, namely that photoinduced recombination might be due to enhanced capture radius when one of the S atoms is excited, was not supported by the present simulations. Even though simulations involving excited state atoms are relatively inaccurate due to neglect of orbital anisotropy, the picture is clear in the sense that excited state potentials do not lead to enhanced probability for recombination. Thus we are left with a mechanism, which describes photoinduced recombination in terms of phonon emission. As discussed, kinetic excitation near 1 eV corresponding to $^1D-^3P$ relaxation is sufficient only by local excitation of the nearest neighbor Ar atom toward a favorable direction. More distant kinetic excitation initiates artificial shock waves in the lattice and promote S+S recombination at excitation energies of 2 eV or more. Increase of the excitation energy favors reactive trajectories for both cases in a way very similar to increasing the number of vacancies near the reaction center. Taken into account the obvious shortcuts made in the theoretical treatment as compared to the real complex chemical system, we feel rather confident that shock waves following phonon sideband absorption are, indeed, very probable source for the experimental observations of Ref. 3. Finally, thermal release of atoms trapped at short distances in pairs is a very plausible mechanism also for other systems, e.g., the strong thermoluminescence in photolysed NO doped Ar and Kr matrices.[32]

ACKNOWLEDGMENT

This research is funded by the Academy of Finland.

[1] A. M. Bass and H. P. Broida, *Formation and Trapping of Free Radicals* (Academic, New York, 1960).

[2] L. Khriachtchev, M. Pettersson, E. Isoniemi, and M. Räsänen, J. Chem. Phys. **108**, 5747 (1998); B. Grigorenko, L. Khriachtchev, A. Nemukhin, M. Pettersson, E. Isoniemi, and M. Räsänen, *ibid.* **110**, 5836 (1998); M. Pettersson, J. Lundell, L. Khriachtchev, E. Isoniemi, and M. Räsänen, J. Am. Chem. Soc. **120**, 7979 (1998); L. Khriachtchev, M. Pettersson, E. Isoniemi, J. Lundell, and M. Räsänen, Chem. Phys. Lett. **302**, 324 (1999).

[3] L. Khriachtchev, M. Pettersson, S. Pehkonen, E. Isoniemi, and M. Räsänen, J. Chem. Phys. **111**, 1650 (1999).

[4] T. Kiljunen, J. Eloranta, and H. Kunttu, J. Chem. Phys. **110**, 11814 (1999); J. Ahokas, T. Kiljunen, J. Eloranta, and H. Kunttu, *ibid.* **112**, 2420 (2000).

[5] W. C. Swope, Y-P. Lee, and H. F. Schaefer III, J. Chem. Phys. **70**, 947 (1979).

[6] M. D. Wheeler, S. M. Newman, and J. Orr-Ewing, J. Chem. Phys. **108**, 6594 (81998).

[7] A. D. Pradhan and H. Partridge, Chem. Phys. Lett. **255**, 163 (1996).

[8] S. R. Langhoff, J. Chem. Phys. **73**, 2379 (1980); T. H. Dunning, Jr. and P. J. Hay, *ibid.* **66**, 3767 (1977); J. S. Cohen, W. R. Wadt, and P. J. Hay, *ibid.* **71**, 2955 (1979).

[9] M. Yamanishi, K. Hirao, and K. Yamashita, J. Chem. Phys. **108**, 1514 (1998).

[10] A. V. Nemukhin, B. L. Grigorenko, and A. A. Granovsky, Chem. Phys. Lett. **301**, 287 (1999).

[11] D. E. Woon and T. H. Dunning, Jr., J. Chem. Phys. **98**, 1358 (1993).

[12] A. Nicklass, M. Dolg, H. Stoll, and H. Preuss, J. Chem. Phys. **102**, 8942 (1995).

[13] H.-J. Werner and P. J. Knowles, J. Chem. Phys. **89**, 5803 (1988); P. J. Knowles and H.-J. Werner, Chem. Phys. Lett. **145**, 514 (1988); Theor. Chim. Acta **84**, 95 (1992).

[14] P. J. Knowles and H.-J. Werner, Chem. Phys. Lett. **115**, 259 (1985); H.-J. Werner and P. J. Knowles, J. Chem. Phys. **82**, 5053 (1985).

[15] MOLPRO 96 is a package of *ab initio* programs written by H.-J. Werner and P. J. Knowles, with contributions from J. Almlöf, R. D. Amos, A. Berning, M. J. O. Deegan, F. Eckert, S. T. Elbert, C. Hampel, R. Lindh, W. Meyer, A. Nicklass, K. Peterson, R. Pitzer, A. J. Stone, P. R. Taylor, M. E. Mura, P. Pulay, M. Schultz, H. Stoll, T. Thorsteinsson, and D. L. Cooper.

[16] C. E. Moore, *Atomic Energy Levels*, Nat. Stand. Ref. Data Ser., Nat Bur. Stand. (US) 35/V.I (1971).

[17] M. R. A. Blomberg and P. E. M. Siegbahn, J. Chem. Phys. **78**, 5682 (1983); S. R. Langhoff and E. R. Davidson, Int. J. Quantum Chem. **8**, 61 (1974).

[18] H.-J. Werner and P. J. Knowles, Theor. Chim. Acta **78**, 175 (1990); R. J. Gdanitz and R. Ahlrichs, Chem. Phys. Lett. **143**, 413 (1988).

[19] F. Scheid, *Numerical Analysis* (McGraw-Hill, New York, 1968).

[20] Numerical Algorithms Group (NAG), Library M16 (Oxford, 1993).

[21] K. Refson, *Moldy User's Manual* (Oxford University Press, Oxford, 1998).

[22] D. Beeman, J. Comput. Phys. **20**, 130 (1976); K. Refson, Physica B **131**, 256 (1985).

[23] B. Quentrec and C. Brot, J. Comput. Phys. **13**, 430 (1975).

[24] M. P. Allen and D. J. Tildesley, *Computer Simulations of Liquids* (Claredon, Oxford, 1987).

[25] G. C. Maitland, M. Rigby, E. B. Smith, and W. A. Wakeham, *Intermolecular Forces: Their Origin and Determination* (Oxford Science, Oxford, 1987).

[26] A. Cenian, S. Hennig, and H. Gabriel, J. Chem. Phys. **102**, 9276 (1995); see also A. Borrmann and C. C. Martens, *ibid.* **102**, 1905 (1995) for the two dimensional case.

[27] V. E. Bondybey and J. H. English, J. Chem. Phys. **72**, 3113 (1980); D. A. Peterson and L. A. Schlie, *ibid.* **73**, 1551 (1980).

[28] J. Almlöf, B. J. Deleeuw, P. R. Taylor, C. W. Bauschlichter, Jr., and P. Siegbahn, Int. J. Quantum Chem., Symp. **23**, 345 (1989).

[29] C. R. Quick and R. E. Weston, J. Chem. Phys. **74**, 4951 (1981).

[30] M. E. Green and C. M. Western, J. Chem. Phys. **104**, 848 (1996).

[31] L. Khriachtchev and M. Pettersson (unpublished).

[32] J. Eloranta, K. Vaskonen, H. Häkkänen, T. Kiljunen, and H. Kunttu, J. Chem. Phys. **109**, 7784 (1998).

PAPER IV

https://doi.org/10.1063/1.1360796

Reprinted with permission from T. Kiljunen et al, “Magnetic properties of atomic boron in rare gas matrices: An electron paramagnetic resonance study with ab initio and diatomics-in-molecules molecular dynamics analysis,” *The Journal of Chemical Physics* **114**, 2001, pp. 7144–7156.

JOURNAL OF CHEMICAL PHYSICS VOLUME 114, NUMBER 16 22 APRIL 2001

Magnetic properties of atomic boron in rare gas matrices: An electron paramagnetic resonance study with *ab initio* and diatomics-in-molecules molecular dynamics analysis

Toni Kiljunen,[a] Jussi Eloranta, Jussi Ahokas, and Henrik Kunttu
Department of Chemistry, University of Jyväskylä, P.O. Box 35, FIN-40351 Jyväskylä, Finland

(Received 16 November 2000; accepted 12 February 2001)

The anisotropic boron atom electron paramagnetic resonance spectra measured in rare gas matrices (Ar, Kr, Xe) are interpreted with the aid of highly correlated *ab initio* calculations including spin–orbit coupling and diatomics-in-molecules (DIM) molecular dynamics simulations. The heavy-element and crystal field effects are inspected as they contribute to the electron g-shift. The DIM-simulated p-orbital splittings and lattice perturbed hyperfine coupling values provide a good starting point for spectral fitting and show the correctness of the guidelines given by purely synthetic generation of the spectra. The present combination of experiment and theory resulted in improved accuracy of the parameters measured in Ar matrix, new values are extracted for Kr matrix, and tentative assignment is also provided for the Xe matrix case. © *2001 American Institute of Physics.* [DOI: 10.1063/1.1360796]

I. INTRODUCTION

The study of open shell atoms with orbital angular momentum necessitates consideration of the angular anisotropy of electron density. For such atoms isolated in rare gas (Rg) matrices, the orbital anisotropy provides a very sensitive probe for exploring the influence of a chemically inert solvent on the valence electron density of a solute. For the simplest system of this kind, a P state impurity surrounded by spherically symmetric host atoms, construction of the potential energy surfaces (PES) can be based on diatomic input in a rather straightforward manner. An especially advantageous approach to describe interactions of this type is the diatomics-in-molecules (DIM) model,[1] because the threefold degeneracy of the P state is removed under the influence of the surrounding resulting generally in three PES. Although PES obtained from DIM are strictly based on diatomic pair interactions, the DIM surfaces do not involve simple assumption of pairwise additivity, and are thus particularly suitable for condensed phase chemical dynamics in which multibody interactions play a crucial role.

Molecular dynamics (MD) simulations can be devised to quantitatively describe a rich variety of nonadiabatic processes operative in condensed phases.[2] The first DIM–MD study utilizing multiple electronic surfaces, allowing for nonadiabatic dynamics, was published by Gersonde and Gabriel and dealt with photodissociation of HCl and Cl_2 in Xe lattice.[3] Excited electronic states of guest atoms embedded in Rg clusters or in solid matrices have provided a very useful framework for exploring nonadiabatic dynamics in condensed phases. Methods, experiment, and theory, for pursuing this very challenging issue have evolved rapidly during the past years. Most of the theoretical studies on these systems have focused on simulating electronic absorption spectra[4,5] and only for a limited number of cases the nonadiabatic many-body dynamics is extracted in detail. Orbital reorientation dynamics of F (^2P) in solid Rg,[6,7] excited state dynamics of Ba in argon clusters,[8,9] and electronic energy relaxation of Cl (^2P) in solid argon[10] serve as representative examples of such studies. For more details on the subject, we refer to a recent comprehensive review by Apkarian and Schwentner.[11]

Electron paramagnetic resonance (EPR) has proven to be a powerful experimental technique for elucidating details of the electronic structure of molecules and ions in crystals and solutions. Because EPR transitions (i) depend solely on the properties of the electronic ground state, (ii) exhibit very narrow linewidths in dilute samples, and (iii) are very sensitive to small changes in the environment of the paramagnetic species under investigation, this method seems conceptually ideally suited for exploring the nature of trapping of matrix isolated atoms. Unfortunately, most of the available EPR data on atoms or ions in Rg matrices have concerned cases with isotropic g values and hyperfine interaction, and only very few atoms with orbitally degenerate ground states have been observed by EPR.[12] Although the failure to observe these transitions has been ascribed to anisotropic interactions with the lattice atoms, and subsequent broadening of the resonances, no rigorous theoretical treatment has been presented. Nevertheless, the apparent anisotropic origin of this effect would suggest that, perhaps, methodology somewhat analogous to what has been applied to optical spectroscopy could be adapted in the theoretical treatment of magnetic spectroscopy of ^2P atoms. After all, the magnetic parameters are in general tensors, which makes the DIM model particularly attractive to be applied here in a generalized form involving hyperfine coupling. In addition, we note that since the equilibrium geometries are of interest here, a low level DIM approach with valence diatomic contributions

---

[a] Author to whom correspondence should be addressed. Electronic mail: kiljunen@epr.chem.jyu.fi

should be sufficient. For the Group IIIB atoms pioneering EPR work exists,[13–15] and in order to elucidate the validity of this assumption, we have selected atomic boron isolated in Rg host as a test case for which the experimental EPR spectroscopy is partly reinvestigated and analyzed by a method combining highly correlated *ab initio* calculations and MD simulations in the DIM framework. In Ar, the earlier data is reproduced with better resolution, whereas in previously not studied Kr and Xe solids new experimental data is obtained.

For serious modeling of electron paramagnetic properties of B (^2P) embedded in a Rg lattice, a number of accurately computed quantum mechanical parameters are needed. First, the dependence of the B atom spin–orbit (SO) interaction magnitude ζ of the Rg–B interatomic distance is evaluated for Ar, Kr, and Xe (Sec. II). This parameter is further used to predict the shift in g tensor caused by perturbation of the host lattice. Second, the hyperfine tensor **A** as fragmented into its isotropic Fermi contact (FC) A_{iso} and anisotropic spin-dipolar (SD) $A_{\perp,\parallel}$ parts is also evaluated as a function of atomic separation (Sec. II). Finally, the effect of tetragonal crystal field (CF) perturbation in terms of the Δ parameter is attained in a DIM scheme with adiabatic states as inputs (Sec. III). While the existence of resonance patterns are exclusively due to hyperfine tensor values, the symmetry and position of the spectra are dictated by the interplay between the ζ and Δ parameters. The theoretical values obtained from *ab initio* and DIM computations are further utilized in simulation of the EPR spectra (Sec. IV) and compared with the experimentally derived parameters (Sec. V). Concluding remarks are given in Sec. VI.

II. *AB INITIO* CALCULATIONS

A. Computational methods

We use the internally contracted multireference configuration interaction (MRCI) method[16,17] for calculating the electronic states arising from degeneracy breaking of the boron atomic orbitals as a Rg atom approaches it. The MRCI calculation uses the orbitals obtained in a complete active space self-consistent-field (CASSCF) procedure[18,19] similarly as described in the subsequent paper.[20] In particular, 11 valence electrons were distributed in eight active orbitals producing a $11e/8o$ space. Also the boron $1s$ orbital was CASSCF optimized but not correlated. In addition, the multireference version of the Davidson correction was performed in order to obtain approximate size extensivity of the method (labeled MRCI+Q).[21] The ground state B(^2P)–Rg interatomic field generates three adiabatic states usually expressed in a $\{\Lambda S\Sigma\}$ Cartesian scheme, whereas the coupled description $\{\Omega\}$ is generally more appropriate for the spin–orbit coupled states. For a light nucleus as B, the fine-structure effects are minor thus the in-between notation $^M\Lambda_\Omega$ is well justified. Hence, the set of states labeled $\{X\,^2\Pi_{x,y}$ (or $^2\Pi_{\pm 1}$),$A\,^2\Sigma(^2\Pi_0)\}$ transforms to $\{^2\Pi_{1/2},{}^2\Pi_{3/2},{}^2\Sigma_{1/2}\}$. The transformation is done at each internuclear separation by diagonalizing the $[H_{\mathrm{el}}+H_{\mathrm{SO}}]$ Hamiltonian matrix, which contains the MRCI+Q calculated energies $\langle H_{\mathrm{el}}\rangle$ in the diagonal and the spin–orbit matrix elements off diagonal. In the calculation of the matrix elements, the full Breit–Pauli SO operator and the mean-field one-electron Fock operator were applied to internal and external configurations, respectively.[22]

The above described calculations were performed with the MOLPRO code,[23] using a correlation-consistent type basis set (aug-cc-pVQZ) of Dunning and co-workers[24] uncontracted for B, and a relativistic effective core potential (RECP) basis set of the Stuttgart group[25] for Rg. The RECPs retain the outer ns^2np^6 shells in the valence space which was further augmented with a $\{spdf\}$ set[26] of more diffuse functions. In addition, we utilized the knowledge of the basis set effects on the SO matrix elements. In a recent convergence study by Nicklass *et al.*[27] the importance of tight functions in describing the core–core and core–valence correlation contributions to the Breit–Pauli operator was shown. Therefore, the final calculations were performed with the aug-cc-pCVQZ boron basis set[28] (up to f functions) which was, due to program limitations, transformed from general to segmented contraction by the procedure described by Davidson.[29]

The above methodology allows one to study the second order contribution to the g tensor. In the well established scheme, the sum over states (SOS) bilinear perturbation formula is[30,31]

$$g_{ab}=g_e\delta_{ab}+g_e\sum_{n\neq 0}\frac{\langle 0|\mathrm{SO}_a|n\rangle\langle n|L_b|0\rangle}{E_n-E_0},\quad a,b=x,y,z \qquad (1)$$

and shows direct proportionality of g_{ab} to the spin–orbit (SO) and orbital-Zeeman (L) transition matrix elements of the unperturbed (MRCI) wave functions. The prefactor g_e accounts for the missing $-g_e/2$ term in the applied SO operator and the complex conjugate (×2). This is what is usually essential for explaining the (negative) g shift ($\Delta g_\perp = g_\perp - g_e$, $\Delta g_\parallel \simeq 0$) of an orbitally quenched p-electron ($P_{1/2}$) atom behaving similarly as a randomly oriented $^2\Sigma$ molecule in an axial crystal field. Since the rigorous and gauge invariant complete-to-second-order treatment considering also the first-order expectation values (the relativistic mass correction to the spin-Zeeman term and the spin-Zeeman gauge correction terms)[32] is beyond our scope here, we approach the subject by relying on the assumption usually confirmed,[33,34] that the second-order contribution is by far the most important in attaining the g shifts and only a few lowest states are significant in the SOS expansion. The validity of this assumption has been shown for several radicals possessing large g-shift components, dominated by large noncanceling second-order contributions.[33,34] For smaller g shifts, on the other hand, the second-order effects are generally less pronounced.

In a lattice surrounding of axial symmetry the orbital degeneracy is lifted so that the $^2\Sigma(\sigma_z)$ state becomes the most stable and is therefore the ground state $|0\rangle$ in Eq. (1), and mixing occurs with the upper $\pi_{x,y}$ levels $|n\rangle$ in this p-orbital scheme. This simple crystal field model is not, however, valid for all cases. It does not, for example, account for the positive $g_\perp$ shift of Al in Xe.[14] Here, although the increasing polarizability of the lattice medium (going from Ar to Xe) is expected to produce more extensive p-orbital splitting and therefore a smaller g shift, the matrix elements remain practically intact and no change in the sign of Δg may be anticipated. This can be verified in atomic calculations by issuing relevant lattice point charges to generate crystal fields of various strength. Next step in the line of approximation would be replacement of the point charges with actual rare gas atoms in order to study how host atom spin–orbit coupling and higher electronic states come into the play. However, while we could make a reasonable assumption of the cluster geometry or use the lattice structures obtained from the DIM simulations described later, this becomes computationally too expensive with the present MRCI wave functions. Therefore, only the Rg–B pairs are investigated, up to the states arising from the B $2s^1 2p^2 (^2D)$ atomic asymptote. Note that since the spin–orbit evaluation described above attains only the contribution of active electrons we have so far disregarded the Rg core contribution. This is described by the spin–orbit terms in the RECPs and is evaluated separately. It is reasonable to expect this contribution to be the main effect and origin for the observed g-shift behavior with respect to different hosts. Finally, the excited states of charge-transfer character for which the most prominent Rg SO effect is expected (i.e., Rg $np \rightarrow$ B p excited ionic states) are shortly examined (CASSCF only).

In order to attain proper description of the hyperfine structure, yet another methodology is utilized as follows. The isotropic part of the electron–nuclear hyperfine coupling requires special attention for the basis sets used. This is the s-wave contribution of the spin density at the magnetic nucleus, composed of spin polarization of the closed shell α–β populations, and caused by the unpaired p-electron. This is handled by the electron correlation via configuration interaction. Experience has shown[35] that an increasingly balanced description of the important core and valence correlation effects is achieved with (aug-) cc-CVXZ (X=D,T,Q,5) basis sets. Therefore, the chosen basis set was that of triple-zeta-type (aug-cc-CVTZ), and also the more extended wave function dependent dipolar part of the interaction was obtained with the same method. The rare gas basis sets were the same (RECPs) as above. Second, the triple excitation level has shown to bear the important configuration contributions to the isotropic hyperfine coupling constants.[36] Therefore, the spin-unrestricted self-consistent-field (UHF) wave function effectively providing spin-polarization single excitations was used as the reference for quadratic CI singles+doubles (QCISD)[37] evaluation, which together produce triply excited configurations in a spin-restricted (RHF) sense. It is important to note that a calculation of this type necessitates the correlation of all B atom electrons, thus no frozen core orbitals were assigned. Two sets of hyperfine data were produced: one for the $X\,^2\Pi$ state Rg–B interaction and the other for $A\,^2\Sigma$ state. This part of the study was performed in the framework of the GAUSSIAN code.[38]

B. Fine structure

For the calculation of spin–orbit states, a usual approximation is to take the atomic coupling ζ as a semiempirical constant ($\zeta\ ^{11}\mathrm{B}=10.17\,\mathrm{cm}^{-1}$)[39] for producing the SO splitting for the entire potential energy curve (PEC). Here, we have calculated the spin–orbit matrix elements along the curves to provide guidelines on how this value is affected by the Rg lattice. The SO matrix elements were calculated at Rg–B distances between 2 and 20 Å and the deviation from the asymptotic value becomes notable in the 2–5 Å region. However, the splitting between the states gets smaller at internuclear distances where the $^2\Sigma$ state starts to deviate from the $^2\Pi$ states, leading to smaller interaction of the states as the $[H_{\mathrm{el}}+H_{\mathrm{SO}}]$ matrix becomes dominated by the $^2\Sigma$ energy. In particular, the asymptotic splitting equal to say $3\langle\Psi_x|\mathrm{SO}_z|\Psi_y\rangle$ decreases to a value of approximately 2/3 of this. Therefore, the usual semiempirical method proved to be a reasonable approximation at distances relevant to the stable lattice structures where the closest Rg atoms are expected to be near 4 Å. Consequently, the variation of the effective molecular parameter ζ to be utilized later when estimating the g shifts is relatively insignificant in this valence electron approximation. It is only well below 3.0 Å where the collapse of the B atom ζ prevents the use of this value as a constant. This is, in fact, the region where the heavy-element effect likely becomes most important. In this respect the splittings in the above generated potential curves become spurious due to the neglected contributions.

The other goal of this study is to unravel the effects of CI and one-electron spaces. Similar trend as observed by Nicklass *et al.*[27] was seen in that valence correlation diminishes the SO matrix elements, while core correlation has an opposite effect. The rapid basis set convergence is evidenced also for the B atom, and at the quadruple-zeta level the segmented contraction does not alter the SO values significantly (<1%) from the uncontracted ones. Inclusion of tight core–valence functions has a diminishing effect on Rg–B pair interaction energies, however. Therefore, in order to produce more accurate spin–orbit PECs, it seems reasonable to use the valence basis set energies and core–valence SO matrix elements in the diagonalization. The curves in Fig. 1 are obtained with valence basis set only. The improvement gained by CVQZ functions is vanishingly small for a light atom as B.

The additional contribution due to Rg core was obtained by SO integration with the RECP parameters. This contribution is asymptotically zero and increases with increasing orbital overlap at shorter Rg–B distances. Figure 2 manifests this behavior. In the case of Ar the contribution is yet small, but already for Kr the RECP SO is comparable with the boron contribution, and as expected, for Xe the core contribution is dominant. The resulting spin–orbit splitting thus consists of an antibonding mixture of the valence Rg and B p orbitals and its relative magnitude reflects the heavy-element effect increasing towards Xe. The CASSCF results for the ionic Rg–B states showed that these states may have a considerable effect to EPR spectra in heavy-atom surrounding provided that the energy separation is not too high and the transition matrix elements (L) differ from zero. For example, in the case of XeB the value of $\langle\Psi_z|\mathrm{SO}_x|\Psi_{\mathrm{ion}}\rangle$ increases rapidly from 35 cm^{-1} to 45 cm^{-1} between 4.0–3.8 Å.

C. Electron *g* matrix

The ground $A\,^2\Sigma$ state in C_{2v} symmetry belongs to the A_1 representation and is magnetically coupled to the $^2\Pi$

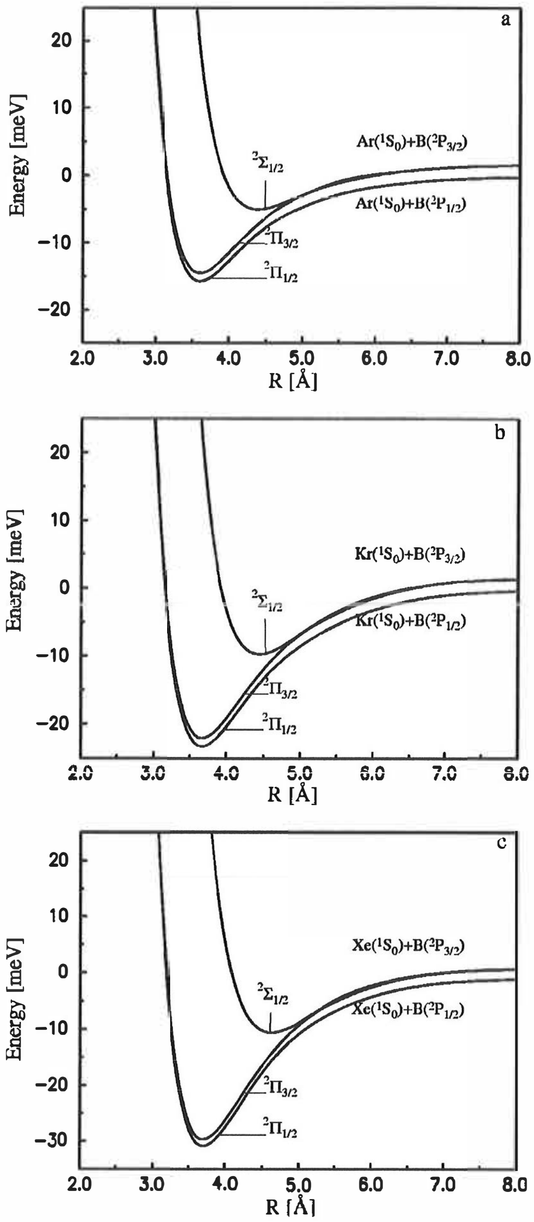

FIG. 1. The potential energy curves for Rg–B including spin–orbit coupling. The boron SO coupling remains practically constant within the range shown.

states (B_1 and B_2). It was sufficient to calculate the matrix elements connecting A_1 and B_2 ($SO_x \cdot L_x$) because $\Delta g_{xx} = \Delta g_{yy}$. The relevant configurations for $|n\rangle$ were thus B $1s^2 2s^2 2p_y (X\,^2\Pi)$ and B $1s^2 2s 2p_z 2p_y (D\,^2\Pi)$ for boron atom single excitations and Rg(p_z)B($2p_z 2p_y$) for the ionic configuration. We note that the calculated natural orbitals revealed no mixing of the Rg $np^5(n+1)$ Rydberg character into the ionic states (or valence states, as well), at least for $R > 2.6$ Å with the present augmentation. In Table I we summarize the results of the computations for the three excited states considered and separate the valence and RECP contributions. The values are those extracted from the PEC calculations at the presumed nearest neighbor distances of 3.6 Å (Ar), 3.9 Å (Kr), and 3.8 Å (Xe) corresponding to the first peak in DIM radial distribution functions (see Sec. III). The predicted values, in ppm, are however not very useful due to the somewhat gauge dependent orbital–Zeeman values. This is not an issue for the lowest state, as indicated by the single (L) value, but the upper states suffer from this flaw. The range in the fifth column corresponds to gauge origins varying from B to Rg, whereas the center-of-mass (c.m.) origin is used for the single values. The gauge variance was of the order of 0.1–0.3 a.u./Å as estimated by shifting the origin

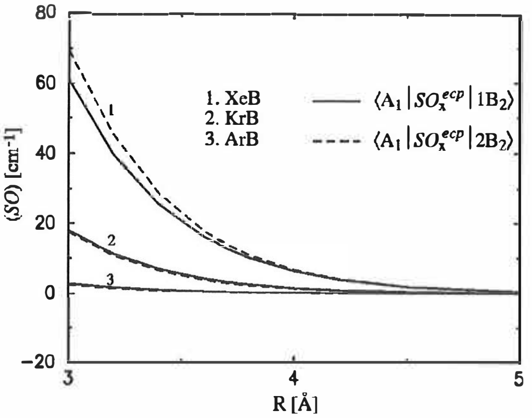

FIG. 2. The spin–orbit matrix elements of the Rg core contribution. The interacting states are denoted by their symmetries: A_1 is the $\Lambda = 0$ ground state and B_2 states are the lowest $\Lambda = 1$ states correlating to boron ^2P and ^2D atomic asymptotes. Note that the energy ordering includes the crystal field splitting in the Rg host lattices.

TABLE I. The spin–orbit [SO(valence)+SO(core)], angular momentum (L), and vertical/DIM excitation energy ΔE contributions in second order to electron g tensor for the $A\,^2\Sigma$ Rg–B ground state[a] (A_1).

Rg	$\|n\rangle$	SO_x (cm^{-1})	SO_x^{ecp} (cm^{-1})	L_x (a.u.)[b]	ΔE (cm^{-1})[c]	$\Delta g_\perp$ (ppm)[d]
	y	4.91	−0.64	0.993	540	−31 410
Ar	yz	−0.019	−0.52	0.01–1.04	49 750	40
	ion	0.211	5.00	0.25–−0.16	95 860	20
	y	−4.91	2.63	−0.991	340	−26 580
Kr	yz	−0.011	−2.38	0.967	48 600	190
	ion	−0.101	−14.6	−0.23–0.53	85 630	310
	y	−4.91	10.2	−0.980	680	30 500
Xe	yz	0.020	11.0	−0.988	48 250	900
	ion	−0.128	−45.4	−0.35–−0.97	69 820	−2400

[a] The Rg–B distances are the estimated equilibrium values taken from DIM RDFs: 3.6 Å, 3.9 Å, and 3.8 Å for Ar, Kr, and Xe, respectively.

[b] The orbital Zeeman unit in Hartrees/Zeeman. Use conversion factor of 2.00 ($1/\mu_B$) to get Δg in ppm. The single value is obtained with center of mass gauge.

[c] The $X\,^2\Pi$–$A\,^2\Sigma$ energy separation corresponds to the averaged DIM value, where the ordering with respect to the diatomic fragments is reversed.

[d] In determining the sign note that the matrix elements are imaginary.

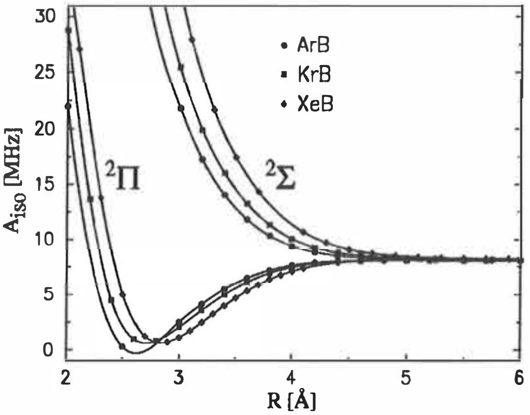

FIG. 3. The distance dependent isotropic hyperfine coupling values for the $X\,^2\Pi$ and $A\,^2\Sigma$ Rg–B states.

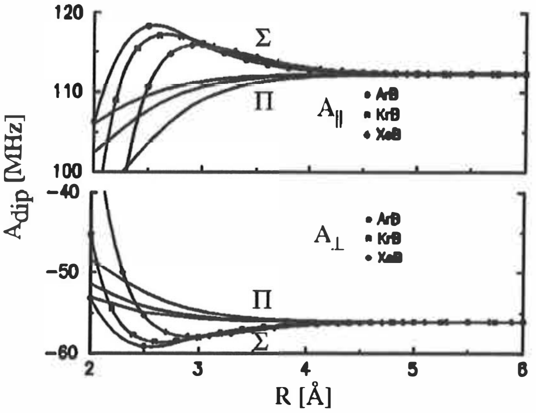

FIG. 4. The anisotropic spin dipolar hyperfine couplings as a function of Rg–B distance.

from c.m. by 1.0 Å toward B. If anything, this modest analysis reveals that the usual p-frame approximation is valid after all, provided the heavy-element effect is taken into account. Moreover, the predicted g shifts are rather sensitive to the RECP SO value. For KrB, the change in sign occurs already at 3.5 Å, where Kr contribution exceeds that of the B atom. Also note that the true situation involves interactions in $B(Rg)_n$ environment which means that the RECP contribution is to be multiplied by the number of nearest neighbors n.

D. Hyperfine properties

While the choice of the basis set and the correlation treatment is crucial for the FC contribution, the anisotropic dipolar part is only little influenced by the method. The chosen method converges towards the experimental A_{iso} value of 11.6 MHz for the B atom,[40] and already with the triple-zeta basis set quite accepted value of 8.0 MHz was obtained at the asymptote. This observation supports the use of this theory in computing the distance dependent $A_{iso}(R)$ curves reliably for Rg–B. The obtained $A_{iso}(R)$ curves are shown in Fig. 3 and they somewhat resemble the behavior of the Rg–B PECs in Fig. 1. As the FC term is a measure of s-wave character of the wave function, more precisely, its spin density at the magnetic nucleus, it is relatively straightforward to interpret these results. The spin density is perturbed, mainly due to polarization caused by spin-specific p-electron exchange interaction with α and β s electrons, so that in the parallel direction relative to the perturbation the spin density increases rapidly. On the other hand, perpendicular perturbation reduces the spin density. Actually, considering the shape of the $^2\Pi$-state curves, it is noticed that the position R_m at which the maximal negative shift in coupling occurs, is coincident with the electronic equilibrium distance R_e of RgB^+ ground states.[41] In a similar way as the dynamic electron correlation is responsible for the potential well before the repulsive forces start to dominate at short distances, the correlation and spin-polarization effects on the magnetic interaction switch their dominances as the orbital overlap enhances. This can be put in another way. Fernández and co-workers[42] have discussed the opposite signed effects for B_2 molecule in terms of core and valence contributions to the FC and SD values that are expressed as response and average matrix elements, respectively.

More detailed insights into the competitive effects may be obtained by comparing the above results to the present UHF calculation where only the positively signed polarization arises. The asymptotic UHF value for A_{iso} is too high by about 15 MHz but the $A_{iso}(R)$ curves follow a similar trend as obtained in the QCISD calculations. The representative ArB values $[R_m,\ A_{shift}(R_m),\ A_{iso}(R=\infty)]$ are (2.6 Å, −8.3 MHz, 8.0 MHz) and (3.1 Å, −7.0 MHz, 26.5 MHz) for QCISD and UHF, respectively. Therefore, it seems evident that the modified core polarization largely accounts for the shape of the $A_{iso}(R)$, whereas further electron correlation mainly has an effect in balancing the description and bringing the coupling to the right level of magnitude, although a pronounced shift to shorter distances in R_m is observed.

The anisotropic coupling terms, namely the principal axis components $-2A_{xx}=-2A_{yy}=A_{zz}$, show less marked dependence on the interatomic separation. The absolute values of both parallel (zz) and perpendicular (xx, yy) components begin to change identically as seen in Fig. 4. The calculations yield declining values from the asymptotic numbers of (−56.1, 112.2 MHz) to (−53.0, 106.0 MHz) for $^2\Pi$ state of ArB, notably between 4 to 2 Å. This only 5% deviation should be put in context with the drastic rise and fall of the isotropic terms. This directional dependence is closely related to the phenomena described for the isotropic case and reflected in Figs. 3 and 4.

III. DIM CALCULATIONS

A. Methods of the simulation

The molecular dynamics simulations presented here are based on evaluation of forces which originate from isotropic Rg–Rg and anisotropic Rg–B interactions. For this we have employed a low level DIM formalism in which the following matrix can be derived for p-orbital basis in laboratory $\{x,y,z\}$ frame:[43]

$$H^{\mathrm{DIM}}=\sum_{i<j} E(i,j)\otimes\mathbf{1}+\sum_i \begin{pmatrix} E_i(^2\Pi)+x_i^2\Delta_i & x_iy_i\Delta_i & x_iz_i\Delta_i \\ x_iy_i\Delta_i & E_i(^2\Pi)+y_i^2\Delta_i & y_iz_i\Delta_i \\ x_iz_i\Delta_i & y_iz_i\Delta_i & E_i(^2\Pi)+z_i^2\Delta_i \end{pmatrix}, \tag{2}$$

where $\Delta_i=E_i(^2\Sigma)-E_i(^2\Pi)$ and x_i, y_i, z_i denote the direction cosines between the ^2P atom and ^1S atoms. The sums count all the lattice atoms i and the calculated diatomic fragment states are used as input. $E(i,j)$ is the pair potential between ^1S atoms, whereas $E_i(^2\Sigma)$ and $E_i(^2\Pi)$ are the potentials asymptotically correlating with the ground state ^2P and ^1S atoms. The obtained 3×3 matrix is real and symmetric and is diagonalized numerically by the LAPACK[44] routine DSYEV. However, the numerical nature of this procedure complicates the calculation of forces as described in the following. Moreover, it should be noted that this approach holds rigorously only in absence of an external field when B has Kramers degeneracy, but in an external field the electronic states are further split. In principle, this would imply the DIM matrix to be six dimensional. However, in low external fields corresponding to an EPR experiment in the 9.5 GHz region, the magnitude of this effect is several orders of magnitude smaller than, e.g., spin–orbit splitting, and is consequently omitted.

The calculated adiabatic potentials were parametrized according to the function

$$V(r)=ae^{-br}+\frac{c}{r^{12}}-\frac{d}{r^6}-\frac{f}{r^8}, \tag{3}$$

where r is the internuclear distance and a,b,c,d,f are least-squares-fitted parameters specific to the interacting pair. For the Rg–Rg pair potential the atomic forces can be easily obtained by differentiating Eq. (3) and applying the chain rule for converting to the Cartesian coordinates. For the anisotropic part involving matrix diagonalization process, analytic differentiation

$$\frac{\partial E}{\partial q}\approx C^T\frac{\partial H}{\partial q}C \tag{4}$$

of the DIM Hamiltonian matrix elements with respect to coordinates q is exact in a mathematical sense, but it assumes that the DIM basis functions change only slowly compared to Hamiltonian change with nuclear motion. Here, E is the lowest energy eigenvalue and C the corresponding eigenvector. On the other hand, a semianalytic approach where the derivative of $^1S-^1S$ part is expressed analytically and the $^1S-^2P$ part by the central difference approximation is, in principle, exact with respect to the DIM procedure. However, the semianalytic method which, for short, loops over lattice atoms within a cutoff radius of 8.0 Å around the impurity and calculates the $^1S-^2P$ force pairwisely by moving the ^1S atom, requires 6×(number of atoms within cutoff) matrix diagonalizations. The results of both the above-described gradient methods turned out equally accurate, thus the substantially faster analytic method was used throughout this study.

The potential inputs used in the simulations were those of the subsequent coupled-cluster study where the fitting parameters are also given.[20] We have utilized computed potentials also for the Rg–Rg interaction. The advantage of this choice is that it allows to use a single scaling factor (1.2) for the energies and, moreover, it yields more balanced (unbiased) lattice structures. The scaling factor arises from ca. 20% error in the calculated dissociation energies.[20]

The MD simulations were carried out in a microcanonical (NVE) ensemble starting with a face-centered-cubic (FCC) crystal structure and the ^2P atom issued as a substitutional impurity. A total of 256 atoms, or less when one or two nearest-neighbor vacancies were introduced in the lattice, were included in the simulations and periodic boundary conditions were imposed. The numerical integration of the classical equations of motion was implemented according to the "velocity Verlet" algorithm[45] with a time step of 0.3 fs. The simulation consisted of two stages. First, the system was subject to simulated annealing 30 K (1.5 ps)→20 K (1.5 ps)→10 K (3 ps) during which thermalization was obtained using velocity scaling. Second, the main simulation at 10 K was carried out for 30 ps during which the system strictly obeyed the NVE conditions, and all the ensemble averages were collected. Radial distribution functions (RDF) around the impurity were computed and the three energy eigenvalues and eigenvectors as a result of the DIM Hamiltonian diagonalization were stored at each time step. The orbital autocorrelation function defined as

$$C_i=\langle c_i(t)\cdot c_i(0)\rangle, \tag{5}$$

where $c_i(t)$ denotes the ith eigenvector, was used for studying the rotation of the p-orbital frame. The beginning of the second simulation stage was chosen for the $t=0$ moment. Since the vacancies were issued within the same cubic unit shell as the impurity, the occupied p orbital tends to get locked towards the cavity. The above correlation function is a convenient way to illustrate this matter.

An obviously severe shortcoming of the above classical treatment is the neglect of the zero-point motion in the simulation. Since all pair interactions in the given systems are only weakly bound the zero-point energies are expected to be small. On the other hand, the shallow potentials may lead to zero-point amplitudes which are comparable to the thermal classical motions. Consequently, the classical treatment might undersample the configuration space by some extent. A practical implication of such deficiency would be the narrower Franck–Condon region for optical transitions as discussed in the following paper.[20] Inspection of classical trajectories showed extensive motion of boron over the entire cage volume, thus the neglect of zero-point amplitudes does not seem like a serious matter.

Assuming pairwise additivity, the anisotropic hyperfine coupling can be calculated along with the DIM simulation. The three components of the **A** matrix, diagonal in p-orbital frame, are collected during a simulation step by using the DIM eigenvectors to define the directional contributions as follows:

$$A_j = \sum_{i=1}^{n} \sum_{k=1}^{3} (d_i \cdot c_k)^2 a^{kj}(r_i), \quad j=1,2,3, \tag{6}$$

where d_i is the direction cosine of the line joining B and Rg atom i relative to the laboratory frame, c_k is the kth DIM eigenvector, and $a^{k,j}$ contains the distance dependent FC and SD hyperfine (shifts from free atom) data. The appropriate value is extracted by linear interpolation. For example, the contribution to the direction of first eigenvector, say $^2\Sigma$, is summed into array A for one interacting pair as follows:

$$\begin{aligned} A_1 = {} & (d \cdot c_1)^2 a(\Sigma_{zz};r) + (d \cdot c_2)^2 a(\Pi_{yy};r) \\ & + (d \cdot c_3)^2 a(\Pi_{xx};r), \end{aligned} \tag{7}$$

showing the state dependency of the $a^{k,j}$. The data in $a^{k,j}$ file is arranged in such a way that the dependence of the indices remains consistent for all j. After summing over all the nearby lattice atoms i, the free B atom $A_{\perp,\parallel}$ *ab initio* values and the experimental A_{iso} value of 11.6 MHz were added to this array. Next, the matrix **A** having the above array values in the diagonal is brought into the fixed reference frame of laboratory by similarity transformation $\mathbf{CAC}^{-1}$, where **C** is constructed from the three DIM row eigenvectors acting as a Cartesian rotation matrix. This is necessary since the p-orbital orientation obviously changes during the simulation.

The cutoff value of 8.0 Å has been used also for the hyperfine interaction and the above procedure was carried out at every tenth simulation step. The **A** matrix was averaged in the laboratory frame over the simulation period (second stage) and finally diagonalized to yield the parallel and perpendicular hyperfine components perturbed by the lattice.

TABLE II. The DIM eigenenergies (in meV) from 30 ps simulations for scaled and nonscaled cases with different number of lattice vacancies.

		Not scaled			Scaled		
Rg	E_n	no vac	1 vac	2 vac	no vac	1 vac	2 vac
Ar	1	−133.0	−134.2	−131.7	−159.2	−161.3	−158.0
	2	−112.0	−86.1	−88.6	−134.2	−104.0	−106.7
	3	−100.5	−69.8	−65.0	−121.1	−84.2	−79.7
Kr	1	−169.6	−164.8	−157.5	−203.5	−198.1	−189.1
	2	−156.6	−135.3	−125.0	−188.0	−163.4	−150.8
	3	−147.3	−123.5	−110.2	−177.5	−149.6	−134.4
Xe	1	−178.9	−167.2	−157.3	−214.3	−200.7	−189.3
	2	−170.7	−127.3	−138.5	−204.7	−143.1	−165.2
	3	−162.6	−91.4	−124.3	−195.4	−90.2	−150.8

B. Simulation results

The stability of the simulation was inspected by several ways. First, five different test runs for one and two vacancy cases in Ar matrix were performed with excessive simulated annealing starting from 80 K. All the trajectories yielded similar energy eigenvalues, hyperfine matrices, and total energies implying that the global minimum was achieved. In addition, the algorithmic stability was reflected in that prolonged simulation times revealed no accumulating errors as indicated by constant temperature. Finally, possible lattice strain caused by the impurity atom was followed by recording the internal virial energy of the system and adjusting the periodic boundary box-size accordingly. All the Cartesian force components were found to be fluctuating around zero as well. These observations together indicate relaxed lattice structures. The results obtained in the simulation, i.e., energy eigenvalues and hyperfine components as presented in the following paragraphs, were further averaged over three separate simulation runs. Again, rather similar values for these properties were obtained from different trajectories indicating the adequacy of rather limited statistics.

The results of the simulations were somewhat influenced by the applied energy scaling. Most notably, of course, the 20% scaling affected the eigenenergies by lowering them, respectively, but the energy separations (ΔE) obeyed the same rare gas dependence as without scaling. As a result, the ΔE values were somewhat larger. The results are collected in Table II. The effect of vacancies on the p-orbital orientation can be seen in Fig. 5. For Ar lattice, without vacancies, the orbital frame rotates freely and loses its memory of the initial orientation in a picosecond time scale. However, with a single nearest-neighbor vacancy one of the eigenvectors (z) becomes locked and the others (x,y-frame) rotate, and for the two-vacancy case the whole frame is fixed 80% although the xy-wobbling occasionally crosses the potential barrier. This analysis shows that the axial symmetric environment is clearly produced by one vacancy, and also by two vacancies if the longer response time of the experiment is considered. In Kr the difference between one and two vacancy cases is not so distinct as the xy-frame rotates relatively freely even in the presence of two vacancies. Xe lattice is similar to Ar but the effect of one and two vacancies is reversed. The orbital locking is effective already in the one-vacancy case and an additional cavity loosens the orbital motion. It can be observed from the c-labeled portion of the lowest panel in Fig. 5 that also the lowest eigenvector occasionally turns away from its initial position. Therefore, we tabulate the results only for one- and two-vacancy cases since the perfect lattice is ruled out by symmetry arguments. Moreover, we note that the correlation functions represented in Fig. 5 involve energy scaling and are from single simulation runs. However, these results are insensitive to the scaling and are reproduced in all the computed trajectories. Further information on lattice structures can be gained from the RDFs shown in Fig. 6. One- and two-vacancy cases appear similar to each other both in Ar and Kr, whereas in Xe the curves differ markedly. Also, the distinct shoulder in the first peak at 4 Å corresponding to pair potential (X, A) minima fades out in Xe.

As will be discussed in the next section, the DIM energy eigenvalues are utilized in determining the crystal field parameters. The results are collected in Table III. If one uses

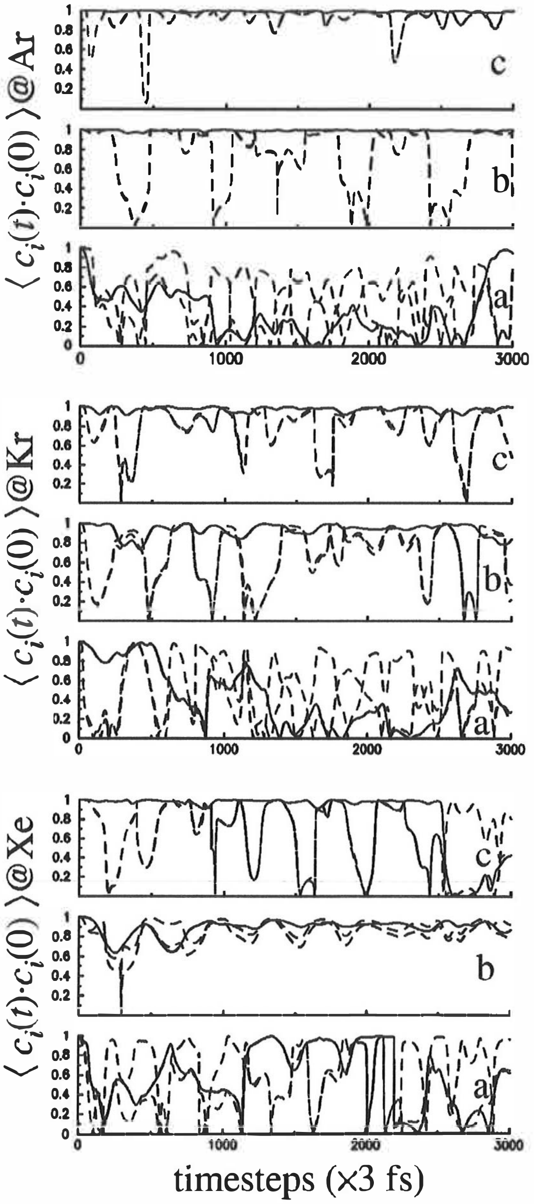

FIG. 5. The boron $2p$-orbital time correlation functions (absolute values) in Rg hosts. (a) No vacancies, (b) one vacancy, (c) two vacancies issued. The solid line corresponds to the eigenvector of the lowest energy and the dashed lines stand for the xy frame.

the single-vacancy case for Ar and Kr and the two vacancy case for Xe, then descending trend in energy separation and therefore in CF parameters is obtained. This is opposite to the initial hypothesis of enlarging orbital splitting with the increasing Rg polarizability. It is an implication of Rg–B/Rg–Rg balance effects on the structures. The PECs show that whereas the Rg–B equilibrium distances are relatively similar in different host lattices, the lattice constants vary significantly. There appears now to be two factors that suggest the use of the two-vacancy case for the Xe lattice. We carry on, however, by representing both the one- and two-vacancy results for the hyperfine matrix components, and collect them in Table IV. As a reminder, the matrix contains both the perturbed FC and SD interactions $(\mathbf{A}=A_{\mathrm{iso}}\mathbf{1}+\mathbf{A}_{\mathrm{dip}})$ although the direction is indicated by A_{dip} only. These values reflect directly what was discussed in the context of correlation functions above. The slight reduction in the parallel component compared to the free atom arises from minor "z-vector" swaying, that is, the obtained value is a projected resultant on the z axis. The enhanced orbital locking is seen in Ar and Kr where the parallel components are larger in the two-vacancy cases. The results for Xe are again distinct from the other two host lattices as axial symmetry is nearly lost in more freely tumbling. The results indicate, however, that the hyperfine structure should be rather similar in all hosts, aside from the heavy-element effects in g-tensor shifting that may invert the whole spectrum.

So far, we have neglected a trapping configuration which, although distinct in character compared to the three substitutional cases treated here, may bear some importance when considering possible lattice environments of the experiment. That is, an impurity atom trapped in an interstitial

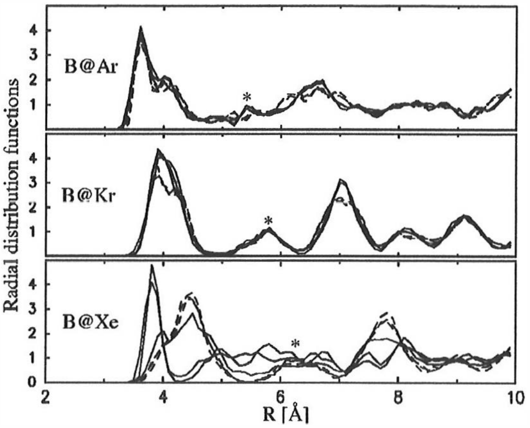

FIG. 6. The RDFs for three DIM trajectories in each matrix with one (solid line) and two (dashed line) vacancies. The asterisks (*) indicate the FCC lattice constants.

TABLE III. The DIM energy separations $(\Delta E_{zx},\Delta E_{zy})$ in meV and the corresponding averaged crystal field parameters (Δ_1) in cm^{-1}.

		1 Vacancy		2 Vacancies	
Rg	d	ΔE_{zd}	Δ_1	ΔE_{zd}	Δ_1
Ar	x	−77.1	361.3	−78.4	348.7
	y	−57.3		−51.3	
Kr	x	−48.5	223.8	−54.7	249.9
	y	−34.7		−38.3	
Xe	x	−110.4	451.8	−38.5	168.3
	y	−57.6		−24.1	

cavity. Among these the octahedrally symmetric site is the least repulsive initially. As this additional 257 atom case was explored separately, we refer to the subsequent paper[20] for corresponding RDFs and discussion on structural details, and give briefly the results. First, the favorable orbital locking, that was seen with one and two vacancies above, is most pronounced here. The energetics is, however, very different as seen in Table V where we collect all the values resulting from this simulation. It is immediately seen that in Ar the interstitial trapping does not result in favorable **A** tensor parameters. Quite opposite is the case in Kr and Xe, however, where strictly axially symmetric data is obtained. This is accompanied with relatively large negative shift in $A_\perp$, that can be rationalized by consulting the Figs. 3 and 4, and considering the nearest-neighbor distances. At these interatomic distances the heavy-element effect takes a strong part in Δg, as the sign change appears already with one B–Kr pair.

We now proceed to define the spectrum simulation method and produce synthetic EPR spectra by utilizing the above-obtained information and compare the results in the experimental section.

IV. NUMERICAL EPR SPECTRUM SIMULATION

^2P atoms trapped in environments where the equivalence of the p orbitals is lost produce anisotropic spectrum both in electron spin coupling to the nuclear spin and to the field B (nonisotropic **A** and **g** matrices). For the numerical simulation of this situation our software[46] uses the following effective Hamiltonian (neglecting nuclear quadrupole effects and assuming isotropic nuclear Zeeman interaction):

$$\mathcal{H}^{\mathrm{eff}}=\mu_B\mathbf{B}(g_e\mathbf{S}+\mathbf{L})+\zeta\mathbf{L}\cdot\mathbf{S}+\mu_N\mathbf{B}g_I\mathbf{I}+\mathbf{S}\cdot\mathbf{A}\cdot\mathbf{I}+\mathcal{H}_{ttgl}(L), \tag{8}$$

where the orbital contributions, i.e., orbital Zeeman and one-electron spin–orbit terms, usually embedded to spin–Hamiltonian type tensoral form (spin–Zeeman term $\mu_B\mathbf{B}\cdot\mathbf{g}\cdot\mathbf{S}$) are explicitly shown. Here, g_e is the free electron g value, g_I is the nuclear g value, μ_B and μ_N are the Bohr and nuclear magnetons, respectively, and ζ is the atomic spin–orbit coupling constant which sign is assigned for electron or electron-hole type species. The vectoral operators are $\mathbf{S}=(S_x,S_y,S_z)$ for electron spin, $\mathbf{I}=(I_x,I_y,I_z)$ for nuclear spin, and $\mathbf{L}=(L_x,L_y,L_z)$ for orbital angular momentum. **A** is the diagonal hyperfine matrix and the last term is responsible for crystal field effects. The crystal fields (octahedral or tetrahedral+tetragonal distortion) of intermediate strength are defined in the operator representation ($\mathcal{H}_{ttgl}(L)=\mathcal{H}_{oct}+\mathcal{H}_{ttgl,d}$) as follows:[47,48]

$$\mathcal{H}_{oct}=\frac{\beta_c}{20}[35L_z^4-30\mathbf{L}(\mathbf{L}+1)L_z^2+25L_z^2-6\mathbf{L}(\mathbf{L}+1)\mathbf{1}+3\mathbf{L}^2(\mathbf{L}+1)^2\mathbf{1}]+\frac{\beta_c}{8}[L_+^4+L_-^4], \tag{9}$$

$$\mathcal{H}_{ttgl,d}=\alpha_t[3L_d^2-\mathbf{L}(\mathbf{L}+1)\mathbf{1}],\quad d=x,y,z.$$

The crystal field parameter is denoted by β_c and α_t is the three component tetragonal distortion parameter. In the present case, only α_t causes separation of the p-orbital energies and therefore β_c is set to zero. Here we have a positive α_t applied in the z direction, so the following relations prevail: $3\alpha_{t,x}=\Delta E_{zx}$, $3\alpha_{t,y}=\Delta E_{zy}$, $\alpha_{t,z}=0$. The usually applied CF parameter Δ is now defined as $\alpha_t=-\Delta/2$. **1** is the identity operator (24×24 unit matrix).

By choosing the basis set as a product of the spin states $|m_l m_s m_I\rangle$ the corresponding Hamiltonian matrix was formed. This Hermitian matrix was diagonalized numerically by the LAPACK[44] routine ZHEEV. Unfortunately, in EPR experiments the magnetic field strength is swept instead of the microwave frequency. The energy levels do not necessarily behave linearly as a function of the field strength and as a consequence the Hamiltonian should be diagonalized at every field value used in the experiment. This is obviously impractical due to excessive computational demand thus various methods, from linear approximation of the field dependence to iterative search of the exact transition fields, have been suggested to overcome this problem.[49] We have approximated the transition magnetic field values by performing linear interpolation within some given number of points at which the Hamiltonian was diagonalized. In a similar way the transition moments between the given eigenlevels were evaluated. Typically, we used 40 points distributed over the 40 mT spectral region. A spline interpolation could, in principle, be applied in this process but would require eigenvector storage for all field values at which the diagonalization is performed.

When the system has orientation dependent parameters, such as an anisotropic crystal field or anisotropic hyperfine coupling and trapping occurs in random directions with respect to the magnetic field, one has to integrate single crystal EPR spectra over the spherical angles to obtain the corresponding powder spectrum. However, in the present case we may mostly restrict ourselves to axial symmetric systems, where the integration is performed over one angle (polar) only. Even in this case the number of matrix diagonalizations grows quickly as the accuracy of the powder integration is increased. We have used cubic spline interpolation to speed up the quadrature in all cases, and when integrating over the spherical octant, have applied a regular 40×40 point mesh.

While interpolating, either in magnetic field strength or magnetic field direction, crossings of the energy levels may confuse the process. In practice, the interpolating scheme may correlate wrong energy levels together. This problem obviously vanishes as the number of interpolation points increases but on the expense of efficiency. To overcome this problem we have constructed a tracking procedure where the magnetic field strength and direction correlation functions are calculated. This is essentially Eq. (5) with time replaced by field strength or direction. This correlation function can be used for locating the matching eigenstates within the interpolation region.

The above procedure yields a stick spectrum which is then convoluted with the Lorentzian line shape function in the Fourier space. Once the powder EPR spectrum is efficiently simulated it can then be fitted to the experimental one

TABLE IV. The anisotropic hyperfine coupling constants (in MHz) for boron resulting from DIM simulations in Rg matrices.

Rg	A_{dip}	1 Vacancy	2 Vacancies
Ar	$\parallel$	119.7	120.0
	$\perp$	−47.5	−47.8
	$\perp'$	−46.7	−47.0
Kr	$\parallel$	116.2	121.7
	$\perp$	−42.4	−44.3
	$\perp'$	−37.7	−43.5
Xe	$\parallel$	117.7	100.3
	$\perp$	−46.8	−36.3
	$\perp'$	−43.6	−26.0

by varying the parameters of Eqs. (8) and (9). Since the least-squares gradient is not available for this process Monte Carlo and simplex based methods were used.[50]

V. EXPERIMENTAL SECTION

A. Measurements

Boron atoms were produced in the gas phase by focusing a 308 nm XeCl excimer laser (Estonian Academy of Sciences, ELI-94) beam into a solid boron target with a quartz lens (20 cm focal length). Typical laser pulse energy was 6 mJ/pulse. The boron target was placed in the vacuum chamber of a closed cycle helium cryostat (APD Cryogenics, DE202A) suitable for EPR measurements as described elsewhere.[51,52] During the vaporization process the boron target was flushed with rare gas stream and the resulting rare gas–boron mixture was subsequently deposited onto a flat copper target held at 12 K. Typical gas deposition (ca. 100 mbar from a 1-l container) time was 80 min with 10 Hz laser repetition rate. All EPR measurements were performed at the lowest accessible temperature of 12 K. The EPR spectra were obtained with Bruker ESP-300 series X-band spectrometer with 100 kHz field modulation. The microwave frequency and magnetic field strength were monitored with a microwave frequency counter (Hewlett-Packard 5350B) and a NMR gaussmeter (Varian E-500), respectively.

Boron of natural isotopic abundance ($^{11}B=80.4\%$ is of interest here; $^{10}B=19.6\%$) with purity of 99% was obtained from Aldrich Chemicals Co. and was held under nitrogen atmosphere in order to avoid oxidation. Ar (99.999 90%), Kr (99.997%), and Xe (99.997%) were obtained from AGA. The present spectral impurities, that is, visible CH_3, ^1H, and BO lines, originate possibly from decomposed hydrocarbons and oxygen in the plasma. It should be noted that these are practically impossible to get rid of and that EPR detection is very sensitive for these because their isotropic spectra. Traces of small boron clusters such as B_2 and B_3 were observed only with high photon fluencies of the ablation laser or as thermal reaction products in annealed matrices, and did not disturb the spectral analysis.

B. The EPR spectra

The quality of the measured spectra suffers from the inevitable methyl radical impurity generated during laser ablation. The precursor for CH_3 is not clear and attempts to completely avoid this impurity failed. Fortunately, this intensive and narrow spectral feature does not complicate the present analysis too much. As a starting point for fitting, it was convenient to first set the $A_\parallel$ and then proceed with the rest of the parameters by adjusting the distinct high-field feature (in Ar, low field in Kr) that is due to the nearly coincident, $A_\parallel$ and $A_\perp$ peaks as seen in the Fig. 7. The difficulty lies, however, partly in that the other three broadened $A_\perp$ lines are not resolved in the spectra. This makes the determination of the perpendicular coupling strengths more putative. In the fitting we have followed the interpretation by Graham and Weltner[15] in which axial symmetry is assumed. This means that a single valued $\Delta_\perp$ was optimized while the atomic spin–orbit parameter ζ was kept constant. In contrast, in order to utilize our theoretical results we have also used an approach, where the averaged CF parameter was the value suggested by the DIM simulations, and the effective spin–orbit coupling was varied accordingly. The clear outcome of the heavy-element effect is seen in that the Kr spectrum is reversed with respect to Ar, that is, $g_\perp > g_\parallel$ and, consequently, the phase of the parallel transitions is turned around. This was simulated by changing the sign of the variable ζ. Figure 7 shows the experimental spectra in Ar and Kr solids overlaid with the simulated spectra obtained by both methods of fitting and applying axial symmetry. The results are

TABLE V. Theoretical data involving intestitial trapping of boron. DIM-simulated energies (E_n, ΔE, $\Delta_\perp$) and hyperfine tensor (A_{dip}) along with the second order contributions to the g tensor.

	E_n (meV)	ΔE_{zd} (meV)	$\Delta_\perp$ (cm^{-1})	A_{dip} (MHz)		SO_x (cm^{-1})[a]	SO_x^{ecp} (cm^{-1})[a]	L_x (a.u.)[a]	ΔE (cm^{-1})	$\Delta g_\perp$ (ppm)
	−61.0	−249.5	959.3	$\parallel$	95.0	4.91	−1.41	0.984	1440	−9580
Ar	46.3	−107.3		$\perp$	−51.4					
	188.5			$\perp'$	−30.0					
	−65.3	−224.7	1111.7	$\parallel$	122.2	−4.91	9.14	−0.970	1670	9840
Kr	123.5	188.8		$\perp$	−51.9					
	159.4			$\perp'$	−51.7					
	−103.7	−272.1	1358.2	$\parallel$	123.1	−4.91	32.55	−0.933	2040	50620
Xe	129.4	−233.1		$\perp$	−52.1					
	168.4			$\perp'$	−52.0					

[a] The values correspond to 3.3 Å Rg–B distances.

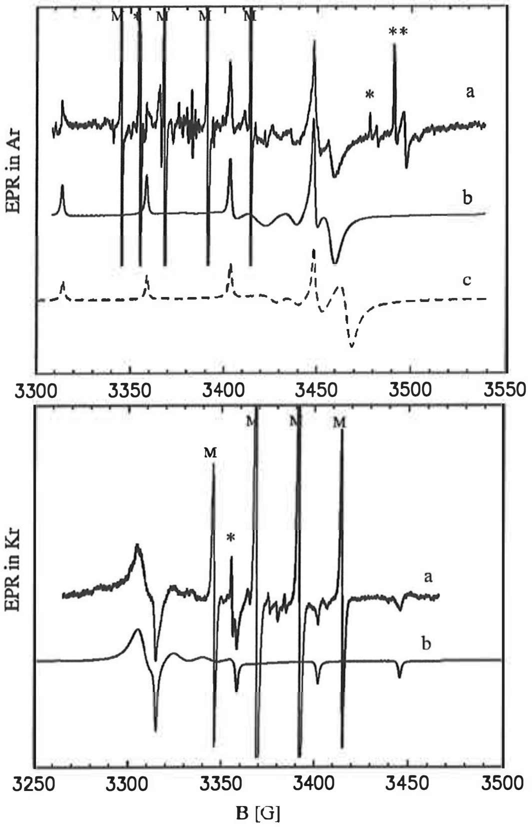

FIG. 7. EPR spectra of ^{11}B atoms in solid Ar and Kr: (a) experimental, (b) axially symmetric simulation, (c) simulation with parameters from Ref. 15. The impurity methyl quartets are indicated by M, and lines due to ^{10}BO (*) and ^{11}BO (**) are also marked ($10\,G=1\,mT=g/g_e$ 28.025 MHz).

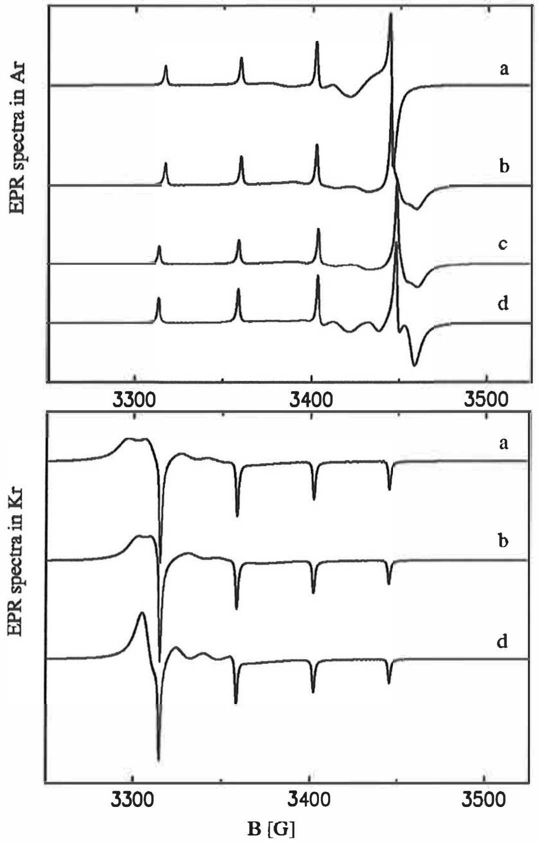

FIG. 8. The simulated EPR spectra using theoretically predicted values (1 vacancy case for Ar and two vacancies for Kr): (a) purely theoretical, (b) ζ adjusted, (c) $A_\parallel$ adjusted, (d) the fitted spectrum that has axially symmetric hyperfine and crystal field values.

collected in Table VI. From the lowest trace in the Ar spectra one sees that the considerably smaller $A_\perp$ parameter given by Graham and Weltner[15] yields somewhat better fit for the blurred feature at 3430–3440 G. Also in Kr fitting of the 3320–3330 G region would necessitate $A_\perp$ coupling below 30 MHz, which seems too small compared to the theoretical prediction.

It should be noted that it was possible to obtain a fit of comparable accuracy with a nonaxial crystal field. This is demonstrated next by synthetizing theoretical spectra with the DIM-simulated parameters from Tables I, III, and IV. Note also that the calculated heavy-element effect was large enough to produce the observed flip to a positive g shift when the number of pair-additively contributing atoms (4) was estimated from the RDFs. Therefore, in Ar the ζ value becomes $2\times(4.91-4\times0.64)=4.7\,\mathrm{cm}^{-1}$, whereas in Kr the outcome is $\zeta=-5.6\,\mathrm{cm}^{-1}$. The upmost spectra in Fig. 8 thus correspond to purely theoretical simulation. Next, we have relaxed the constraint on ζ to mimic the experiment more

TABLE VI. The EPR spectral parameters for B atom isolated in Rg matrices as obtained from the fitting of the experimental spectra in the axial framework using theoretical prediction as a starting point. For Xe matrix, ζ was the only adjustable parameter.

Rg	Method	$A_\parallel$ (MHz)	$A_\perp$ (MHz)	$g_\parallel$	$g_\perp$	ζ (cm^{-1})	$\Delta_\perp$ (cm^{-1})
Ar	Varied SO/CF	126.1	−46.9	2.0014	1.970	7.76/10.16	361.2/480
	Ref. 15	126	−33	2.0014	1.965	10.67	380
Kr	Varied SO	122.3	−44.9	2.0018	2.032	−4.72	223.8
Xe	2 Vacancies	100	−26, −36	2.002	2.10	−11.4	168.3

closely, and finally adjusted the $A_{\parallel}$. Comparison with the lowest axially fitted trace suggests that the dynamics simulation fails partly while producing a slightly nonaxial crystal field which is not supported by the experiment. A close inspection of these figures shows that the measured B atom spectra in Ar and Kr hosts is indeed strictly axial. Also, as the $A_{\parallel}$ needs to be corrected upwards it can be concluded that either the orbital frame is more strictly oriented than predicted by the simulations or already the free atom *ab initio* value is too small by a few MHz. The spin–orbit energetics follows quite closely what is predicted by the theory as already discussed. It is, furthermore, shown that this can be handled by the effective parameter ζ with sign convention. Since the value of $A_{\perp}$ is hard to determine, moreover, it has to be uniquely defined (axial A) in Ar and Kr, the accuracy of $g_{\perp}$ is difficult to quantify.

While the above analysis cannot be simplified for Ar by considering interstitial trapping, the simulation in Kr becomes more straightforward. The $A_{\parallel}$ hits the correct 122 MHz value immediately, and by using $\Delta_{\perp}$ of 1111.7 cm^{-1} with spin–orbit value of $-22.5\ \mathrm{cm}^{-1}$ we have a remarkably good fit. If we consider the SO value as an outcome of relation $2\times(4.91-n\times9.14)\ \mathrm{cm}^{-1}$, we get the effective number of nearest neighbors n to be 1.8. This seems a bit small since the actual simulated trapping site consisted of four nearly equally spaced nearest neighbors in the xy plane including the impurity atom.[20] Nevertheless, the results for effective ζ or n values derived above in Ar and Kr with substitutional trappings did not quite correspond to simulated structures either. In particular, the n values were 1.6 and 2.8, respectively. We are not, however, too worried about this discrepancy, since the qualitative picture is as clear as it can be without more accurate experimental knowledge on the magnitude of $A_{\perp}$.

From the above discussion it seems reasonable to accept the concept of pair additivity also when considering the g shift. This was already employed by Adrian[53] for trapped H atoms, where he used an expression for Δg that included the sum over the n nearest-neighbor matrix atoms. In this respect, provided that one has rigorous gauge invariant quantities calculated for pairs, it could be possible to simulate the g-shift variation by molecular dynamics similarly as done for hyperfine parameters here.

Another feature evident in the spectra is the different linewidths (LW) for parallel and perpendicular lines, namely $\mathrm{LW}_{\parallel}:\mathrm{LW}_{\perp}=1:7$ in Ar and$=1:9$ in Kr. In the following we adapt the discussion by Du *et al.*[54] The unpaired electron in B is in an orbital that is predominantly p_z, and the g anisotropy is due to spin–orbit coupling. When magnetic field is along the z axis, this adds no contribution to the first order wave function. In the perpendicular plane, the SO coupling adds a contribution from $p_{x,y}$ which has the opposite electron spin state as that of the p_z. Since spin-lattice relaxation requires a change in electron spin state, vibrations in the x, y plane that modulate the SO coupling may have more impact on relaxation than vibrations along the z axis, therefore having a broadening effect on $A_{\perp}$ lines.

Finally, in Fig. 9 we show the spectra measured in Xe solid along with the corresponding synthetic simulations. The broad lump at 3200 G is tentatively assigned to $g_{\perp}$ transition of boron. This assignment is based on the disappearance of the resonance upon annealing, which reveals the $H_2{}^{11}BO$ spectrum $[g=2.0075, A(\mathrm{H})=375.8\ \mathrm{MHz}, A(\mathrm{B})=87.6\ \mathrm{MHz}]$ due to thermally mobilized B atoms. In the attempt to simulate this we used the predicted values for the two-vacancy case, having the averaged value for the crystal field and nonaxial $A_{\perp}$ and $A_{\perp}'$. This procedure yielded an effective SO parameter of $-11.4\ \mathrm{cm}^{-1}$. Unfortunately, due to the extreme broadness of the observed resonance, it is not feasible to distinguish between different trapping sites, although the computed $A_{\parallel}$ values for the one- and two-vacancy cases differ significantly.

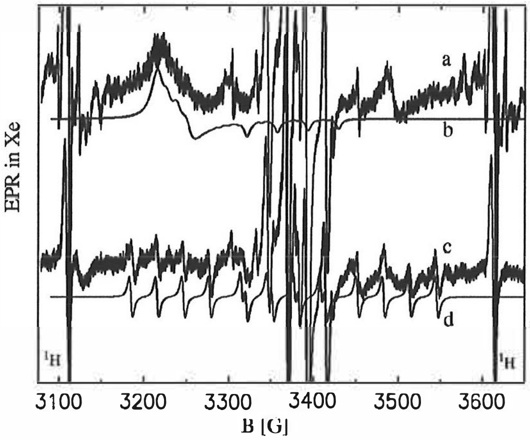

FIG. 9. EPR spectra of B in Xe matrix: (a) experimental at 12 K, (b) simulation with parameters derived from theory, (c) experimental at 50 K, (d) the simulated spectrum of thermally formed $H_2{}^{11}BO$. The impurity ^1H doublets are also shown.

VI. SUMMARY

Although it is shown here that the classical textbook example of a "p electron in crystal field" model fails as it is originally formulated, by using ζ as variable parameter possessing both signs due to the heavy-element effect and not by referring to an electron-hole type situation, it was possible to interpret the measured boron atom EPR spectra in rare gas solids. While the B atom spin–orbit coupling remains practically intact in the course of matrix perturbations, mixing of the Rg character into the wave function comprises from-closed-to-singly-occupied excitations that have an oppositely signed contribution to the g tensor. The DIM theory used in the study served two purposes in addition to the adiabatic dynamics it allowed. The eigenenergy separation was used as crystal field–excitation energy parameter in the g-tensor evaluation. Second, the hyperfine coupling based on the calculated pair interactions was also included in the simulation and the dependence on the electronic coordinates were obtained by using the DIM eigenvectors. By combining experiment and theory, more accurate B atom hyperfine parameters were derived for the Ar matrix, new data presented for the Kr matrix with similar accuracy as in Ar, and tentative assignment for Xe host was suggested. In addition, the trapping site structures were shown to necessarily have one or two vacancies nearby the embedded B atom in order to create an environment favorable to magnetic detection. Although, in Kr interstitial trapping was also effective in producing this strict axial symmetric situation.

ACKNOWLEDGMENT

This study was funded by the Academy of Finland.

[1] F. O. Ellison, J. Am. Chem. Soc. **85**, 3540 (1963).

[2] J. C. Tully, J. Chem. Phys. **93**, 1061 (1990).

[3] I. H. Gersonde and H. Gabriel, J. Chem. Phys. **98**, 2094 (1993).

[4] N. L. Doltsinis and P. J. Knowles, Chem. Phys. Lett. **325**, 648 (2000).

[5] J. A. Boatz and M. E. Fajardo, J. Chem. Phys. **101**, 3472 (1994).

[6] A. I. Krylov, R. B. Gerber, and V. A. Apkarian, J. Phys. Chem. **189**, 261 (1994).

[7] A. I. Krylov and R. B. Gerber, Chem. Phys. Lett. **231**, 395 (1994).

[8] A. I. Krylov, R. B. Gerber, M. A. Gaveau, J. M. Mestdagh, B. Schilling, and J. P. Visticot, J. Chem. Phys. **104**, 3651 (1996).

[9] P. Jungwirth and R. B. Gerber, J. Chem. Phys. **104**, 5803 (1996).

[10] A. I. Krylov, R. B. Gerber, and R. D. Coalson, J. Chem. Phys. **105**, 4626 (1996).

[11] V. A. Apkarian and N. Schwentner, Chem. Rev. **99**, 1481 (1999).

[12] W. Weltner, Jr., *Magnetic Atoms and Molecules* (Dover, New York, 1983).

[13] L. B. Knight and W. Weltner, Jr., J. Chem. Phys. **55**, 5066 (1971).

[14] J. H. Ammeter and D. C. Schlosnagle, J. Chem. Phys. **59**, 4784 (1973).

[15] W. R. M. Graham and W. Weltner, Jr., J. Chem. Phys. **65**, 1516 (1976).

[16] H.-J. Werner and P. J. Knowles, J. Chem. Phys. **89**, 5803 (1988).

[17] P. J. Knowles and H.-J. Werner, Chem. Phys. Lett. **145**, 514 (1988).

[18] H.-J. Werner and P. J. Knowles, J. Chem. Phys. **82**, 5053 (1985).

[19] P. J. Knowles and H.-J. Werner, Chem. Phys. Lett. **115**, 259 (1985).

[20] T. Kiljunen, J. Eloranta, J. Ahokas, and H. Kunttu, J. Chem. Phys. **114**, 7157 (2001), following paper.

[21] M. R. A. Blomberg and P. E. M. Siegbahn, J. Chem. Phys. **78**, 5682 (1983).

[22] A. Berning, M. Schweizer, H.-J. Werner, P. J. Knowles, and P. Palmieri, Mol. Phys. **98**, 1823 (2000).

[23] MOLPRO is a package of *ab initio* programs written by H.-J. Werner and P. J. Knowles, with contributions from R. D. Amos, A. Bernhardsson, A. Berning *et al.*

[24] R. A. Kendall, T. H. Dunning, Jr., and R. J. Harrison, J. Chem. Phys. **96**, 6796 (1992).

[25] A. Nicklass, M. Dolg, H. Stoll, and H. Preuss, J. Chem. Phys. **102**, 8942 (1995).

[26] T. Kiljunen, J. Eloranta, and H. Kunttu, J. Chem. Phys. **110**, 11814 (1999).

[27] A. Nicklass, K. A. Peterson, A. Berning, H.-J. Werner, and P. J. Knowles, J. Chem. Phys. **112**, 5624 (2000).

[28] D. E. Woon and T. H. Dunning, Jr., J. Chem. Phys. **103**, 4572 (1995).

[29] E. R. Davidson, Chem. Phys. Lett. **260**, 514 (1996).

[30] J. E. Harriman, *Theoretical Foundations of Electron Spin Resonance* (Academic, New York, 1978).

[31] R. McWeeny, *Methods of Molecular Quantum Mechanics*, 2nd ed. (Academic, London, 1992).

[32] G. H. Lushington, P. Bündgen, and F. Grein, Int. J. Quantum Chem. **55**, 377 (1995).

[33] G. H. Lushington and F. Grein, J. Chem. Phys. **106**, 3292 (1996).

[34] P. J. Bruna and F. Grein, J. Phys. Chem. A **103**, 3294 (1999).

[35] I. Carmichael, J. Phys. Chem. A **101**, 4633 (1997).

[36] D. M. Chipman, Theor. Chim. Acta **82**, 93 (1992).

[37] J. A. Pople, M. Head-Gordon, and K. Raghavachari, J. Chem. Phys. **87**, 5968 (1987).

[38] GAUSSIAN 98, Revision A.7, M. J. Frisch, G. W. Trucks, H. B. Schlegel *et al.*, Gaussian, Inc., Pittsburgh, PA, 1998.

[39] G. A. Odintzova and A. R. Striganov, J. Phys. Chem. Ref. Data **8**, 63 (1979).

[40] J. S. M. Harvey, L. Evans, and H. Lew, Can. J. Phys. **50**, 1719 (1972).

[41] A. Ding, J. Karlau, J. Weise, J. Kendrick, P. J. Kuntz, I. H. Hillier, and M. F. Guest, J. Chem. Phys. **68**, 2206 (1978).

[42] B. Fernández, P. Jørgensen, E. A. McCullough, Jr., and J. Simons, J. Chem. Phys. **99**, 5995 (1993).

[43] J. P. Visticot, P. de Pujo, J. M. Mestdagh, A. Lallement, J. Berlande, O. Sublemontier, P. Meynadier, and J. Cuvellier, J. Chem. Phys. **100**, 158 (1994).

[44] E. Anderson, Z. Bai, C. Bischof *et al.*, *LAPACK Users' Guide*, 3rd ed. (Society for Industrial and Applied Mathematics, Philadelphia, PA, 1999).

[45] W. C. Swope, H. C. Andersen, P. H. Berens, and K. R. Wilson, J. Chem. Phys. **76**, 637 (1982).

[46] J. Eloranta, http://epr.chem.jyu.fi/xemr

[47] M. T. Hutchings, Solid State Phys. **16**, 227 (1964).

[48] J. E. Wertz and J. R. Bolton, *Electron Spin Resonance: Elementary Theory and Practical Applications* (McGraw-Hill, New York, 1972), p. 269.

[49] A. Ponti, J. Magn. Reson. **138**, 288 (1999), and references therein.

[50] B. Kirste, Anal. Chim. Acta **265**, 191 (1992).

[51] J. Eloranta, K. Vaskonen, H. Häkkänen, T. Kiljunen, and H. Kunttu, J. Chem. Phys. **109**, 7784 (1998).

[52] K. Vaskonen, J. Eloranta, and H. Kunttu, Chem. Phys. Lett. **310**, 245 (1999).

[53] F. J. Adrian, J. Chem. Phys. **32**, 972 (1960).

[54] J.-L. Du, G. R. Eaton, and S. S. Eaton, J. Magn. Reson., Ser. A **117**, 67 (1995).

PAPER V

https://doi.org/10.1063/1.1360797

Reprinted with permission from T. Kiljunen et al, "Optical properties of atomic boron in rare gas matrices: An ultraviolet absorption/laser induced fluorescence study with ab initio and diatomics-in-molecules molecular dynamics analysis," *The Journal of Chemical Physics* **114**, 2001, pp. 7157–7165.

JOURNAL OF CHEMICAL PHYSICS VOLUME 114, NUMBER 16 22 APRIL 2001

Optical properties of atomic boron in rare gas matrices: An ultraviolet-absorption/laser induced fluorescence study with *ab initio* and diatomics-in-molecules molecular dynamics analysis

Toni Kiljunen,[a] Jussi Eloranta, Jussi Ahokas, and Henrik Kunttu
Department of Chemistry, University of Jyväskylä, P.O. Box 35, FIN-40351 Jyväskylä, Finland

(Received 16 November 2000; accepted 12 February 2001)

Boron atoms have been produced by laser ablation and trapped in solid Ar, Kr, and Xe matrices. In addition to stable doublet absorptions at 210–230 nm, broad temperature dependent bands less in blue have been recorded. With the aid of laser induced fluorescence measurements, *ab initio* pair potential calculations, and diatomics-in-molecules simulations these novel broad lines at 241 nm in Ar, 247 nm in Kr, and 254 nm in Xe were assigned to boron $3s(^2S)\leftarrow 2p(^2P)$ transitions. The thermal behavior of the broad absorption bands is similar to what was reported for boron atoms detected by electron paramagnetic resonance [J. Chem. Phys. **114**, 7144 (2001)]. The revised interpretation based on the new spectroscopic observations is in good agreement with theoretical predictions. © *2001 American Institute of Physics.* [DOI: 10.1063/1.1360797]

I. INTRODUCTION

The microscopic description of trapping of an orbitally degenerate atom in atomic solids such as rare gas (Rg) matrices or crystals necessitates treatment of the angular anisotropy of electron density. The impurity center may cause severe static or dynamic distortion of its lattice surrounding, which will in turn lift the degeneracy of electronic surfaces and, moreover, quench the electronic orbital angular momentum. The vast body of recent work on this subject was reviewed by Apkarian and Schwentner.[1] In the first part of the present series of investigations[2] we took boron impurity atom as a prototypical Group IIIB case, and investigated its ground state properties in terms of electron paramagnetic resonance (EPR) parameters by experiment and theory. The method allowed for direct assignment of the nature of the trapping sites of B. In order to provide complementary information of this system, similar minimal basis diatomics-in-molecules (DIM) procedure for treating the angular dependence of the electron density is utilized here in characterization of the lowest optical transition ($3s\leftarrow 2p$) of atomic boron.

Experimental matrix isolation studies of optical absorptions have shown lines heavily blueshifted from the free atom term values. Ammeter and Schlosnagle[3] were the first to report such data for Al and Ga isolated in Ne, Ar, Kr, and Xe hosts. Strongly blueshifted from the atomic line at 249.8 nm, Graham and Weltner[4] reported absorptions at 208.0 nm and 213.6 nm for B in Ar. Jeong and Klabunde[5] presented similar data for B, Al, Ga, and In in Ar in a study of reactions with methane. The $^2S\leftarrow {}^2P$ assigned absorption in these studies frequently appears as largely separated doublets which have been ascribed to multiple trapping sites of B. Although the peaks come spectrally close to the atomic $^2D\leftarrow {}^2P$ transition, those transitions should show multiplets and also shift further to the blue, perhaps beyond the detection window (below 200 nm). Classical Monte Carlo simulations for absorptions and emissions of Na and B in Ar lattice were performed by Boatz and Fajardo.[6] The authors were not, however, able to reproduce such a strong blueshift in B absorption (ca. 2500 vs 7000 cm^{-1}), and the simulations yielded singlet spectra for all the trapping configurations studied.

Close correspondence between experiment and theory has been obtained for simpler systems by Alexander and coworkers. First, fluorescence excitation of BAr van der Waals complex, $B\,^2\Sigma^+ - X\,^2\Pi$ bands, was characterized by *ab initio* calculations,[7] and a similar study was also carried out for BNe.[8] Then, by using the BAr potentials pairwise in quantum Monte Carlo simulations, the $3s\leftarrow 2p$ transition of BAr$_2$ was simulated and found to account for the experimental observations.[9] More recently, this methodology has been used for AlNe complex involving spin–orbit interaction and transitions to states due to Al$(3d)\,^2D$ excited atom.[10] Finally, the B$(2s2p^2)^2D$ state excitation was succesfully added to theory in a BAr$_2$ study.[11]

The experimental blueshifts for BAr and BAr$_2$ are 230 and 420 cm^{-1}, respectively.[9] Of particular interest is the 108 cm^{-1} barrier in the BAr double well $B\,^2\Sigma^+$ potential at internuclear separation corresponding to the ground state minimum. Thus, the blueshift is a combined consequence of ground state solvation and the shape of the excited state surface. For the higher B$(2s2p^2)$ excitations, however, the spectral lines of BAr$_2$ extend to lower and higher energies from the atomic 208.9 nm transition. The redshifted peak in BAr$_2$ corresponds to transition to $^2D_{x^2-y^2}$- and $^2D_{xy}$-like states, that is, to the $\Lambda=2(C\,^2\Delta)$ type state, which shows strongest binding among the three-state manifold. In a solid phase, however, the ground state is predominantly quenched $\Lambda=0(^2\Sigma)$ and this transition becomes forbidden. Therefore, in light of the previously published data it seems that the

---

[a] Author to whom correspondence should be addressed. Electronic mail: kiljunen@epr.chem.jyu.fi

observed transitions in a matrix, if boron at all, are the blue-shifted $3s \leftarrow 2p$, not $2p \leftarrow 2s$.

In the present paper we re-examine the absorption spectra theoretically by using *ab initio* pair potentials for all interactions, and utilize the DIM theory to account for the effects by the lattice surrounding. Then, we show absorption and laser induced fluorescence (LIF) spectra of B in Ar, Kr, and Xe matrices. Atomic boron is produced by laser vaporization in these experiments. Based on the new spectral observations the interpretation of the UV spectra of B/Rg solids is revised in a way which yields consistency with the theoretical predictions.

II. *AB INITIO* CALCULATIONS

A. Methods of computation

The coupled-cluster theory forms the basis for description of the interaction between the boron and a rare gas atom in this study. In particular, the RHF–UCCSD(T)[12] variant (spin-unrestricted open shell coupled-cluster with singles, doubles and perturbative triples excitations using high-spin restricted Hartree–Fock reference) of this method is utilized for the $X\,^2\Pi$ and $A\,^2\Sigma$ electronic states of RgB correlating to the ground state B(^2P) and Rg(^1S) atomic limits. For Rg–Rg pairs, the closed shell CCSD(T) theory[13] was used in computation of the potential energy curves (PEC). The advantages of this method, in addition to its high accuracy, are connected to the concept of size consistency and the relatively straightforward and reliable counterpoise procedure (CP)[14] for correcting the effects arising from the basis set superposition errors (BSSE). This method is, however, of ground state nature and therefore applicable only for the lowest state of particular spin and symmetry (irreducible presentation in the C_{2v} point group). For this reason, and also because of the enhanced multiconfigurational character, the B($2p3s$) excited $B\,^2\Sigma$ state potential energy curves are calculated with a multireference configuration interaction (MRCI)[15,16] method.

For MRCI, two kinds of complete active spaces (CAS) were used as a reference. The smaller CAS includes the $2s$, $2p$, and $3s$ orbitals and the valence electrons of B atom resulting in a $3e/5o$ combination. The larger CAS is a full valence space, leaving only the inner core orbitals unrelaxed. This leads to a $11e/9o$ situation. As the Rg and B orbitals were not allowed to mix in the smaller CAS, i.e., excitations of Rg electrons to the boron orbitals were ruled out, the evaluation of the BSSE was justified according to the usual CP procedure, where the energies of the atomic fragments calculated with the full basis of the diatomic were subtracted from the molecular energy. The B atom contribution was calculated similarly to the molecular case, i.e., MRCI with $3e/5o$ CAS, but the Rg part was obtained with single reference CISD (singles and doubles CI). For the larger CAS and in general for multireference calculations, the CP correction is not well defined, and there remains a size-consistency correction (scaling to zero interaction at infinite distance) that had to be made for CP-corrected interactions.

In order to overcome the evident problem with the CP correction, a study with linear ArBAr geometry (now in D_{2h}) was performed. This provided an indirect route to carry out CCSD(T) calculations also for the B state. In addition, the CCSD(T) method was used for the $^3\Pi$ and $^{1,3}\Sigma^+$ states of ArB$^+$ to further study the interactions by the ionic core. For all the MRCI calculations in this study the Davidson method[17,18] for quadratic cluster correction of size inconsistency was used and the results are denoted as MRCI+Q energies.

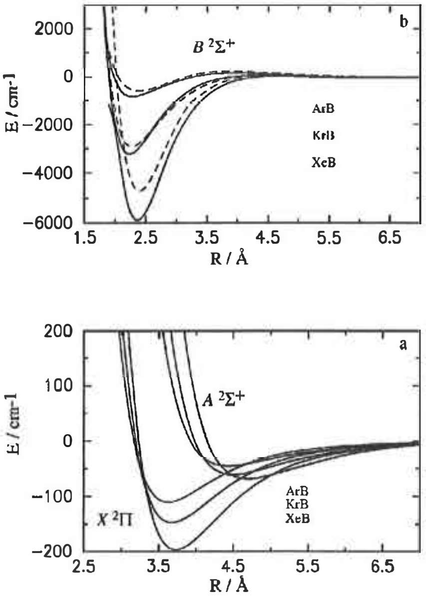

FIG. 1. The Rg–B potential energy curves. (a) The CCSD(T) calculated lowest states; (b) the MRCI+Q calculated B state with small active space and CP correction (dashed lines), and large active space (solid lines).

All calculations described above rely on the singly augmented correlation consistent basis set (aug-cc-pVQZ)[19] of Dunning for B and the effective core potential (ECP)[20] basis set developed by the Stuttgart group for Rg. A $\{spdf\}$ set of diffuse functions was added to the Rg valence part as previously,[21] and two diffuse s functions were added in an even-tempered manner (producing $\zeta_s = 0.010\,013, 0.003\,685$ exponents) to the B atom basis for $B\,^2\Sigma$ state calculations. Both basis sets were used in their contracted forms. This work was carried out with the MOLPRO code.[22]

B. RgB PECs for $X\,^2\Pi$, $A\,^2\Sigma^+$, and $B\,^2\Sigma^+$ states

The CCSD(T) and MRCI calculated potential energy curves formed from the $B\,^2P$ and ^2S atomic asymptotes are shown in Fig. 1. For both the ground and excited states studied, increasing stabilization is observed as the Rg becomes heavier. Simultaneously, the $B\,^2\Sigma^+$ state barrier between the strongly bound inner region of the potential and the van der Waals minimum disappears in KrB and XeB. We remind that in NeB the B state is not bound at all.[8] The magnitude of the BSSE effect on the well depths increases nearly linearly from Ar to Xe. In a qualitative level, not much difference is found with the two reference spaces. Before CP correction,

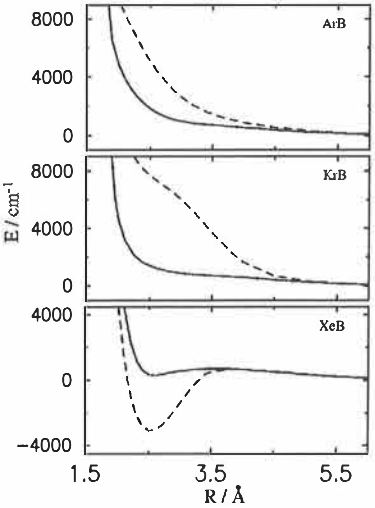

FIG. 2. The Rg–B $B\ ^2\Sigma^+$ state PECs as obtained by the CASSCF method. Dashed lines correspond to the smaller active space and solid lines to the full valence space.

the smaller reference yields almost equal well depths and barrier heights as the larger one does. The underlying CASSCF-reference results in Fig. 2 show more clearly the difference when interatomic excitations are included in the multiconfiguration wave function compared to intraatomic-only correlation effects. Surprisingly, the small reference space function yields significant binding in Xe compared to the full valence space computation.

We collect the potential parameters obtained from the present calculations, and to be used in the subsequent simulations, in Table I. Note that, considering the accuracy of the numbers, the equilibrium values R_m and D_e refer to the PEC calculations with a finite number of points spline fitted instead of rigorous geometry optimization. Special emphasis is put on the accuracy of the dissociation region, which is of high importance in defining the energetics of the simulated optical transitions. The potential form $V'(R)$ given in Table I was chosen for its ability to produce the barrier found in argon. The earlier work[7,9] allows comparison in the case of ArB. Alexander and co-workers used a scaling factor of 1.19 for correlation energy to match their calculated $X\ ^2\Pi$ and $A\ ^2\Sigma^+$ state curves with those derived from experiments. The experimental D_0 values are 102.4 cm^{-1} and 1005 cm^{-1} for $X\ ^2\Pi$ and $B\ ^2\Sigma^+$ states, respectively.[9] By applying the same scaling factor we obtain very similar potential curves that have been presented earlier[9] for the $X\ ^2\Pi$ and $A\ ^2\Sigma^+$, and $B\ ^2\Sigma^+$ states.

C. ArBAr and ArB$^+$ PECs

The CCSD(T) calculated B_{3u}, B_{1u}, and A_g symmetric states for the linear nuclear configuration of ArBAr allow comparison with the $X(B_1)$, $A(A_1)$, and $B(A_1)$ states of ArB, respectively, when the interaction energies are divided by 2. Within the assumption of pairwise additivity, the PECs obtained with these two methods should coincide. This is indeed the case for the $X\ ^2\Pi$ and $A\ ^2\Sigma^+$ states for a wide range of internuclear separations R. As seen in Fig. 3, the perfect coincidence in the 2.5–6.5 Å region diverges only at very short distances. The upper panel in Fig. 3 compare the $B\ ^2\Sigma^+$ state curves obtained from the ArBAr CCSD(T) calculation with the corresponding ArB MRCI calculation. It is immediately seen that the curves no more remain the same and a pronounced 0.3–0.4 Å shift in the position of the inner well can be seen. Two possible reasons may be considered for this behavior. Either the methodological difference between CC and CI procedures produces such divergent results, or it is a true manifestation of the breakdown of pair additivity of the interaction. The former effect could be expected for binding that arises from nondynamical correlation effects. The $\mathcal{T}_1$ diagnostics of Lee and Taylor[23] gives a steeply descending value from 0.035 at 1.6 Å to 0.012 at 6.0

TABLE I. The potential parameters[a] used in the DIM–MD simulations. All the numbers except those for the B states refer to CP-corrected CCSD(T) calculations. The $B\ ^2\Sigma^+$ states are computed at the MRCI level with full valence CASSCF reference.

Molecule	State	R_m (Å)	D_e (meV)	A	B	C	D	E
Ar_2	$^1\Sigma^+$	3.85	9.9	8 658 900	3.502 95	0.0	24 191.4	701 938
Kr_2	$^1\Sigma^+$	4.15	13.6	11 427 300	3.257 63	0.0	54 615.7	1 606 290
Xe_2	$^1\Sigma^+$	4.55	18.2	12 661 400	2.868 97	0.0	40 666.7	7 491.210
ArB	$X\ ^2\Pi$	3.62	13.6	1 790 810	3.064 06	4 032 790	26 088.9	882 091
	$A\ ^2\Sigma^+$	4.43	5.6	1 446 350	2.748 00	2 528960	69 363.2	614 900
	$B\ ^2\Sigma^+$	2.29	102.5	101.671	1.422 17	−3.224 24	0.794 08	2.282 74
KrB	$X\ ^2\Pi$	3.67	18.2	1 661 010	2.943 33	5.160 650	59 050.3	932 789
	$A\ ^2\Sigma^+$	4.50	7.5	1 526 100	2.638 59	3 453 620	114 987	804 788
	$B\ ^2\Sigma^+$	2.23	399.2	403.956	1.685 27	−2.252 02	0.556 162	2.199 47
XeB	$X\ ^2\Pi$	3.73	24.4	1 358 250	2.795 72	5 399 660	127 040	640 087
	$A\ ^2\Sigma^+$	4.70	8.4	1 801 470	2.527 05	9 556 620	153 680	1 796 060
	$B\ ^2\Sigma^+$	2.36	730.1	760.355	1.830 62	−2.041 87	0.470 257	2.321 27

[a] The parameters are in units yielding $V(R)$ in meV (Å). The fitting functions were $V(R)=Ae^{-BR}+CR^{-12}-DR^{-6}-ER^{-8}$ for the CCSD(T) results and $V'(R)=-A[1+B(R-E)+C(R-E)^2+D(R-E)^3]e^{-B(R-E)}$ for the $B\ ^2\Sigma^+$ states.

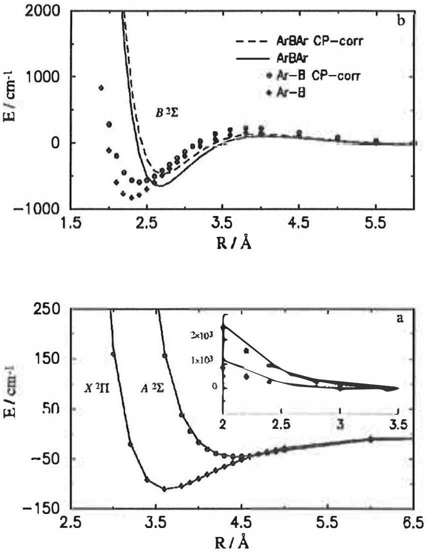

FIG. 3. A test for the pair additivity of the potentials. (a) CCSD(T) curves from ArBAr calculation (solid lines) and from ArB calculation (◇ for *X* and ○ for *A*); (b) CCSD(T) ArBAr vs MRCI+Q ArB curves for the $B\,^2\Sigma$ state.

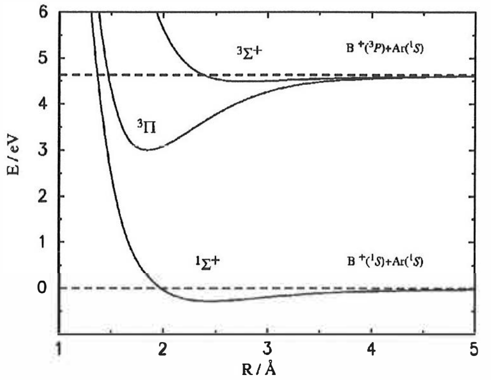

FIG. 4. The lowest state potential energy curves for ArB^+ as calculated with the CCSD(T) method and corrected for BSSE. The asymptotic limits (0 and 4.63 eV) are marked. The well depths are close to the experimental values (Ref. 25) 0.3 eV and 1.5 eV for $^1\Sigma^+$ and $^3\Pi$, respectively.

Å indicating dynamical correlation to be more important for the potential energy well. The latter explanation would be supported by the fact that for the two theoretical methods, although different in nature, the vast body of literature[24] has shown comparable accuracy, close to the full CI limit.

A simple explanation for the inner well produced when the $2p$ electron is excited to the $3s$ orbital is the strong interaction between the Rg atom, penetrated inside the Rydberg node, and the B^+ ion core. As seen in the PECs above, and discussed previously,[7] theoretical reproduction of such well necessitates triple and quadruple excitations in MRCI indicating more complex origin for the barrier-well shape of the potential. The calculation on ArB^+, which shows binding already at the SCF level,[25] mimics the ion core part of the situation. Here, the charge polarization effect is isolated from screening by the unpaired electron, and the resulting bound $^1\Sigma^+$ PEC is shown in Fig. 4. By further excitation of B^+ to its ^3P state, more pronounced Rg-ion core (effectively 2+) attraction results. We show the $^3\Pi$ and $^3\Sigma^+$ states also in Fig. 4. The well depths are 0.28 eV at 2.4 Å, 1.62 eV at 1.8 Å, and 0.14 eV at 2.8 Å for the $^1\Sigma$, $^3\Pi$, and $^3\Sigma$ states, respectively. With these results in mind we suggest an upper limit of 0.28 eV for the *B* state ArB well, and ascribe it to charge polarization screened due to electron correlation.

III. DIM SIMULATED ABSORPTIONS

The molecular dynamics simulation method is described in detail in the preceding paper.[2] Briefly, the applied DIM formalism, the framework for evaluation of instantaneous forces, produces three eigenstates in the $\{|p_x\rangle,|p_y\rangle,|p_z\rangle\}$ basis. The lowest eigenenergy gives directly the magnitude of ground state solvation for the lattice embedded ^2P atom. The excited $B\,^2\Sigma^+$ state, on the other hand, is isotropic and the interaction with the lattice atoms is a simple pairwise sum over the nearest neighbors. Therefore, the $3s \leftarrow 2p$ absorption was represented by recording the energy difference between the lowest energy eigenvalue and the potential energy evaluated at the excited $B\,^2\Sigma^+$ state, and adding the atomic 249.75 nm offset. This procedure was carried out at every tenth simulation step (timestep 0.3 fs). The spectrum was obtained simply from the histogram (bin width 0.05 nm) of this data after the 51 ps time propagation, and no actual electronic transitions, i.e., Franck–Condon factors or transition moments, were considered in the simulation. This means assumption of a constant transition dipole, thus the intensity distribution is dictated solely by configuration distribution, both in atomic and electronic degrees of freedom. The configuration distribution, that is, the sampling of Franck–Condon region, on the other hand, is dictated only by thermal movement due to the classical description of nuclear motion. At these temperatures (10 K), however, the amplitude of zero-point vibrations is of comparable magnitude to the thermal one. While it is completely neglected, a dominant portion of this effect is attained by present treatment according to the trajectories, and the possibly remaining portion has minimal effect on the spectral blueshifts. The outcome of this procedure, which has been applied also for $Ba-(Ar)_n$ clusters before,[26] is seen in Fig. 5.

In order to theoretically reproduce the experimental spectral observations, we aimed at simulated spectra which would show strong blueshift from the atomic transition. By applying a scaling factor of 1.2 to the ground state potentials (for both Rg_2 and RgB) we attained an extra ~200 cm^{-1} shift. The slightly higher barrier obtained with the CP corrected $B\,^2\Sigma^+$ state calculation for ArB resulted in ~1000 cm^{-1} larger blueshift as compared to the full valence potential in the simulation. In Kr host the effect was minor, ~200 cm^{-1} and to the opposite direction, but for Xe, as the larger active space XeB calculation yielded markedly lower energies at optically accessed region, the difference was about 800 cm^{-1}.

In Fig. 5 we present the results of simulations which rely

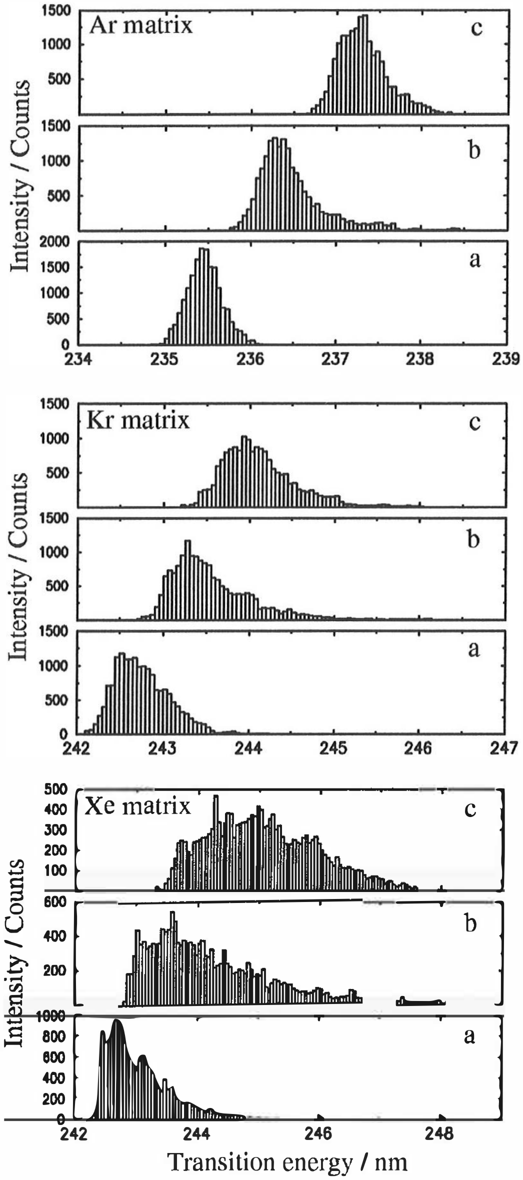

FIG. 5. The DIM simulated absorption spectra obtained in different lattice environments. (a) B atom in substitutional site of otherwise perfect lattice, (b) one lattice vacancy is issued as nearest neighbor to B, (c) two nearest-neighbor lattice vacancies. The simulations are based on scaled ground state potentials and the larger reference space for the MRCI. The spectra correspond to a simulation period of 51 ps.

on the scaled ground state potentials and excited states obtained with the larger active space. It is immediately seen that the shift to the blue decreases as vacancies are issued in the lattice. This is, indeed, consistent with the observations by Boatz and Fajardo[6] who found similar trend by increasing the size of the trapping site. It is clearly a ground state solvation effect since it is also observed in Kr and Xe. The only exception from the above rule was noticed in Xe. There, the nonscaled potential yielded a transition closer to the atomic value, whereas energy scaling produced a broad distribution between 242–250 nm.

The most striking outcome of the present series of simulations is that the large, about 7000–8000 cm^{-1} in argon, blueshift proposed by the experiments[4,5] was not supported. The most blueshifted peak was simulated at 229 nm by scaled, CP-corrected input and a perfect lattice environment. In the preceding study,[2] we showed that B atoms detected by EPR are trapped in axially symmetric environments produced by one nearest-neighbor lattice vacancy, for example. In the present case, we have peaks centered at 236.5, 243.5, and 244 nm in Ar, Kr, and Xe, respectively, showing a matrix dependence well below what is expected. These numbers are relatively consistent with the simulations by Boatz and Fajardo.[6] Although it is evident that our results are very sensitive to the quality of the pair potential data, it is a straightforward conclusion that by no means can the strong blueshift be reproduced by theory.

Another feature inherent in the simulations is that for a given initial configuration, with or without lattice vacancies, the resulting spectra appear as single lines. In the experiments carried out earlier, however, a distinct doublet absorption arises. The tentative assignment to multiple trapping means, according to the simulations, that one of the absorptions is attributed to a tight structure involving 0–2 vacancies and the other one a more distorted and looser trapping structure. This contradicts the fact that both absorptions should be largely blueshifted. These confusing observations led us to perform new measurements. Before entering there, we shortly examine interstitial trapping.

A boron atom placed in an octahedral site of a FCC Rg lattice is subject to strongly repulsive forces. At the end of a simulation period, we see (i) from atomic coordinates that the relaxed structure comprises somewhat distorted lattice where two of the nearest neighbors are pushed further apart, (ii) from orbital autocorrelation functions that axial symmetry is produced in terms of strict directional locking of the lowest energy eigenvector and free rotation of the *xy* frame, and (iii) from the DIM eigenenergies that only the lowest one is negative in contrast to the other trapping sites considered for which all of them were bound (solvated). We show in Fig. 6 the radial distribution functions (RDF) obtained from 30 ps and 51 ps simulations together with the absorption spectra based on 51 ps simulation.

The relaxed interstitial trapping in Ar comprises roughly of B atom displaced slightly above a plane that consists of four nearest neighbors at 3.2–3.5 Å distances, one atom above at 3.0 Å, and one below at 3.7 Å. In Kr, the B atom is situated more closely in the four atom plane with distances 3.2–3.4 Å, pushing the atoms above and below the plane to 3.7 Å. In Xe the situation is similar, the four atoms in plane are 3.3–3.5 Å apart from B, and the perpendicular two are pushed to 3.8–3.9 Å. The time averaged maxima seen in RDF clarify these observations. The orbital correlation functions reflect the fact that the unpaired electron occupies an orbital parallel to the normal of the four atom plane, pointing at the more distant atoms. Finally, note that the absorption

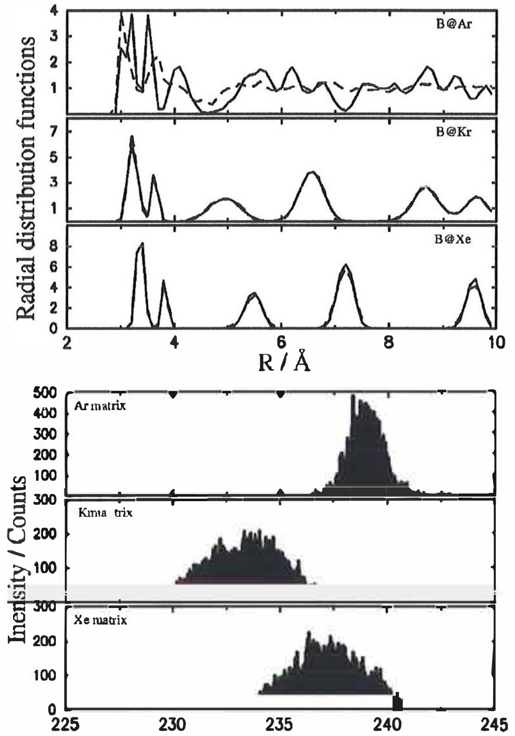

FIG. 6. Upper portion: the B–Rg radial distribution functions from single 51 ps (solid lines) and 30 ps (dashed lines) simulation trajectories for interstitial trapping structures. The impurity atom was initially placed at an octahedral site. Lower portion: the simulated absorption spectra resulting from interstitial trapping with otherwise same input parameters as in Fig. 5.

spectra in Fig. 6 are all considerably broader compared to what was simulated for substitutional trapping.

IV. EXPERIMENTAL SECTION

A. Setup

Boron atoms were produced by laser vaporization technique. The beam of a XeCl excimer laser (Estonian Academy of Sciences, ELI-94) with a pulse energy of 35–58 mJ was focused on the surface of a boron target (Aldrich Chem. Co., Boron 99+ %). The boron target was placed at a distance of ca. 15 mm from a MgF_2 cold window. The matrix host gases argon (99.9999%, AGA), krypton (99.997%, AGA), and xenon (99.997%, AGA) were deposited through a 1/16 inch stainless steel capillary. The outlet of the capillary was placed ca. 7 mm from the cold window and the angle between the window and the capillary was ca. 45 degrees.

The gas deposition rate from a volume of 1 dm^3 and backing pressure of 516–651 torr was adjusted to 3.3–4.3 torr/min, and the total deposited pressure was 30 torr (1.8 m mol). A constant gas condensation temperature of 9.5–10 K was maintained by closed cycle helium cryostat (ADP Cryogenics, Inc., DE-202A) and the temperature was controlled with a Lake Shore 330 controller unit. Laser ablation was started after 15 torr pure matrix gas was deposited and we observed that laser pulse repetition rates of 15 Hz or higher produced samples showing well resolved spectra.

In order to compensate for scattering by the matrix, we also deposited reference matrices for background correction procedure. For this purpose blank Ar, Kr, and Xe matrices were deposited similarly as described for the boron doped samples. The only difference was that for blank Kr and Xe samples the rate of deposition was increased to 16–18 torr/min. Under these conditions the blank and boron doped solid matrices showed very similar optical properties which is essential for accurate background correction.

The UV-absorption spectra of the matrix samples were recorded with a spectrometer composed of an intensified ICCD camera with 690×256 active pixels (Andor Technologies), a 12.5 cm focal length spectrograph (Oriel Instruments), and a 30 W deuterium lamp. Although the window of the detector was of MgF_2 the quartz lamp housing limited the high energy side of detection to approximately 200 nm. Atomic lines of mercury were used for wavelength calibration of the ICCD. Signal intensities in different measurements were adjusted to the same level by the detection gate width. Background correction was made by subtracting the reference spectrum recorded from a blank sample from the spectrum under consideration. In the LIF measurements the same detection system was used in combination with an ArF (193 nm) excimer laser (Lambda Physic Optex) with a pulse energy of 7–9 mJ. The timing between the excitation pulse and detection was controlled with a digital delay generator (Stanford Research Systems).

B. Absorption and LIF spectra

The absorption spectra obtained from B/Rg matrices are presented in Fig. 7. The decrease of intensities of spectral features at the low energy side of the left column is clearly recognizable although, due to scattering effects and steep profiles, the baseline was difficult to adjust to a comparable level. For Ar matrix, we show spectral changes upon stepwise warming 10 K→12 K→15 K→20 K to demonstrate the noticeable disappearance of the 241 nm absorption, and simultaneous growth of an absorption at 331 nm, which has been assigned to B_2 (0,0) $\Sigma-\Sigma$ band.[4] Most importantly, no changes are observed in the intensity of the narrow doublet at 210 nm and 216 nm.

For the Kr matrix, the spectra shown in Fig. 7 were measured at temperatures of 10 K, 12 K, 15 K, and 25 K, and bleaching of the 247 nm spectral feature was observed as in Ar. In this case the absorption showing simultaneous growth is located at 335 nm. Additionally, at further elevated temperatures (30–40 K) a new absorption, assigned to B_2 (1,0), appeared at 325 nm (not shown) and slight reduction of the doublet at 211 and 227 nm was observed. Quite interestingly, at 25 K growth of the 227 nm peak is observed while the 211 nm counterpart is unchanged.

In Xe matrix, thermal behavior of the absorptions is qualitatively similar to what is seen in Kr. The broad absorption, now centered at 254 nm, is originally the most intense peak, and gradually decreases at elevated temperatures (10

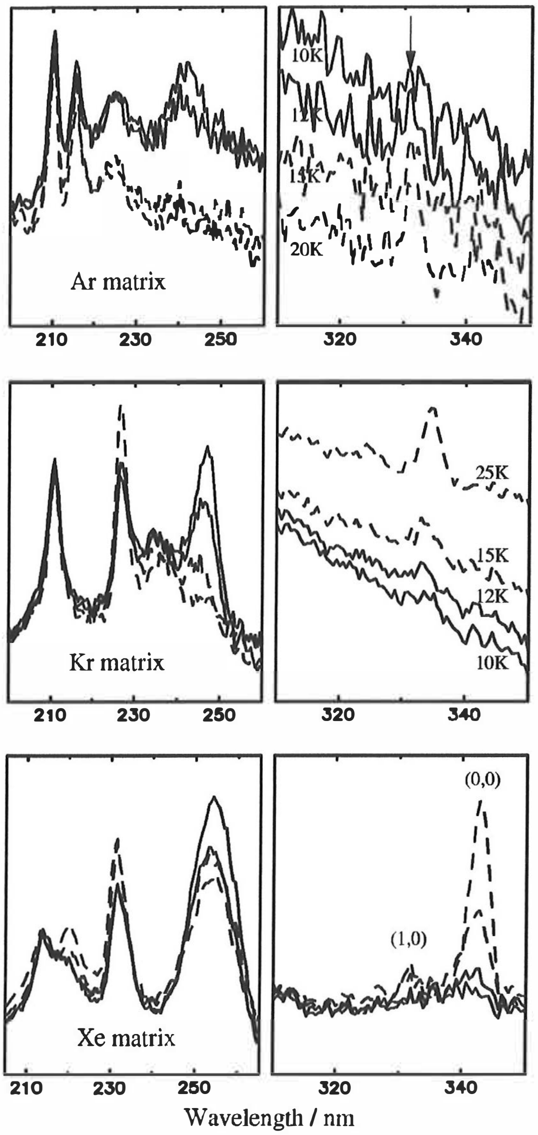

FIG. 7. The measured absorption spectra of B atom doped Rg matrices, background corrected as explained in text, at different temperatures. Left column: the broad line is thermally bleached whereas the narrow doublets stay intact. Right column: the corresponding growth of the B_2 absorptions.

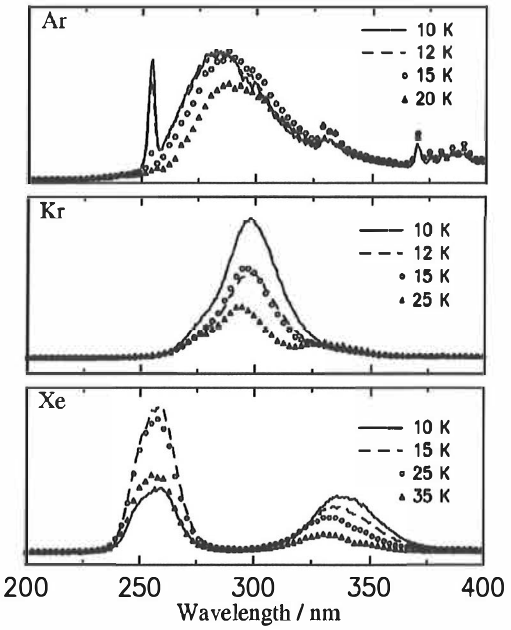

FIG. 8. The LIF spectra of B/Rg matrices. The 250 nm spectral feature in Xe matrix corresponds to Xe_2H impurity emission.

K, 15 K, 25 K, and 35 K shown in Fig. 7). This is accompanied with an increase of an absorption at 343 nm. Alike in Kr, the B_2 (1,0) absorption band at 332 nm is resolved in traces recorded at 25 K and 35 K. The narrow doublet shows peaks at 214 nm and 232 nm and a shoulder at 220 nm. The shoulder gains intensity at elevated temperatures as does the 232 nm absorption.

The emission spectra shown in Fig. 8 provide complementary proof that the origin for the novel absorptions at 241–254 nm are most probably the boron $3s \leftarrow 2p$ transitions. The temperature dependence, i.e., the reduction of emission intensities at elevated temperatures, would mean that the emitting species can be assigned to the same one that is responsible for the observed novel absorptions.

The Ar matrix is most peculiar, since two distinct emission features are present in the spectrum. The observed spectral shape can be qualitatively explained with the aid of *ab initio* calculated potentials of Fig. 1. If we assume vertical excitation from the ground X state minimum, the excited B state is initially prepared in the region, where a low barrier separates the deeply bound inner part of the potential from the almost flat van der Waals (vdW) region. Subsequent relaxation of the excited state, strongly dependent on the atomic configuration, can then proceed either to the vdW or inner well minima, from which the system radiates. Taking into account the shape of the pair potentials involved, the vdW case would yield a relatively narrow spectral distribution compared to the inner well for which significant repulsion on the ground state would be observed as a very broad spectrum. Thus, the narrow line near the atomic transition energy can be ascribed to trapping of B in a loose site, the minor redshift arising from the $B\,^2\Sigma$ state vdW interaction. The broad line, considerably redshifted, is therefore due to trapping sites that allow relaxation to tighter emitting structures. At elevated temperatures the sharp emission disappears and the broad maxima gets weaker and redshifts.

In Kr and Xe matrices only broad emission bands are observed, which is quite expected as no barrier can be found in the excited state potential. Moreover, the extent of redshift with respect to the absorption indicates binding in the emitting $B\,^2\Sigma$ state. The thermal behavior of the emission inten-

TABLE II. UV absorptions and LIF emissions in B doped Ar, Kr, and Xe matrices. Estimated accuracy of the last digit is set in parentheses.

	Absorption		LIF	
Rg host	Type	λ (nm)	Type	λ (nm)
	stable	210.4(1)		
	stable	215.6(1)	broad	285(5)
Ar	transient	241(2)	narrow	254.2(3)
	B_2 (0,0)	331(1)		
	stable	210.7(2)		
	stable	226.7(3)		
Kr	transient	247(1)	broad	297(2)
	B_2 (1,0)	325(1)		
	B_2 (0,0)	335(1)		
	stable	213.7(1)		
	thermal	220.0(2)		
	thermal	231.5(1)		
Xe	transient	254(1)	broad	337(3)
	B_2 (1,0)	332(1)	$Xe_2^+H^-$	257(2)
	B_2 (0,0)	343(1)		

sity is nevertheless similar to the Ar case but the band experiences blueshift at higher temperatures. The lowest panel in Fig. 8 emphasizes the presence of mobile H atoms which show intense emission assigned[27] to $Xe_2^+H^-$. This emission increases first from 10 K to 15 K, and then decreases at further elevated temperatures.

It would be tempting to interpret the data shown for Ar matrix as resulting from substitutional trapping with additional 0–2 vacancies (the sharp emission), and interstitial trapping (the broad emission). In fact, the temperature behavior of these bands would support this conclusion as the tighter site can be expected to be more easily mobilized. The results in Kr and Xe are, however, in contradiction with this model. There, interstitial trapping produces considerably stronger blueshifts compared to substitutional structures. We are thus left with an interpretation that strongly temperature dependent bands in Ar, Kr, and Xe matrices are due to $3s \leftarrow 2p$ transitions of matrix perturbed B atoms trapped identically as boron atoms observed by EPR.[2]

While not substantiated by a systematic study of diffusivity or recombination kinetics, the thermally induced increase of the B_2 band, if originating from the mobilized atoms, implies pairwise trapping and subsequent short-range recombination, thus leaving a portion of the trapped atoms stable. At a qualitative level, however, the thermal dependence of the B_2 absorption rise follows that of the transient B fall, so we state that the structural relaxation during annealing results in recombination of atoms in sites that are axially symmetric (according to EPR) due to nearby vacancies and therefore more loose (less in blue) and more easily mobilized. Furthermore, since the absorptions termed as stable doublets do not behave similar to the magnetically detected transient atoms, these might correspond to orbitally nonquenched atoms, for which the $^2D \leftarrow {}^2P$ transitions are allowed.

Finally, we can make a comparison of our transitions collected in Table II with those published by Tam *et al.*[28] (this paper appeared after the present work was submitted) for B and B_2 in p-H_2, n-D_2, and Rg matrices. These authors presented transitions (that we have termed as transients) at 223.0, 235.8, and 252.6 nm in Ar, Kr, and Xe, respectively. Their tentative assignment was the $3s \leftarrow 2p$ Rydberg transition of a secondary trapping site. Annealing was performed for Ar matrix only, and disappearance of the 223.0 nm absorption was observed. We agree on the Xe interpretation, but have not assigned the spectral features at 223 and 235 nm in Ar and Kr due to problems in the baseline. The interpretation given in Ref. 28 for absorptions at 208.4 and 213.9 nm in Ar, 210.3 and 226.7 nm in Kr, and 211.9, 219.8, and 231.9 nm in Xe was based on the intensity ratios of these lines. They assigned the doublets to the same trapping site but different transitions, the one in blue being the core-to-valence $^2D \leftarrow {}^2P$. Also the middle peak in Xe, that appears as the rising shoulder in our spectrum, was tentatively attributed to this transition. Further support to these assignments was provided by a parallel theoretical work,[29] where the spectrum simulation was performed for solid *para*-hydrogen by quantum molecular dynamics method.

V. CONCLUSIONS

The main result in this paper is that the major discrepancy between experiment and theory in interpreting the B atom optical spectroscopy in Rg hosts was partially resolved by new experiments. The novel bands revealed here are (i) in better accord with the present DIM simulated spectra, for which considerable effort was addressed to validate the pair interaction input data, and (ii) show temperature dependence very similar to what was observed in the previous study by EPR.[2] In particular, trapping near vacancies is the most probable situation for these species. The origin of the stable doublets remains unclear. Simulations with different trapping structures were not very helpful to unravel this issue. Nevertheless, one of the earlier suggestions in literature, namely the boron $2p \leftarrow 2s$ transition, although seemingly more doubtful in light of the present results, has arised new attention[28] and may as well be the source for the line most in blue. In all, the most justified explanation is a combined structural effect on the ground state and the thermal stability, and therefore on the possible electronic transitions taking place in a matrix. As the present study simulates a bulk lattice, possible surface effects could not be considered. Simulations with finite size clusters might provide new insights into the subject. Additional experiments and nonadiabatic simulations are planned to provide a more rigorous interpretation of the LIF spectra.

[1] V. A. Apkarian and N. Schwentner, Chem. Rev. **99**, 1481 (1999).

[2] T. Kiljunen, J. Eloranta, J. Ahokas, and H. Kunttu, J. Chem. Phys. **114**, 7144 (2001), preceding paper.

[3] J. H. Ammeter and D. C. Schlosnagle, J. Chem. Phys. **59**, 4784 (1973).

[4] W. R. M. Graham and W. Weltner, Jr., J. Chem. Phys. **65**, 1516 (1976).

[5] G. Jeong and K. J. Klabunde, J. Am. Chem. Soc. **108**, 7103 (1986).

[6] J. A. Boatz and M. Fajardo, in *Proceedings of the High Energy Density Matter (HEDM) Contractor's Conference*, edited by T. L. Thompson (USAF Phillips Laboratory, Edwards Air Force Base, CA, 1993), p. 351.

[7] E. Hwang, Y.-L. Huang, P. J. Dagdigian, and M. H. Alexander, J. Chem. Phys. **98**, 8484 (1993).

[8] X. Yang, E. Hwang, P. J. Dagdigian, M. Yang, and M. H. Alexander, J. Chem. Phys. **103**, 2779 (1995).

[9] M. H. Alexander, A. R. Walton, M. Yang, X. Yang, E. Hwang, and P. J. Dagdigian, J. Chem. Phys. **106**, 6320 (1997).

[10] X. Yang, P. J. Dagdigian, and M. H. Alexander, J. Chem. Phys. **108**, 3522 (1998).

[11] J. R. Krumrine, M. H. Alexander, X. Yang, and P. J. Dagdigian, J. Chem. Phys. **112**, 5037 (2000).

[12] P. J. Knowles, C. Hampel, and H.-J. Werner, J. Chem. Phys. **99**, 5219 (1993).

[13] C. Hampel, K. Peterson, and H.-J. Werner, Chem. Phys. Lett. **190**, 1 (1992).

[14] S. F. Boys and F. Bernardi, Mol. Phys. **19**, 553 (1970).

[15] H.-J. Werner and P. J. Knowles, J. Chem. Phys. **89**, 5803 (1988).

[16] P. J. Knowles and H.-J. Werner, Chem. Phys. Lett. **145**, 514 (1988).

[17] M. R. A. Blomberg and P. E. M. Siegbahn, J. Chem. Phys. **78**, 5682 (1983).

[18] S. R. Langhoff and E. R. Davidson, Int. J. Quantum Chem. **8**, 61 (1974).

[19] R. A. Kendall, T. H. Dunning, Jr., and R. J. Harrison, J. Chem. Phys. **96**, 6796 (1992).

[20] A. Nicklass, M. Dolg, H. Stoll, and H. Preuss, J. Chem. Phys. **102**, 8942 (1995).

[21] T. Kiljunen, J. Eloranta, and H. Kunttu, J. Chem. Phys. **110**, 11814 (1999).

[22] MOLPRO is a package of *ab initio* programs written by H.-J. Werner and P. J. Knowles, with contributions from R. D. Amos, A. Bernhardsson, A. Berning *et al.*

[23] T. J. Lee and P. R. Taylor, Int. J. Quantum Chem., Quantum Chem. Symp. **23**, 199 (1989).

[24] T. J. Lee, A. P. Rendell, and P. R. Taylor, J. Chem. Phys. **93**, 6636 (1990), for example.

[25] A. Ding, J. Karlau, J. Weise, J. Kendrick, P. J. Kuntz, I. H. Hillier, and M. F. Guest, J. Chem. Phys. **68**, 2206 (1978).

[26] J. P. Visticot, P. de Pujo, J. M. Mestdagh, A. Lallement, J. Berlande, O. Sublemontier, P. Meynadier, and J. Cuvellier, J. Chem. Phys. **100**, 158 (1994).

[27] J. Eloranta and H. Kunttu, J. Chem. Phys. **113**, 7446 (2000), and references therein.

[28] S. Tam, M. Macler, M. E. DeRose, and M. E. Fajardo, J. Chem. Phys. **113**, 9067 (2000).

[29] J. R. Krumrine, S. Jang, M. H. Alexander, and G. A. Voth, J. Chem. Phys. **113**, 9079 (2000).

DEPARTMENT OF CHEMISTRY, UNIVERSITY OF JYVÄSKYLÄ
RESEARCH REPORT SERIES

1. Vuolle, Mikko: Electron paramagnetic resonance and molecular orbital study of radical ions generated from (2.2)metacyclophane, pyrene and its hydrogenated compounds by alkali metal reduction and by thallium(III)trifluoroacetate oxidation. (99 pp.) 1976
2. Pasanen, Kaija: Electron paramagnetic resonance study of cation radical generated from various chlorinated biphenyls. (66 pp.) 1977
3. Carbon-13 Workshop, September 6-8, 1977. (91 pp.) 1977
4. Laihia, Katri: On the structure determination of norbornane polyols by NMR spectroscopy. (111 pp.) 1979
5. Nyrönen, Timo: On the EPR, ENDOR and visible absorption spectra of some nitrogen containing heterocyclic compounds in liquid ammonia. (76 pp.) 1978
6. Talvitie, Antti: Structure determination of some sesquiterpenoids by shift reagent NMR. (54 pp.) 1979
7. Häkli, Harri: Structure analysis and molecular dynamics of cyclic compounds by shift reagent NMR. (48 pp.) 1979
8. Pitkänen, Ilkka: Thermodynamics of complexation of 1,2,4-triazole with divalent manganese, cobalt, nickel, copper, zinc, cadmium and lead ions in aqueous sodium perchlorate solutions. (89 pp.) 1980
9. Asunta, Tuula: Preparation and characterization of new organometallic compounds synthesized by using metal vapours. (91 pp.) 1980
10. Sattar, Mohammad Abdus: Analyses of MCPA and its metabolites in soil. (57 pp.) 1980
11. Bibliography 1980. (31 pp.) 1981
12. Knuuttila, Pekka: X-Ray structural studies on some divalent 3d metal compounds of picolinic and isonicotinic acid N-oxides. (77 pp.) 1981
13. Bibliography 1981. (33 pp.) 1982
14. 6th National NMR Symposium, September 9-10, 1982, Abstracts. (49 pp.) 1982
15. Bibliography 1982. (38 pp.) 1983
16. Knuuttila, Hilkka: X-Ray structural studies on some Cu(II), Co(II) and Ni(II) complexes with nicotinic and isonicotinic acid N-oxides. (54 pp.) 1983
17. Symposium on inorganic and analytical chemistry, May 18, 1984, Program and Abstracts. (100 pp.) 1984
18. Knuutinen, Juha: On the synthesis, structure verification and gas chromatographic determination of chlorinated catechols and guaiacols occuring in spent bleach liquors of kraft pulp mill. (30 pp.) 1984
19. Bibliography 1983. (47 pp.) 1984
20. Pitkänen, Maija: Addition of BrCl, B_2 and Cl_2 to methyl esters of propenoic and 2-butenoic acid derivatives and ^{13}C NMR studies on methyl esters of saturated aliphatic mono- and dichlorocarboxylic acids. (56 pp.) 1985
21. Bibliography 1984. (39 pp.) 1985
22. Salo, Esa: EPR, ENDOR and TRIPLE spectroscopy of some nitrogen heteroaromatics in liquid ammonia. (111 pp.) 1985
23. Humppi, Tarmo: Synthesis, identification and analysis of dimeric impurities of chlorophenols. (39 pp.) 1985

24. Aho, Martti: The ion exchange and adsorption properties of sphagnum peat under acid conditions. (90 pp.) 1985

25. Bibliography 1985 (61 pp.) 1986

26. Bibliography 1986. (23 pp.) 1987

27. Bibliography 1987. (26 pp.) 1988

28. Paasivirta, Jaakko (Ed.): Structures of organic environmental chemicals. (67 pp.) 1988

29. Paasivirta, Jaakko (Ed.): Chemistry and ecology of organo-element compounds. (93 pp.) 1989

30. Sinkkonen, Seija: Determination of crude oil alkylated dibenzothiophenes in environment. (35 pp.) 1989

31. Kolehmainen, Erkki (Ed.): XII National NMR Symposium Program and Abstracts. (75 pp.) 1989

32. Kuokkanen, Tauno: Chlorocymenes and Chlorocymenenes: Persistent chlorocompounds in spent bleach liquors of kraft pulp mills. (40 pp.) 1989

33. Mäkelä, Reijo: ESR, ENDOR and TRIPLE resonance study on substituted 9,10-anthraquinone radicals in solution. (35 pp.) 1990

34. Veijanen, Anja: An integrated sensory and analytical method for identification of off-flavour compounds. (70 pp.) 1990

35. Kasa, Seppo: EPR, ENDOR and TRIPLE resonance and molecular orbital studies on a substitution reaction of anthracene induced by thallium(III) in two fluorinated carboxylic acids. (114 pp.) 1990

36. Herve, Sirpa: Mussel incubation method for monitoring organochlorine compounds in freshwater recipients of pulp and paper industry. (145 pp.) 1991

37. Pohjola, Pekka: The electron paramagnetic resonance method for characterization of Finnish peat types and iron (III) complexes in the process of peat decomposition. (77 pp.) 1991

38. Paasivirta, Jaakko (Ed.): Organochlorines from pulp mills and other sources. Research methodology studies 1988-91. (120 pp.) 1992

39. Veijanen, Anja (Ed.): VI National Symposium on Mass Spectrometry, May 13-15, 1992, Abstracts. (55 pp.) 1992

40. Rissanen, Kari (Ed.): The 7. National Symposium on Inorganic and Analytical Chemistry, May 22, 1992, Abstracts and Program. (153 pp.) 1992

41. Paasivirta, Jaakko (Ed.): CEOEC'92, Second Finnish-Russian Seminar: Chemistry and Ecology of Organo-Element Compounds. (93 pp.) 1992

42. Koistinen, Jaana: Persistent polychloroaromatic compounds in the environment: structure-specific analyses. (50 pp.) 1993

43. Virkki, Liisa: Structural characterization of chlorolignins by spectroscopic and liquid chromatographic methods and a comparison with humic substances. (62 pp.) 1993

44. Helenius, Vesa: Electronic and vibrational excitations in some biologically relevant molecules. (30 pp.) 1993

45. Leppä-aho, Jaakko: Thermal behaviour, infrared spectra and x-ray structures of some new rare earth chromates(VI). (64 pp.) 1994

46. Kotila, Sirpa: Synthesis, structure and thermal behavior of solid copper(II) complexes of 2-amino-2- hydroxymethyl-1,3-propanediol. (111 pp.) 1994

47. Mikkonen, Anneli: Retention of molybdenum(VI), vanadium(V) and tungsten(VI) by kaolin and three Finnish mineral soils. (90 pp.) 1995

48. Suontamo, Reijo: Molecular orbital studies of small molecules containing sulfur and selenium. (42 pp.) 1995

49. Hämäläinen, Jouni: Effect of fuel composition on the conversion of fuel-N to nitrogen oxides in the combustion of small single particles. (50 pp.) 1995

50. Nevalainen, Tapio: Polychlorinated diphenyl ethers: synthesis, NMR spectroscopy, structural properties, and estimated toxicity. (76 pp.) 1995

51. Aittola, Jussi-Pekka: Organochloro compounds in the stack emission. (35 pp.) 1995

52. Harju, Timo: Ultrafast polar molecular photophysics of (dibenzylmethine)borondifluoride and 4-aminophthalimide in solution. (61 pp.) 1995

53. Maatela, Paula: Determination of organically bound chlorine in industrial and environmental samples. (83 pp.) 1995

54. Paasivirta, Jaakko (Ed.): CEOEC'95, Third Finnish-Russian Seminar: Chemistry and Ecology of Organo-Element Compounds. (109 pp.) 1995

55. Huuskonen, Juhani: Synthesis and structural studies of some supramolecular compounds. (54 pp.) 1995

56. Palm, Helena: Fate of chlorophenols and their derivatives in sawmill soil and pulp mill recipient environments. (52 pp.) 1995

57. Rantio, Tiina: Chlorohydrocarbons in pulp mill effluents and their fate in the environment. (89 pp.) 1997

58. Ratilainen, Jari: Covalent and non-covalent interactions in molecular recognition. (37 pp.) 1997

59. Kolehmainen, Erkki (Ed.): XIX National NMR Symposium, June 4-6, 1997, Abstracts. (89 pp.) 1997

60. Matilainen, Rose: Development of methods for fertilizer analysis by inductively coupled plasma atomic emission spectrometry. (41 pp.) 1997

61. Koistinen, Jari (Ed.): Spring Meeting on the Division of Synthetic Chemistry, May 15-16, 1997, Program and Abstracts. (36 pp.) 1997

62. Lappalainen, Kari: Monomeric and cyclic bile acid derivatives: syntheses, NMR spectroscopy and molecular recognition properties. (50 pp.) 1997

63. Laitinen, Eira: Molecular dynamics of cyanine dyes and phthalimides in solution: picosecond laser studies. (62 pp.) 1997

64. Eloranta, Jussi: Experimental and theoretical studies on some quinone and quinol radicals. (40 pp.) 1997

65. Oksanen, Jari: Spectroscopic characterization of some monomeric and aggregated chlorophylls. (43 pp.) 1998

66. Häkkänen, Heikki: Development of a method based on laser-induced plasma spectrometry for rapid spatial analysis of material distributions in paper coatings. (60 pp.) 1998

67. Virtapohja, Janne: Fate of chelating agents used in the pulp and paper industries. (58 pp.) 1998

68. Airola, Karri: X-ray structural studies of supramolecular and organic compounds. (39 pp.) 1998

69. Hyötyläinen, Juha: Transport of lignin–type compounds in the receiving waters of pulp mills. (40 pp.) 1999

70. Ristolainen, Matti: Analysis of the organic material dissolved during totally chlorine-free bleaching. (40 pp.) 1999

71. Eklin, Tero: Development of analytical procedures with industrial samples for atomic emission and atomic absorption spectrometry. (43 pp.) 1999

72. Välisaari, Jouni: Hygiene properties of resol-type phenolic resin laminates. (129 pp.) 1999

73. Hu, Jiwei: Persistent polyhalogenated diphenyl ethers: model compounds syntheses, characterization and molecular orbital studies. (59 pp.) 1999

74. Malkavaara, Petteri: Chemometric adaptations in wood processing chemistry. (56 pp.) 2000

75. Kujala Elena, Laihia Katri, Nieminen Kari (Eds.): NBC 2000, Symposium on Nuclear, Biological and Chemical Threats in the 21st Century. (299 pp.) 2000

76. Rantalainen, Anna-Lea: Semipermeable membrane devices in monitoring persistent organic pollutants in the environment. (58 pp.) 2000

77. Lahtinen, Manu: *In situ* X-ray powder diffraction studies of Pt/C, CuCl/C and Cu_2O/C catalysts at elevated temperatures in various reaction conditions. (92 pp.) 2000

78. Tamminen, Jari: Syntheses, empirical and theoretical characterization, and metal cation complexation of bile acid-based monomers and open/closed dimers. (54 pp.) 2000

79. Vatanen, Virpi: Experimental studies by EPR and theoretical studies by DFT calculations of α-amino-9,10-anthraquinone radical anions and cations in solution. (37 pp.) 2000

80. Kotilainen, Risto: Chemical Changes in wood during heating at 150-260 °C. (57 pp.) 2000

81. Nissinen, Maija: X-ray structural studies on weak, non-covalent interactions in supramolecular compounds. (69 pp.) 2001

82. Wegelius, Elina: X-ray structural studies on self-assembled hydrogen-bonded networks and metallosupramolecular complexes. (84 pp.) 2001

83. Paasivirta, Jaakko (Ed.): CEOEC'2001, Fifth Finnish-Russian Seminar: Chemistry and Ecology of Organo-Element Compounds. (163 pp.) 2001